

# NRE 4351 – NUCLEAR AND RADIOLOGICAL ENGINEERING DESIGN

## Spring 2024

### **MoSS Reactor**

**Alicia Borel, Matthew Louis, Jaden Minnick, Nathan  
Tanzosch**

---

Nuclear and Radiological Engineering  
Georgia Tech  
Atlanta, GA

April 24, 2024

## Contents

<b>1 Executive Summary</b>	<b>8</b>
<b>2 Introduction</b>	<b>8</b>
2.1 Introduction and Background . . . . .	8
2.2 State of the art . . . . .	8
2.2.1 Molten Salt Fuel . . . . .	8
2.2.2 Atmospheric Pressure Fuel Tube . . . . .	9
2.3 Alicia Safety Considerations . . . . .	10
2.4 Motivation . . . . .	10
2.5 Objective and Scope . . . . .	10
<b>3 Model and Approach/Methodology</b>	<b>11</b>
3.1 Corrosion Calculations . . . . .	11
3.1.1 History and Background . . . . .	11
3.1.2 Corrosion in Molten Salts . . . . .	12
3.1.2.1 The Oxidation-Reduction Reaction . . . . .	12
3.1.2.2 Examples . . . . .	12
3.1.2.3 The Damage Mechanism in Corrosion . . . . .	13
3.1.2.4 Corrosion Mechanisms and Considerations . . . . .	13
3.1.2.5 Redox Control . . . . .	15
3.1.2.5.a Coolant Salt Redox Control . . . . .	15
3.1.2.5.b Fuel Salt Redox Control . . . . .	15
3.1.3 Modelling Corrosion . . . . .	16
3.1.3.1 Thermodynamic Equilibrium . . . . .	16
3.1.3.2 The CALPHAD Method . . . . .	18
3.1.3.3 The MSTDB . . . . .	19
3.1.3.4 The Gibbs Energy Minimizer . . . . .	19
3.2 Thermophysical Properties . . . . .	21
3.2.1 Introduction . . . . .	21
3.2.2 Methods . . . . .	21
3.2.2.1 Ideal Density . . . . .	21
3.2.2.2 RK and Muggianu Interpolation . . . . .	21
3.2.2.3 Other Thermophysical Properties . . . . .	22
<b>4 Trade-Off Analyses and Initial Down-Selection</b>	<b>23</b>
4.1 Scoping Calculation for Natural Convection . . . . .	23
4.1.1 Introduction . . . . .	23
4.1.2 Free Convection on a Vertical Surface . . . . .	24
4.1.3 The Correlations . . . . .	26
4.1.4 The Intra-Pin Radial Temperature Profile . . . . .	26
4.1.5 Choice of a Reference Salt . . . . .	27
4.1.6 The Prandtl Number . . . . .	27
4.1.7 The Calculation . . . . .	28
4.1.8 Iterative Calculation of the Rayleigh Number . . . . .	28
4.1.9 Validity . . . . .	28
4.1.10 Results . . . . .	28
4.2 Sensitivity Study in PinCell Model . . . . .	29
4.2.1 PinCell Modeling . . . . .	29
4.2.2 PinCell Depletion . . . . .	32
4.3 Assembly Modeling . . . . .	33

<b>5 Materials Selection and Justifications</b>	<b>34</b>
5.1 Methodology and Relevant Considerations . . . . .	34
5.1.1 Materials Under Consideration . . . . .	35
5.1.1.1 Structural Materials . . . . .	35
5.1.1.1.a Stainless Steel 316 . . . . .	35
5.1.1.2 Salt Constituents . . . . .	35
5.1.1.2.a Exclusion of Bromides and Iodides . . . . .	36
5.1.1.2.b The Coolant Salt . . . . .	36
5.1.1.2.c The Fuel Salt . . . . .	36
5.1.2 Safety Margins . . . . .	36
5.2 Benchmarking Thermochimica . . . . .	37
5.2.1 The LiCl-KCl-PuCl <sub>3</sub> System . . . . .	37
5.2.1.1 Calculation of Binary Phase Diagrams . . . . .	37
5.2.1.1.a A Note on Stoichiometry . . . . .	37
5.2.1.1.b A Custom Pseudo Binary Phase Diagram Plotter . . . . .	37
5.2.1.1.c Benchmarking the Custom Phase Diagram Plotter . . . . .	38
5.2.1.1.d Numerical Artifacts . . . . .	39
5.2.1.1.e LiCl-KCl . . . . .	40
5.2.1.1.f LiCl-PuCl <sub>3</sub> . . . . .	41
5.2.1.2 Calculation of Ternary Phase Diagrams . . . . .	42
5.2.1.3 PuCl <sub>3</sub> Solubility . . . . .	42
5.2.2 Heat Capacity, Melting, and Boiling Points . . . . .	43
5.3 Redox Control and Corrosion Resistance . . . . .	43
5.3.1 Corrosivity of Fresh Fuel . . . . .	44
5.3.1.1 Parameters and Surrogates . . . . .	44
5.3.1.2 Results . . . . .	45
5.3.2 Corrosivity of the Coolant . . . . .	47
5.3.2.1 Parameters and Surrogates . . . . .	47
5.3.2.2 Results . . . . .	47
5.4 Optimization of Thermophysical Properties . . . . .	47
5.4.1 Thermophysical Property Benchmarking . . . . .	48
5.4.1.1 Chloride RK Comparisons . . . . .	48
5.4.1.2 Fluoride RK Comparisons . . . . .	49
5.4.1.3 Heat Capacity . . . . .	49
5.4.1.4 Thermal Conductivity . . . . .	51
5.4.1.5 Viscosity . . . . .	52
5.4.2 Melting and Boiling Point Benchmarking . . . . .	53
5.4.2.1 The Benchmark Case . . . . .	53
5.4.2.2 A Note on Special Salts . . . . .	53
5.4.3 Coolant Salt Optimization . . . . .	53
5.4.3.1 Optimization Criteria . . . . .	54
5.4.3.2 Constraints . . . . .	55
5.4.3.3 Choice of Solver . . . . .	55
5.4.3.4 Results . . . . .	55
5.4.4 Fuel Salt Optimization . . . . .	56
5.4.4.1 Optimization Criteria . . . . .	58
5.4.4.2 Results . . . . .	58
5.4.4.2.a Fuel Salt PuCl <sub>3</sub> Solubility . . . . .	61
5.5 Summary . . . . .	62

<b>6 Design Overview</b>	<b>64</b>
6.1 Reactor Design . . . . .	64
6.2 Core Modeling . . . . .	64
6.2.1 Control Rod Worth . . . . .	66
6.2.2 3-Batch Core . . . . .	66
6.2.3 Burnup . . . . .	66
6.2.4 Reactivity Coefficient . . . . .	68
<b>7 Fuel Cycle and Waste</b>	<b>69</b>
7.1 Fuel Cycle . . . . .	69
7.2 Decay Heat . . . . .	70
7.3 Waste . . . . .	70
<b>8 Thermal Hydraulics</b>	<b>72</b>
8.1 CFD Methodology . . . . .	74
8.1.1 Goals . . . . .	74
8.1.2 Modelling Approach . . . . .	75
8.1.2.1 CFDOF . . . . .	75
8.2 The Coolant Calculation . . . . .	75
8.2.1 Boundary Conditions . . . . .	75
8.2.2 The Profiles . . . . .	76
8.2.3 Radially Averaged Fields . . . . .	77
8.2.4 Clad Surface Averaged Fields . . . . .	78
8.3 The Fuel Calculation . . . . .	80
8.3.1 Approximating With a Shortened Pincell . . . . .	80
8.3.2 The Profiles . . . . .	80
8.3.3 Radially Averaged Fields . . . . .	81
8.3.4 Fields Along the Centerline . . . . .	82
8.4 A Worst Case Analysis . . . . .	83
8.5 The Need for Pumps . . . . .	84
8.6 Decay Heat . . . . .	84
8.7 Efficiency . . . . .	84
8.8 Conclusion . . . . .	84
<b>9 Safety</b>	<b>85</b>
9.1 Event Trees . . . . .	85
9.2 Accidents . . . . .	85
9.2.1 Power Excursion Accident . . . . .	86
9.2.2 Flow Decrease Accident . . . . .	86
9.2.3 Fuel Salt Leak Accident . . . . .	86
9.3 Severe Accidents . . . . .	86
9.3.1 Criticality Event . . . . .	86
9.3.2 Source Term Accident . . . . .	87
9.3.3 Decay Heat Accident . . . . .	88
9.4 Safety Functions . . . . .	89
9.4.1 A Note on Freeze Plugs . . . . .	89
<b>10 Regulations</b>	<b>89</b>
10.1 Venting of Radioactive Gases . . . . .	90
10.2 Radioactivity in the Coolant . . . . .	90
10.3 Dosimetry . . . . .	90
10.4 Other Basic Characteristics for MSR Safety pertaining to Our Design . . . . .	90

<b>11 Economics</b>	<b>91</b>
11.1 Capital Cost . . . . .	92
11.2 Fuel Cost . . . . .	93
11.3 Operational and Maintenance Costs . . . . .	93
11.4 Decommissioning Cost . . . . .	94
11.5 Profit Analysis . . . . .	94
<b>12 Summary of Findings and Conclusions</b>	<b>95</b>
<b>13 Compilation of all References</b>	<b>95</b>
<b>A Appendix</b>	<b>101</b>
A.1 Figures . . . . .	101
A.2 Tables . . . . .	104

## List of Figures

1 A reference diagram of the diving bell gas vent at the top of Moltex static salt fuel rods taken from [84]	10
2 Electronegativities of the periodic table . . . . .	12
3 Plots showing the material effects of corrosion by molten salts (taken from [45]) . . . . .	13
4 Various methods for modelling corrosion based on their length and timescale (taken from [79]) . . . . .	17
5 An illustration of the CALPHAD method taken from [79] . . . . .	18
6 Boundary layer development on a hot vertical plate. Velocity boundary layer (left), thermal boundary layer (right). Taken from [19] . . . . .	24
7 Fuel centerline temperature as a function of volumetric heat generation ( $\dot{q}$ ) and rod outer radius ( $r_o$ ) . . . . .	29
8 Fuel cycle and depletion analysis for a pin-cell model with multiple optimized parameters inside the design space determined from the pin-cell sensitivity studies. . . . .	32
9 Three types of assemblies designed in SCALE and visualized using FULCRUM . . . . .	33
10 The importance of stoichiometry in phase diagram calculation . . . . .	38
11 Benchmarks of the custom plotting tool to thermochimica for KCl-PuCl <sub>3</sub> . . . . .	39
12 Comparisons for the LiCl-KCl system . . . . .	40
13 Comparisons for the LiCl-PuCl <sub>3</sub> system . . . . .	41
14 Solubility Comparisons for the (0.586LiCl-0.414KCl)-PuCl <sub>3</sub> system . . . . .	43
15 The total corrosion depth with and without sacrificial Zr . . . . .	46
16 Fraction of corroded chromium . . . . .	46
17 Composition of corroded components . . . . .	47
18 Effect of controlling the ZrF <sub>2</sub> to ZrF <sub>4</sub> ratio . . . . .	48
19 Comparisons of calculations of the density of the KCl-NaCl pseudo binary system with experimental data . . . . .	49
20 Comparisons of calculations of the density of the ternary KCl-NaCl-UCl <sub>3</sub> system along the slice NaCl:UCl <sub>3</sub> = 0.25:0.75 with experimental data . . . . .	49
21 Comparisons of calculations of the density of the ternary NaF-LiF-ZrF <sub>4</sub> system along the slice NaF:LiF = 0.4:0.6 with experimental data . . . . .	50
22 Comparisons of calculations of the heat capacity of the two binary systems: LiF-KF, LiF-NaF, with experimental data given in [18] . . . . .	50
23 Comparisons of calculations of the thermal conductivity of the KCl-MgCl <sub>2</sub> system with experimental data . . . . .	51
24 Comparisons of calculations of the dynamic viscosity of LiF-NaF-KF (FLiNaK), LiF-BeF <sub>2</sub> (66-34 mol%), and LiF-BeF <sub>2</sub> (73-27 mol%) with experimental data . . . . .	52
25 The melting and boiling transitions for LiF-NaF-KF (0.465-0.115-0.42 mol%) . . . . .	53
26 The phase transition of the finalized coolant salt . . . . .	56
27 Final coolant salt thermophysical properties . . . . .	57

28	The phase transition of the finalized fuel salt . . . . .	59
29	Graphs showing initial attempts at calculating the final fuel salt density . . . . .	59
30	Final fuel salt thermophysical properties . . . . .	60
31	A pseudo binary phase diagram showing the solubility of PuCl <sub>3</sub> in the fuel salt . . . . .	61
32	The solubility of PuCl <sub>3</sub> in the fuel salt . . . . .	62
33	A basic core graphic that shows the side profile of the reactor and primary loop. The original image was taken from [4]. . . . .	65
34	A visual representation of the core layout produced in SCALE and visualized using FULCRUM. There are 211 individual assemblies arranged in a symmetrical hexagonal grid comprised of 18858 fuel rods. . . . .	67
35	The reactivity swing the core experiences in a 3-batch core at HFP ARO conditions over 730 days . . . . .	70
36	Radiotoxicity of 1 gram of MoSS Reactor waste compared to one gram of actinides from discharged LWR fuel . . . . .	71
37	The centerline temperatures calculated using the finalized coolant and fuel salts . . . . .	73
38	The clad temperatures calculated using the finalized coolant and fuel salts . . . . .	74
39	CFD meshes . . . . .	75
40	Coolant velocity (magnitude) and temperature profiles . . . . .	77
41	Radially averaged fields for the coolant calculation . . . . .	78
42	Clad surface averaged fields for the coolant calculation . . . . .	79
43	Fuel velocity (magnitude) and temperature profiles . . . . .	81
44	Radially averaged fields for the fuel calculation . . . . .	82
45	Fields along the fuel centerline . . . . .	83
46	Event tree for a criticality/reactivity insertion accident . . . . .	87
47	Event tree for a source term accident . . . . .	87
48	Event tree for a decay heat accident . . . . .	88
49	Event tree for a loss of coolant accident . . . . .	88
50	A reference diagram of a molten salt swing valve used in transporting molten salt in a solar plant taken from [64] . . . . .	101
51	Lattice shape sensitivity study in pin-cell depletion . . . . .	102
52	Fuel radius sensitivity study in pin-cell depletion . . . . .	102
53	P/D ratio sensitivity study in pin-cell depletion . . . . .	103
54	Uranium-Plutonium ratio sensitivity study in pin-cell depletion . . . . .	103
55	Radiotoxicity of 1 gram of discharged MoSS waste compared against its constituent groups, against discharged LWR waste, and against natural uranium . . . . .	104

## List of Tables

1	Relative atom fractions of higher actinides taken from destructive testing of Three Mile Island spent nuclear fuel with an average burnup of 51.1 GWD/MTU . . . . .	9
2	Density expansion coefficients for salt components . . . . .	27
3	Pin-cell Model base case properties . . . . .	30
4	Fuel salt isotopic weight percentages in base pin-cell depletion case . . . . .	30
5	Coolant salt isotopic weight percentage in base pin-cell depletion case . . . . .	31
6	Table of multiplication factor results from the assembly modeling . . . . .	34
7	A range of typical compositions of stainless steel 316, and their averages, taken for the purposes of this project from [68] . . . . .	35
8	Different specifications of the KCl-PuCl <sub>3</sub> system, i.e. in terms of mole fractions of endmember elements and moles of endmember elements . . . . .	37
9	Chemical surrogates for elements used in corrosion calculation along with references . . . . .	45
10	The composition of the fuel salt used for the fuel corrosion calculation . . . . .	45
11	Final coolant salt composition . . . . .	55
12	Availability of thermophysical properties for fuel salt components . . . . .	57
13	Final fuel salt composition . . . . .	58

14	Core loading regions and their average burnup and neutron fluence at 730 days at full power operation	68
15	Reactivity Coefficients calculated from temperature and density changes in the MoSS Reactor	68
16	Decay Heat in Watts Thermal Post-shutdown in the MoSS Reactor	70
17	Radiotoxicity in $m^3$ required to dilute to RCGa limit of one gram of discharged fuel in the MoSS Reactor compared against one gram of the starting actinides or one gram of natural uranium	71
18	Regulations for occupational and non-occupational dose	90
19	MIT Capital Cost Estimation [76]	92
20	Characteristics of Reactor Design [74]	92
21	Construction Schedule [74]	92
22	Investment Cost Comparison	93
23	Operation and Maintenance Cost [74]	93
24	Decommissioning Cost [70]	94
25	Component-Wise LCOE for MOSS Reactor	94
26	Profit from MOSS Reactor	94
27	ZAID values and their corresponding weight percentages for each fuel region at the beginning of cycle.	105

## 1 Executive Summary

The results of this study have shown promise for the introduction of a next-generation molten salt wasteburner reactor. This design has been coined as the MoSS Reactor (Molten Static Salt Reactor). It has been inspired by Moltex's SSR-W reactor, which uses fuel rods to contain fuel salt within the core while using a secondary salt as a working fluid to transport heat out of the core. Using this concept, we have applied nuclear engineering principles to design a fast spectrum reactor in which legacy nuclear waste shows almost a 90% decrease in radiotoxicity 300 years after being refined and re-utilized as fuel. This is while also generating over 150 megawatts of electricity that can be supplied to the grid and sold for profit. The design in of itself has numerous safety advantages over currently licensed reactors including but not limited to its atmospheric pressure reactor vessel and its ability to dissipate decay heat through natural circulation.

## 2 Introduction

One of the largest still unsolved concerns with commercial nuclear operations is what to do with spent fuel after it leaves a reactor. Currently, most spent fuel sits in temporary storage. Long term plans to close the fuel cycle through permanent geological disposal has encountered red tape from a variety of interest groups including but not limited to national and local governments, environmental advocacy groups, and worker protection groups. Finding a solution to this issue that is safe and economical is necessary to close the nuclear fuel cycle. One such option is waste burner reactors which are designed to decrease the radiotoxicity of spent fuel.

### 2.1 Introduction and Background

Wasteburner reactors have been on the forefront of next generation reactor concepts. Utilizing the world's stockpiles of spent nuclear fuel is more sustainable and economical compared to other options like geological storage. Specifically one major concern of spent nuclear waste is the length of time during which it remains hazardous to humans. Short-lived fission products that exist in spent fuel are particularly hazardous as their activity tends to be large and they decay via penetrating ionizing radiation. At the other end of the spectrum, higher actinides produced from neutron absorption in uranium have half-lives longer than the human species has existed; the danger they pose will be prevalent far beyond what anyone now can predict.

A solution resides in reprocessing the fuel. In contrast to fossil systems that burn their fuel in entirety, a large fraction of fissile elements remain in spent nuclear waste. Reprocessing the fuel allows for these and any useful byproducts from the nuclear fuel cycle to be recovered and used again.

### 2.2 State of the art

This project differs from the variety of other next-generation reactors by introducing the concept of a stationary molten fuel salt. Fuel salt, which is a hot liquid fuel source, is confined in pins that resemble traditional solid oxide fuel pins. These fuel pins are further surrounded by a non-fueled molten coolant salt. In the majority of fuel salt reactor concepts, the fuel salt is also the primary loop coolant, meaning that it is the primary heat transportation mechanism. Major concerns with this system are adjacent to those that arise with current light water reactors such as a loss-of-coolant-accident (LOCA). The difference being in a traditional molten salt concept that a LOCA would result in radioactive material being expelled from the core. The exclusion of radioactive fuel material from the coolant and accident conditions is a major draw of fuel rod concepts. Thus, a marriage between molten salt fuel and the operational history of fuel rod designs is theorized to result in a safer and more economical nuclear reactor.

#### 2.2.1 Molten Salt Fuel

The reactor fuel is novel in itself. Our team has chosen to create fuel salt that is a combination of depleted uranium and higher actinides from PWR fuel. Plutonium and the minor actinides have been shown to be able to be separated from spent nuclear fuel at up to 99.9% through a combination of electro-refining and countercurrent extraction with a lithium reductant [1]. Separating specific elements within the actinides, however, has been shown

to be energy intensive and has a lower purity yield due to Gibbs free energy considerations. Thus, we will be utilizing the ratio of plutonium to minor actinides (MA) taken from destructive testing of fuel rods discharged from the Three Mile Island nuclear site. The testing was administrated by Oak Ridge National Labs and the data was retrieved from SFCOMPO 2.0 (Spent Fuel Isotopic Composition) provided by the Nuclear Energy Agency [3]. The relative atom fractions of the higher actinides are shown below in Table 1. These Uranium, plutonium, and MAs all exist in stable forms as chloride salts in a ratio of 1:3, i.e. uranium trichloride. Thus, an atomic ratio of heavy metal elements to chlorine in the fuel salt is also assumed to be the same.

Plutonium in of itself is a fissile element in a fast neutron spectrum. Thus the idea of combining it with depleted uranium is to effectively breed in more Plutonium-239 in order to extend cycle length. An increased cycle length is directly correlated to a higher burnup at the same power, which is equivalent to a higher transmutation of transuranics in the fuel and a greater density of fission products. Fission products have half-lives orders of magnitudes lower than that of the transuranics, so although in the short-term their radiotoxicity will be increased, within a few hundred years these fission products will decay away and the net hazard will be decreased. The main concern of current high level waste are these transuranics which outlive hundreds of generations of humanity. By reducing the time scale for dangerous radiotoxicity, engineering permanent disposal solutions becomes an easier feat.

Table 1: Relative atom fractions of higher actinides taken from destructive testing of Three Mile Island spent nuclear fuel with an average burnup of 51.1 GWD/MTU

Isotope	Relative Atom Fraction
Pu-238	0.024440035
Pu-239	0.448358759
Pu-240	0.225844734
Pu-241	0.057146719
Pu-242	0.072085773
Am-241	0.078411732
Am-243	0.021148667
Np-237	0.067191653
Cm-244	0.005402089

### 2.2.2 Atmospheric Pressure Fuel Tube

One major benefit of utilizing a liquid fuel salt is that gaseous fission products are able to sublime out. In a comparable solid oxide fuel, fission products form inside of a strict chemical lattice structure where they inherently damage its integrity. The fission products thus break down the fuel and can poison the reactor as they remain trapped inside. In a liquid salt, there is no lattice structure to damage at all, and due to the unbonded nature, the fission products are free to disperse throughout. Moreover, specifically gaseous fission products exist at a much lower density than their liquid salt counterparts and thus will migrate out of the fuel salt and leave solution inside a fuel tube. If a fuel tube is given open headspace above the fuel salt line, these fission gasses can accrue here. This would ordinarily result in an increasing pressure in a fuel tube as the gasses accumulate in the fuel tube head, which can lead to material strain and potentially failure. In a light water reactor, the tubes are pressurized to maintain a boundary between the coolant and the fuel and prevent inward buckling from the coolant pressure, however for the static salt reactor neither of these requirements exist. Thus, it is theorized that one could have an unpressurized fuel tube wherein the fission gasses are allowed to "vent" into the greater reactor head. Further justification of the safety of venting fission gases will be addressed in ??.

Creating a one-directional-flow valve is of great importance to this design to prevent coolant salt from intermixing with the fuel salt. Moltex has numerous documents outlining that their final licensed design would include a fission gas venting system. Specifically they call it a "Diving Bell Gas Vent" and a figure showing a drawing of the Moltex design is shown as Figure 1. There is little to no information given regarding how this system operates or how it prevents backwards flow. Reaching out to Moltex directly also yielded no results in determining how their system functions. It is assumed that if the gas vent resides above the equilibrium coolant salt level that the vent would prevent the intake of liquid material from entering the fuel tube by maintaining gaseous pressure equivalent to that

of the reactor head.

One alternative solution is the use of swing valves currently designed for use in molten salt pipes, specifically molten salt thermal storage in a solar plant. These valves are designed for one-directional flow of molten salt, thus proving their reliability in temperature and corrosion conditions we would expect in the reactor core. A sample design is shown as Figure 50 in the Appendix. The main differences between this design and our anticipated usage would be firstly the change between horizontal and vertical flow, and secondly the change between flowing molten salt and flowing fission gasses. The authors of [2] calculated the pressure required to open the swing valve by one degree to be 84.8 kPa. This would be enough to allow fission gasses to effectively exist inside the fuel tube at less than two atmospheres pressure. However, taking into account this calculation was done for a horizontal rather than vertical opening, it is pertinent to realize that the force necessary to overcome gravity on the valve lid would be greater. Contrarily, the valve would not need to be as heavy in general as it can be designed with little to no expected back pressure from heavier molten salt as it sits currently. Thus, a conservative estimate of even five times the critical opening pressure would result in an equilibrium fuel tube pressure of approximately five atmospheres. This strain is negligible to the structural integrity of a fuel tube made of stainless steel, thus we conclude it to provide a satisfactory method for the release of fission gasses into the greater reactor pool.

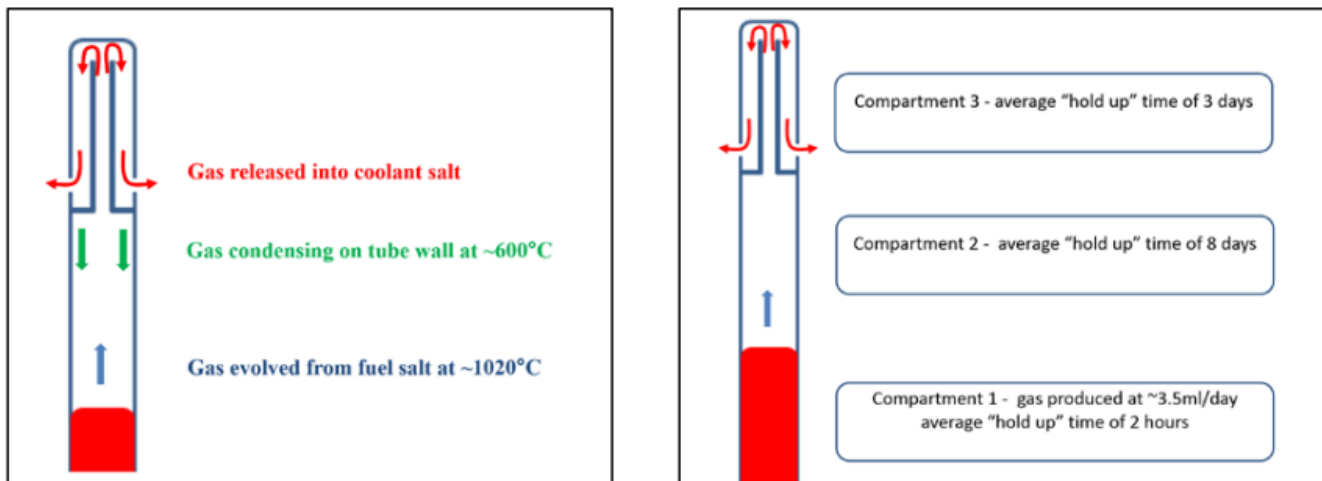


Figure 1: A reference diagram of the diving bell gas vent at the top of Moltex static salt fuel rods taken from [4]

## 2.3 Alicia Safety Considerations

## 2.4 Motivation

The primary motivations of designing a wasteburner static salt reactor is to reduce radiotoxicity in spent nuclear fuel, thus allowing for safer permanent disposal over a shorter time span. This goal, however, can only be achieved when applied to a working reactor that has economic utility. Thus, making the reactor system both reliable and affordable is critical to a fully functioning system. Secondary motivations are then achievements such as long cycle lengths to avoid frequent refueling costs and selecting favorable thermophysical properties that will allow for the safe operation of the reactor.

## 2.5 Objective and Scope

The objective of our project is to design a static salt reactor core and the associated systems that meet the following criteria. Firstly, the reactor must maintain significant margin from salt boiling. This is dependent on deriving quality salt characteristics and defining a geometry that maximizes heat transfer out of the core. Secondly, the reactor should reduce the radiotoxicity of its input reagents. In other words, the MoSS reactor fuel when discharged should have a lower radiotoxicity than the light water reactor discharged fuel it is initially composed of. A lofty goal would be to

reduce the radiotoxicity to natural levels within a few human generations, typically defined as around 300 years, as this would drastically decrease the costs and planning associated with storage of waste. Secondly, the reactor should have cycle lengths that are at least 18 months, mimicking large reactors currently in operation. As more reactors look towards longer cycle lengths such as two years between refueling, we want to maximize cycle length to match with industry patterns. The third objective is to determine the economic feasibility of the reactor, including its capital and operational costs. Discovering the break-even cost to charge for fuel reprocessing is critical in realizing that even if the reactor operates in theory, it needs to be attractive enough financially to investors or government authorities to utilize in practice..

The scope of our project is to design a static salt reactor core and the associated primary coolant loop. The fuel cycle, safety related systems, and operational degradation are all considered in scope to provide a holistic review of the design's potential strengths and weaknesses. Specifics regarding the extraction of thermal power from the active core and its subsequent reprocessing into either electrical energy or heat storage is considered out of scope as it is primarily reliant on the same technology used in reactors operating today. Any improvements to these systems will be left to further research.

## References

- [1] K. Kinoshita, T. Inoue, S. P. Fusselman, D. L. Grimmett, J. J. Roy, R. L. Gay, C. L. Krueger, C. R. Nabelek, and T. S. Storwick. Separation of uranium and transuranic elements from rare earth elements by means of multistage extraction in  $\text{LiCl-KCl}/\text{Bi}$  system. *Journal of Nuclear Science and Technology*, 36(2):189–197, 1999. doi: 10.1080/18811248.1999.9726197. URL <https://doi.org/10.1080/18811248.1999.9726197>.
- [2] S. Li, T. Ma, H. Shen, M. Yu, and Z. Lei. Analysis and optimization of the opening dynamic characteristics of molten salt check valves for concentrating solar power. *Applied Sciences*, 13(5), 2023. ISSN 2076-3417. doi: 10.3390/app13053146. URL <https://www.mdpi.com/2076-3417/13/5/3146>.
- [3] F. Michel-Sendis, I. Gauld, J. Martinez, C. Alejano, M. Bossant, D. Boulanger, O. Cabellos, V. Chrapciak, J. Conde, I. Fast, M. Gren, K. Govers, M. Gysemans, V. Hannstein, F. Havlůj, M. Hennebach, G. Hordosy, G. Ilas, R. Kilger, R. Mills, D. Mountford, P. Ortego, G. Radulescu, M. Rahimi, A. Ranta-Aho, K. Rantamäki, B. Ruprecht, N. Soppera, M. Stuke, K. Suyama, S. Tittelbach, C. Tore, S. V. Winckel, A. Vasiliev, T. Watanabe, T. Yamamoto, and T. Yamamoto. Sfcompo-2.0: An oecd nea database of spent nuclear fuel isotopic assays, reactor design specifications, and operating data. *Annals of Nuclear Energy*, 110:779–788, 2017. ISSN 0306-4549. doi: <https://doi.org/10.1016/j.anucene.2017.07.022>. URL <https://www.sciencedirect.com/science/article/pii/S0306454917302104>.
- [4] M. H. S. S. Banoori and F. Reitsma. Advances in small modular reactor technology developments, 2016.

## 3 Model and Approach/Methodology

### 3.1 Corrosion Calculations

#### 3.1.1 History and Background

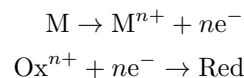
Molten salts are widely used in industrial heat transfer applications (e.g. concentrated solar power [20]) and have been considered as a coolant, fuel, and even energy storage fluids for nuclear reactors ever since the 1940s [25]. This widespread popularity is due to their favorable thermophysical properties: high heat capacity, large coefficient of thermal expansion (which introduces a strong negative temperature feedback), high boiling point (allowing for operation at near-atmospheric pressure), and their high chemical stability (specifically the formation of stable compounds with fission products such as Cs and I). These favorable properties come with a cost, however, as experience has shown in the molten salt reactor experiment (MSRE) [12] that molten salts are highly corrosive and can lead to severe degradation of structural materials if not properly managed.

### 3.1.2 Corrosion in Molten Salts

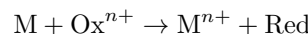
Herein we qualitatively describe the phenomenology of corrosion in molten salts, and how its effects will be mitigated to ensure adequate materials performance. Note, due to neutronic considerations, and the more favorable thermophysical properties of fluorides, a fluoride based coolant and a chloride based fuel salt were chosen (although there are some waste management challenges with the activation product  $^{36}\text{Cl}$  [7, 27]).

### 3.1.2.1 The Oxidation-Reduction Reaction

Fundamentally, corrosion reactions are characterized by a reaction between a species that accepts electrons (called an oxidant or oxidizer) and one that “donates” electrons that results in a net transfer of electrons to the oxidant thereby “reducing” it forming a reductant. This is expressed by the following individual (or half) reactions

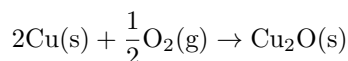


where the first reaction represents the anodic dissolution of a metal M (e.g. Ni, Fe, Cr, Co), and the second the cathodic reduction of the oxidant, where Ox and Red represent the oxidant and its corresponding reductant [10]. Together, these reactions form the overall electrochemical corrosion (oxidation reduction) reaction



### 3.1.2.2 Examples

A common example is the corrosion of copper



In this case, the oxidant is O<sub>2</sub>, and its reductant is O<sup>-</sup>. Conversely, the copper is oxidized to copper (I) Cu<sup>+</sup><sub>2</sub> and combines with the oxygen to form copper (I) oxide Cu<sub>2</sub>(I)O which appears red. Cu<sub>2</sub>O is further oxidized, and reacts with atmospheric CO<sub>2</sub>, SO<sub>3</sub>, and water H<sub>2</sub>O to produce the blue Cu<sub>2</sub>(OH)<sub>2</sub>(s) and green Cu<sub>4</sub>SO<sub>4</sub>(OH)<sub>6</sub>(s) compounds which together give corroded copper its characteristic blueish-green color [16]. In general, the oxidant is a strongly electronegative element such as O, or a halogen/halide (as is the case for molten salts) as shown in Fig. 2.

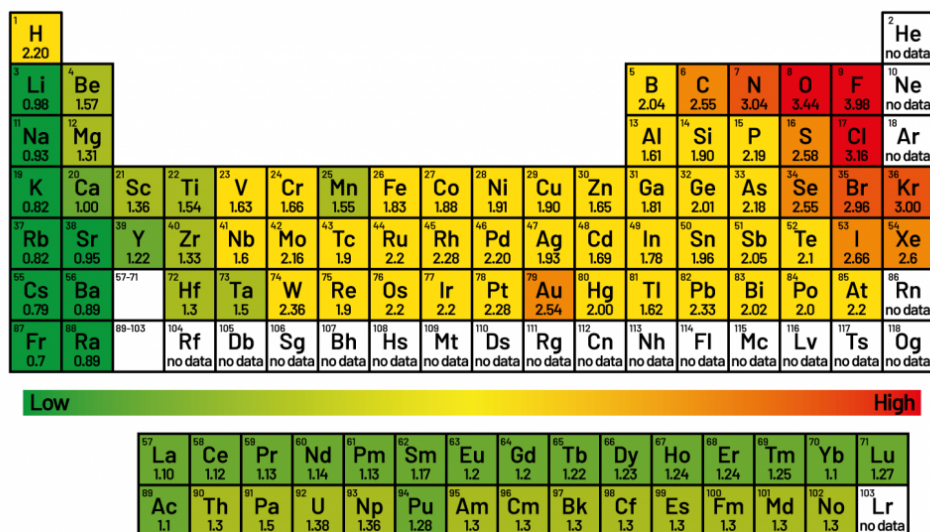
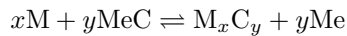


Figure 2: Electronegativities of the periodic table

In the case of molten salts, the oxidant is typically an alkali halide (denoted by Me) which oxidizes a pure metal component of a structural material (e.g. stainless steel Nimonic PE16 [13]) e.g. Ni, Co, Fe, or Cr (although Cr has been shown to be the most susceptible to corrosion in practice [17]) via the reaction (where C is a generic carrier halide, either Cl/F)



For Ni, Co, Fe, and Cr, the metal halide compound is  $NiC_2$ ,  $CoC_2$ ,  $FeC_2$ , and  $CrC_2/CrC_3$  [17]. However, for an aluminium metal, [17] suggests that a more complex species  $AlC_6^{3+}$  may form



### 3.1.2.3 The Damage Mechanism in Corrosion

In each of these cases, the redox reaction results in the migration of a component of a structural metal to the surface, after which it is dissolved by the molten salt. During their migration, these metal components may create interstices, and over time may lead to the creation of cracks. The phenomenology of corrosion damage and how it affects materials performance is of ongoing study [18]. This form of damage can be seen visually by using modern methods of microscopic imaging such as Scanning Electron Microscopy (SEM), an example of which is shown in Fig. 3a. Further, Energy Dispersive X-Ray Spectroscopy (EDS) can be used to determine the masses of metal components as a function of depth as in Fig. 3b, which clearly shows the selective dissolution of Cr from the metal surface, as well as the buildup of oxides and Ni/Mo [11].

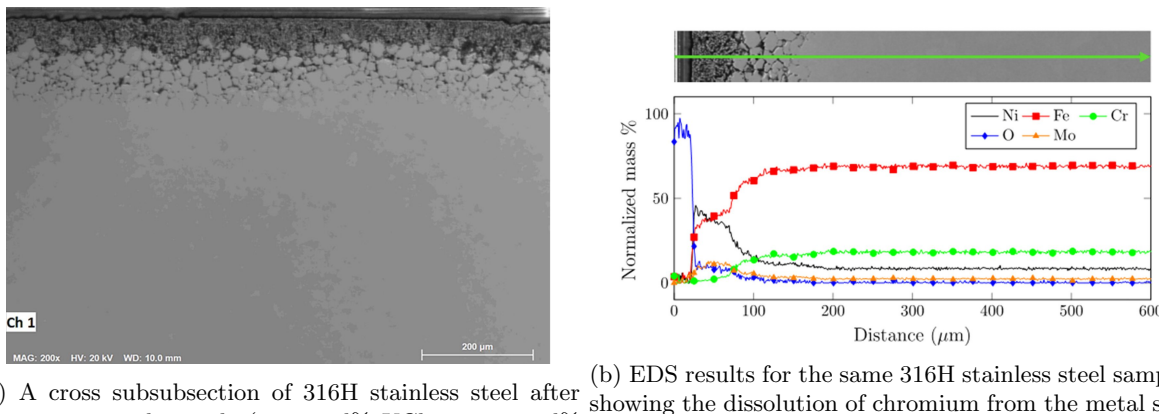


Figure 3: Plots showing the material effects of corrosion by molten salts (taken from [11])

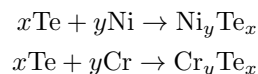
### 3.1.2.4 Corrosion Mechanisms and Considerations

As shown in the previous example, typically (especially in the case of atmospheric corrosion) a passivating oxide layer is formed which prevents further corrosion by fully coating the outer surface of the metal. This mechanism has been used effectively to mitigate corrosion in other nuclear reactor concepts such as the liquid lead-alloy-cooled reactor where an oxide layer prevents corrosion of structural materials by the liquid metal coolant [28]. In molten salts, these layers are not stable, as the oxides are generally soluble in the chloride/fluoride salt, and so they are effectively dissolved [10]. In fact, since these oxide layers are effectively dissolved, the addition of oxygen to a molten salt can even accelerate the corrosion by increasing the redox potential of the fuel [10]. Thus, corrosion by molten salts is entirely driven by thermodynamics. Corrosion rates then become determined by the rate at which susceptible metals can diffuse to the metal surface [6].

The redox potential is defined as the “tendency of a chemical species to acquire electrons and become reduced”, this is a measurable voltage that depends on the concentrations of the reduced and oxidized species, and is generally a good way of characterizing the driving force of redox reactions [10].

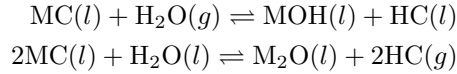
Among corrosion due to the pure salt are several other effects which can degrade structural materials [6]

- Effects caused by fission products, namely tellurium, which causes embrittlement and intergranular cracking via its preferential diffusion along the grain boundaries, and the following reactions [17]

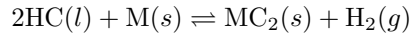


which result in the formation of brittle tellurides

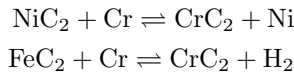
- Net release of halogens from actinide halides over time due to fission products having a lower average valency than the actinide
- Impurity driven corrosion
  - Oxygen and hydrogen contamination of the fuel salt from trace amounts of air or water, which can accelerate corrosion, and result in the formation of HF/HCl which are corrosive in their own right. I.e. where C represents the carrier (either F or Cl) [17]



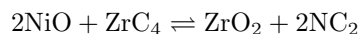
which can result in metal corrosion by the following reaction



- Metallic impurities such as Fe, Ni incorporated in the salt during manufacturing can cause the following corrosion reactions, which leach chromium from structural alloys [17]



- For zirconium-containing salts, the presence of oxides on the surface can lead to corrosion via



- To mitigate these effects, extensive purification methods were used in the MSRE and involve vacuum drying (to remove moisture) and hydrofluorination treatment to remove oxides, halides, and other impurities [17], however complete purity cannot be obtained in practice, so some concentration of impurities must be assumed

- Thermal gradient driven corrosion. The solubility of corrosion products is highly temperature dependent, so corrosion products dissolved in the salt at high temperature surface may deposit on cooler surfaces. This is particularly problematic in the coolant loop, where this effect can lead to deposition of corrosion products in heat exchanger tubes and pumps, as was observed over 9 years of operational experience in the MSRE [15]
- Formation of tritium and/or sulfur (via capture of Li in salts containing LiF/capture of Cl in chloride salts) increases redox potential continuously during operation, and are highly corrosive [10]
- Radiolysis can in principle drive the dissociation of molten salt halides into F<sub>2</sub>/Cl<sub>2</sub> gas, which can affect the redox state of the salt, but fortunately, under typical operating conditions, recombination effects dominate, and there is no net release of F<sub>2</sub>/Cl<sub>2</sub> [17].

### 3.1.2.5 Redox Control

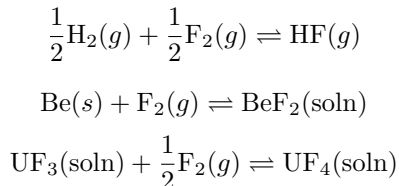
Corrosion can be mitigated by lowering the redox potential of the salt via additions of a reducing element to the salt. However, it must be noted that as long as the redox potential is nonzero, corrosion will occur, but what is important is that the rate of corrosion is small enough that it is negligible. Lowering the redox can also decrease the effect of tellurium embrittlement. The formation of brittle telluride compounds can be attributed to the corrosion reaction between tellurium and other metals. Belonging in the same (element) group as oxygen, it similarly oxidizes metals (e.g. Ni, Cr) to the (-1) or (-2) state, however, if the tellurium can be maintained in a strongly reducing state through proper redox control, this reaction can be mitigated [10].

#### 3.1.2.5.a Coolant Salt Redox Control

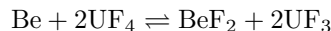
For a fluoride salt, the redox condition is defined as the fluorine potential  $\Delta\bar{G}_{F_2}$

$$\Delta\bar{G}_{F_2} = RT \ln p_{F_2}$$

where  $p_{F_2}$  is the partial pressure of fluorine in the salt. The fluorine potential can be controlled by controlling any of the following reactions, which establish the fluorine partial pressure  $p_{F_2}$  [10]



In other words, redox control can be achieved by controlling the ratios of  $\text{H}^{2+}/\text{H}$  ( $\text{H}_2/\text{HF}$ ),  $\text{Be}^{2+}/\text{Be}$  ( $\text{BeF}_2/\text{BeF}$ ), or  $\text{U}^{4+}/\text{U}^{3+}$  ( $\text{UF}_4/\text{UF}_3$ ). The first ratio may be controlled by the addition of a  $\text{H}_2/\text{HF}$  cover gas, the second by addition/removal of Beryllium metal from the system, and the third ratio may be controlled in a number of ways. The last method is how the redox was controlled in the molten salt reactor experiment [9], except instead of directly controlling the amount of  $\text{UF}_3$  in the fresh salt, beryllium metal was added in small capsules into the reactor's sampling system, which produces  $\text{UF}_3$  via the reaction



generating  $\text{UF}_3$  in this way is favorable because it is more thermodynamically favorable for  $\text{UF}_3$  to be converted to  $\text{UF}_4$  than for corrosion of Cr etc.

However, due to the high chemical toxicity of beryllium, we have chosen to exclude it from the coolant salt, in favor of a (albeit therapeutically inferior) Zr-based salt. This approach may not be suitable for a thermal system with a graphite moderator, because of the preferential formation of zirconium carbides, however for our fast system this is not an issue. In fluoride salts, zirconium forms two stable fluorides:  $\text{ZrF}_2$  and  $\text{ZrF}_4$ , and controlling the ratio  $\text{ZrF}_4/\text{ZrF}_2$  (e.g. by addition of small amounts of  $\text{ZrF}_2$  to the salt) can effectively control the overall redox state of the fuel [6, 5].

#### 3.1.2.5.b Fuel Salt Redox Control

The main difference between the fuel and coolant salts is that the fuel salt contains fissioning actinides, and in general will have a time-variable redox potential. The previously described method of adding small amounts of  $\text{ZrCl}_2$  to the fresh fuel salt cannot be used. While corrosion may initially be tolerable, with the accumulation of halogens and the formation of oxidizing sulfur, the redox state will quickly become strongly oxidizing, resulting in non-negligible amounts of corrosion. It is for this reason that the redox state in the MSRE had to be continuously monitored and modified. An online redox control system would likely be infeasible for a reactor with thousands of fuel rods, so a passive option must be sought. It has been suggested that the addition of small amounts of  $\text{MgCl}_2$  to the salt could effectively control the redox state [11], but the addition of too much  $\text{MgCl}_2$  can result in the formation of Mg-Ni intermetallics which can cause alloy embrittlement at high temperatures, so this technique still offers no solution for passive redox control.

Alternatively, Scott in [6] suggests the use of a sacrificial metal, which controls the redox state by corroding in place of the susceptible components of the structural materials, driving the salt to a strongly reducing state. This type of passive redox control can be problematic for pumped systems due to thermal-gradient driven corrosion, which might cause deposition of the sacrificial metal in cooler parts of the primary loop, resulting in the fouling of pumps and heat exchanger pipes. However, since the fuel is completely static, we have no such constraints. The use of a sacrificial metal can be either as a coating applied to the inner surface of the fuel tube, or as an insert. Scott in [6] suggests using zirconium as a sacrificial metal, although feasibly chromium or any other strongly reducing metal could also be used, but zirconium is perhaps the simplest and is already widely used in nuclear applications. The sacrificial metal can take the form of a coating on the inner part of the fuel tube (analogous to galvanizing steel, i.e. adding a protective zinc coating to prevent the formation of rust [14]) or can be an insert, as explored by [19], which also demonstrates the feasibility of using Zr for redox control in molten salts experimentally. It is also reported [6] that the use of a zirconium sacrificial metal scavenges tellurium, trapping it as  $ZrTe_2$ , effectively preventing embrittlement entirely. Also, due to the control of the redox state of the salt, sulfur preferentially forms actinide sulfides rather than corroding structural materials [6], though each of these claims must be verified.

### 3.1.3 Modelling Corrosion

As the previous discussion shows, the phenomenology of corrosion in molten salts is complicated, and needless to say, its accurate modelling requires complex tools. A wide variety of tools are available for modelling chemical effects, each suited to specific length and time scales (due to their theoretical formulation), and a sampling is shown in Fig. 4. Although the most accurate formalisms are those based on quantum mechanics and electronic structure (typically using density functional theory [2]), they are impractical for simulations of large engineering-scale problems such as molten salt reactors, and are rarely used for modelling of mesoscopic corrosion phenomena. Since the length-scale of corrosion is generally on the order of  $\mu m$ , for accurate corrosion calculations, the nuclear industry has preferred the use of phase field modelling [4], which is currently being implemented in the Yellowjacket corrosion suite (more information can be found [here](#)).

Accurate phase field modelling is considered outside the scope of this project, and instead simpler methods based on classical thermodynamics are pursued. A worst-case estimate for corrosion of structural alloys can be found by calculating the amount of corrosion in equilibrium (given a potentially infinite amount of time for the corrosion reaction to stabilize in the forward and reverse directions) [17]. The challenge then becomes the adequate modelling of the equilibrium state of a molten salt in contact with a structural component.

#### 3.1.3.1 Thermodynamic Equilibrium

The first law of thermodynamics dictates that energy is conserved, or, in terms of common quantities, that the infinitesimal change in internal energy of a system  $dU_{sys}$  must be brought about by either an infinitesimal heat addition  $\delta Q_{sys}$  or an infinitesimal amount of internal work  $dW_{sys}$  [24]

$$dU_{sys} = \delta Q_{sys} + dW_{sys}$$

the second law states that the entropy of the universe must *always* increase, so for a given system and its surroundings, an infinitesimal change in the system's entropy  $dS_{sys}$  and a corresponding change  $dS_{surr}$  must always add to a negative quantity

$$\begin{aligned} dS_{sys} + dS_{surr} &> 0 \\ \implies dS_{surr} &> -dS_{sys} \end{aligned}$$

Assume the system is in thermal and mechanical equilibrium (the temperature of the system is constant and there is no contribution from “shaft work” namely non- $p\delta V$  work), but *not* chemical equilibrium, so it may still partake in heat exchange with its environment. In such a case, the entropy imparted to the surroundings is given by

$$dS_{surr} = -\frac{\delta Q_{sys}}{T}$$

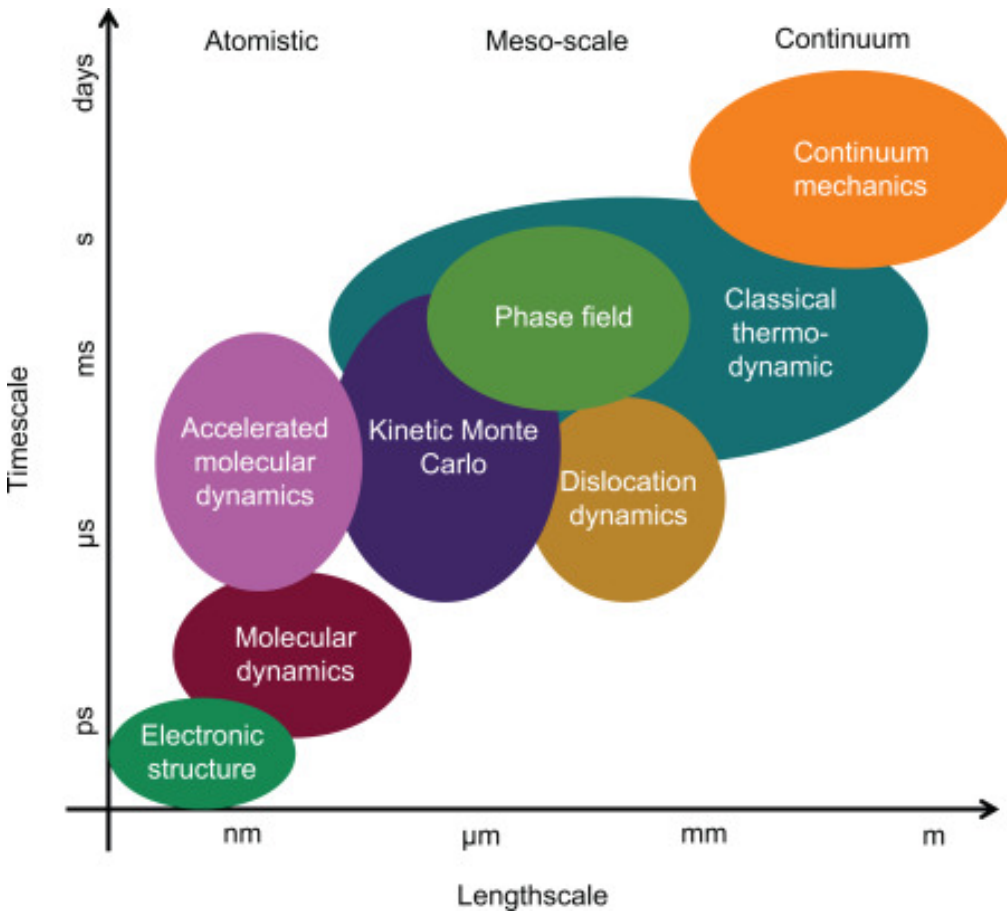


Figure 4: Various methods for modelling corrosion based on their length and timescale (taken from [24])

substituting this into the above expression of the second law gives

$$\begin{aligned} -\frac{\delta Q_{\text{sys}}}{T} &> -dS_{\text{sys}} \\ \delta Q_{\text{sys}} - TdS_{\text{sys}} &< 0 \end{aligned} \quad (1)$$

Now, since energy is conserved, we have that the corresponding change in internal energy and work must be related to the infinitesimal heat transfer by

$$\begin{aligned} dU_{\text{sys}} &= \delta Q_{\text{sys}} + dW_{\text{sys}} \\ \Rightarrow \delta Q_{\text{sys}} &= dU_{\text{sys}} - dW_{\text{sys}} \\ &= dU_{\text{sys}} - PdV_{\text{sys}} \end{aligned}$$

where shaft work is zero due to the condition of mechanical equilibrium. Substituting this expression into Eq. 1 gives

$$dU_{\text{sys}} - PdV_{\text{sys}} - TdS_{\text{sys}} < 0$$

and under the assumed isothermal and isobaric conditions, we may use the product rule to write the sum of differentials as a single differential

$$\begin{aligned} d(U_{\text{sys}} - PV_{\text{sys}} - TS_{\text{sys}}) &< 0 \\ \Rightarrow dG_{\text{sys}} &< 0 \end{aligned} \quad (2)$$

where the quantity  $G \equiv U_{\text{sys}} - PV_{\text{sys}} - TS_{\text{sys}}$  is often dubbed the “Gibbs energy”. Eq. 2 states that thermodynamically favorable changes (the only changes that can occur) are those that lower the Gibbs energy. At some point, the Gibbs energy cannot be lowered anymore, and the system will come to complete thermodynamic equilibrium. Thus for a closed isothermal-isobaric system, the condition for thermodynamic equilibrium is that the Gibbs energy is at a minimum [24]. In practice, this is how chemical thermodynamics codes compute the thermodynamic equilibrium state. However, to use the condition, we must have a way of calculating the Gibbs energy of an arbitrary system, which can be done systematically via the calphad method.

### 3.1.3.2 The CALPHAD Method

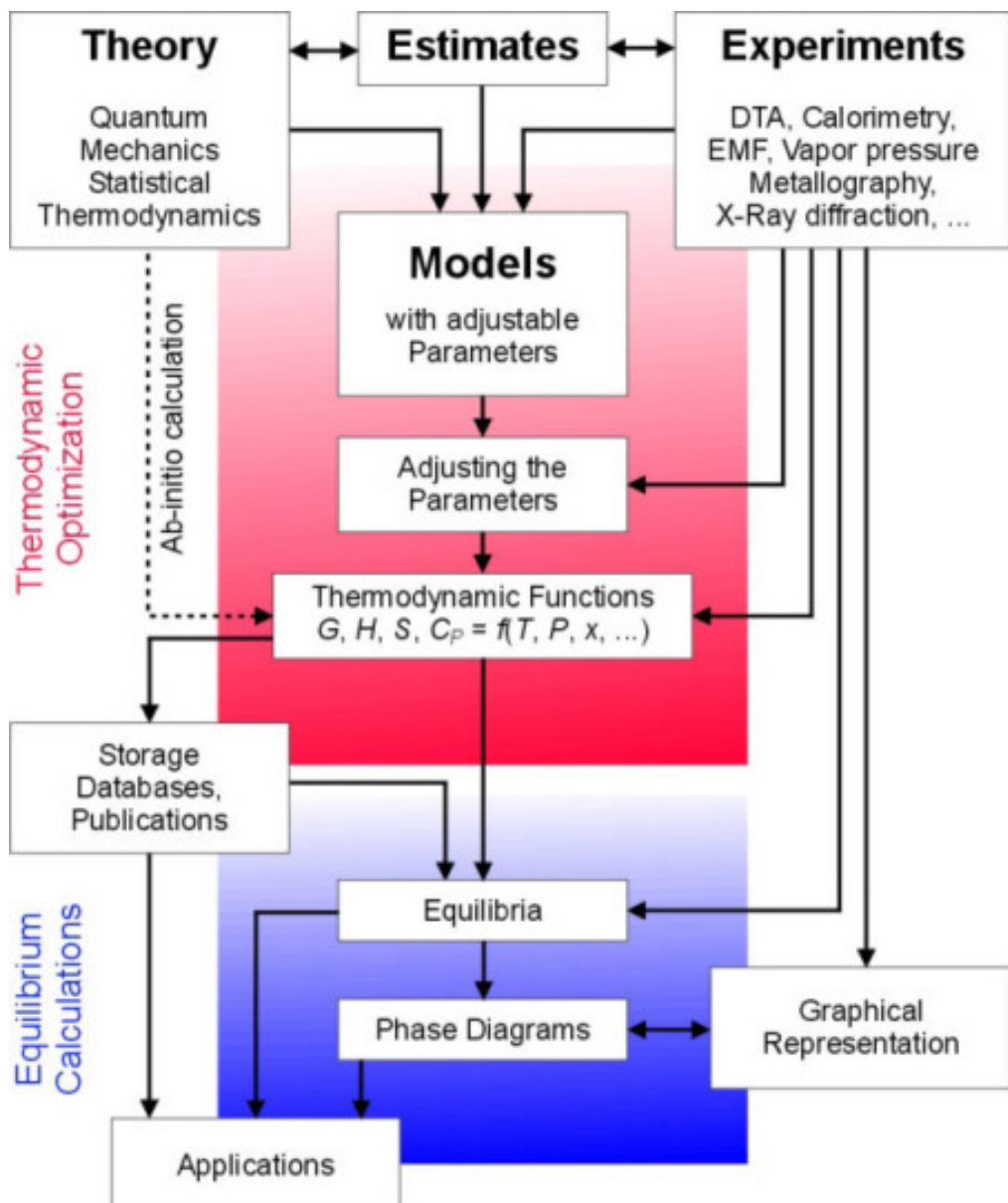


Figure 5: An illustration of the CALPHAD method taken from [24]

A basis set of elements and their binary, ternary, and higher-order interactions are represented in a database

by Gibbs energy equations, that can be used collectively to determine the Gibbs energy of the entire system. The development of such a database follows a systematic procedure known as the Calculation of Phase Diagrams Method (CALPHAD), and is schematically depicted in Fig. 5. Essentially, CALPHAD is “a methodological nonlinear regression” [24] which uses theoretical models along with experimental data to fine tune the database to better represent the thermodynamics of real systems. for example, measurements of heat capacity, along with enthalpy entropy data (as a function of temperature) derived from theoretical models applied to experimental data allow one to compute the Gibbs energy of a pure species (from Eq. 2). Since Gibbs energy is fully parameterized over the entire temperature-composition space, use of such a database (with an equilibrium thermodynamics code) can allow the calculation of entire binary/ternary phase diagrams, which are often needed to match the needs of the end user, since phase diagrams in the literature are often limited in their scope (e.g. are only plotted for a specific temperature/pressure) [24].

### 3.1.3.3 The MSTDB

One such database that has been developed for molten salts of relevance to nuclear applications is the Molten Salt thermal Properties Database (MSTDB) [3] and contains gibbs free energy functions computed with the modified quasichemical model in the quadruplet approximation (MQMQA), which is widely considered state-of-the-art. In addition to a thermochemical database, the MSTDB also has a compilation of thermophysical properties (density, heat capacity, viscosity, thermal conductivity) as well as techniques for expanding some quantities as a function of composition.

### 3.1.3.4 The Gibbs Energy Minimizer

Given a database, to compute the equilibrium state, a Gibbs Energy Minimizer (GEM) is needed. Several of these tools have been developed for use in industry e.g. FactSage [1] and ThermoCalc [26]. There are also open source options such as ThermoChimica [23] and PyCalphad [21], which have similar capabilities, but only ThermoChimica is currently compatible with the MQMQA and the format of the MSTDB thermochemical database format (written in the ChemSage format, compatible with FactSage and ThermoCalc industry codes), and so this code was chosen as the GEM for this project. Also of note is the newly developed GEM in the Yellowjacket corrosion suite [22], however this tool has not yet been made available (or perhaps is still in development). In addition, ThermoChimica has successfully been used previously by Graham [8] in a full multiphysics model of the molten salt reactor experiment to predict the formation of various phases of interest throughout the entire primary loop.

## References

- [1] C. W. Bale, P. Chartrand, S. Degterov, G. Eriksson, K. Hack, R. B. Mahfoud, J. Melançon, A. Pelton, and S. Petersen. Factsage thermochemical software and databases. *Calphad*, 26(2):189–228, 2002.
- [2] A. D. Becke. Density-functional thermochemistry. i. the effect of the exchange-only gradient correction. *The Journal of chemical physics*, 96(3):2155–2160, 1992.
- [3] T. M. Besmann and J. Schorne-Pinto. Developing practical models of complex salts for molten salt reactors. *Thermo*, 1(2):168–178, 2021.
- [4] C. V. Bhave, G. Zheng, K. Sridharan, D. Schwen, and M. R. Tonks. An electrochemical mesoscale tool for modeling the corrosion of structural alloys by molten salt. *Journal of Nuclear Materials*, 574:154147, 2023.
- [5] W.-J. Cheng, R. S. Sellers, M. H. Anderson, K. Sridharan, C.-J. Wang, and T. R. Allen. Zirconium effect on the corrosion behavior of 316l stainless steel alloy and hastelloy-n superalloy in molten fluoride salt. *Nuclear technology*, 183(2):248–259, 2013.
- [6] T. J. Dolan. *Molten salt reactors and thorium energy*. Woodhead Publishing, 2017.
- [7] C. W. Forsberg. Reactors with molten salts: options and missions. *Frederick Joliot & Otto Hahn Summer School on Nuclear Reactors, Physics and Fuels Systems, Cadarache, France*, 2004.

- [8] A. M. Graham, Z. Taylor, B. S. Collins, R. K. Salko, and M. Poschmann. Multiphysics coupling methods for molten salt reactor modeling and simulation in vera. *Nuclear Science and Engineering*, 195(10):1065–1086, 2021.
- [9] W. Grimes. Molten-salt reactor chemistry. *Nuclear Applications and Technology*, 8(2):137–155, 1970.
- [10] S. Guo, J. Zhang, W. Wu, and W. Zhou. Corrosion in the molten fluoride and chloride salts and materials development for nuclear applications. *Progress in Materials Science*, 97:448–487, 2018.
- [11] K. Hanson, K. M. Sankar, P. F. Weck, J. K. Startt, R. Dingreville, C. S. Deo, J. D. Sugar, and P. M. Singh. Effect of excess mg to control corrosion in molten mgcl<sub>2</sub> and kcl eutectic salt mixture. *Corrosion Science*, 194:109914, 2022.
- [12] P. N. Haubenreich and J. Engel. Experience with the molten-salt reactor experiment. *Nuclear Applications and technology*, 8(2):118–136, 1970.
- [13] B. A. Hombourger. Conceptual design of a sustainable waste burning molten salt reactor. Technical report, EPFL, 2018.
- [14] I. A. Kartsonakis, S. G. Stanciu, A. A. Matei, R. Hristu, A. Karantonis, and C. A. Charitidis. A comparative study of corrosion inhibitors on hot-dip galvanized steel. *Corrosion Science*, 112:289–307, 2016.
- [15] J. Koger. Evaluation of hastelloy n alloys after nine years exposure to both a molten fluoride salt and air at temperatures from 700 to 560 0 c. Technical report, Oak Ridge National Lab., 1972.
- [16] A. Krätschmer, I. O. Wallinder, and C. Leygraf. The evolution of outdoor copper patina. *Corrosion Science*, 44(3):425–450, 2002.
- [17] F. Lantelme and H. Groult. *Molten salts chemistry: from lab to applications*. Newnes, 2013.
- [18] N. Larrosa, R. Akid, and R. Ainsworth. Corrosion-fatigue: a review of damage tolerance models. *International Materials Reviews*, 63(5):283–308, 2018.
- [19] C. Linder. Investigation of new materials and methods to reduce corrosion of stainless steel in contact with molten chloride salts., 2017.
- [20] K. Lovegrove and W. Stein. Concentrating solar power technology: principles, developments and applications. 2012.
- [21] R. Otis and Z.-K. Liu. pycalphad: Calphad-based computational thermodynamics in python. *Journal of Open Research Software*, 5(1), 2017.
- [22] B. Parikshit, M. Poschmann, M. Piro, C. Bhave, M. Tonks, and D. Schwen. Yellowjacket gibbs energy minimiser: computing thermochemical equilibrium for multiphysics simulations of molten salt reactors.
- [23] M. Piro, S. Simunovic, T. M. Besmann, B. Lewis, and W. Thompson. The thermochemistry library thermochimica. *Computational Materials Science*, 67:266–272, 2013.
- [24] M. H. Piro. Computational thermochemistry of nuclear fuel. In *Advances in Nuclear Fuel Chemistry*, pages 159–182. Elsevier, 2020.
- [25] M. Rosenthal, P. Kasten, and R. Briggs. Molten-salt reactors—history, status, and potential. *Nuclear Applications and Technology*, 8(2):107–117, 1970.
- [26] B. Sundman, B. Jansson, and J.-O. Andersson. The thermo-calc databank system. *Calphad*, 9(2):153–190, 1985.
- [27] D. Williams, L. Toth, and L. UT-Battelle. Chemical considerations for the selection of the coolant for the advanced high-temperature reactor. *ORNL/GEN4/LTR-05-011, Oak Ridge National Laboratory, Oak Ridge, TN*, 2005.
- [28] J. Zhang and N. Li. Review of the studies on fundamental issues in lbe corrosion. *Journal of nuclear materials*, 373(1-3):351–377, 2008.

## 3.2 Thermophysical Properties

### 3.2.1 Introduction

Thermophysical properties and their proper measurement are important to the safety and efficiency of reactor operation, and no reactor could hope to be licensed without extensive measurements and/or models of thermophysical properties. Currently, there is a severe lack of measurements of molten salt thermophysical properties for higher order systems (that would be used in potential reactor designs), and especially how they depend on composition, and understanding of which is necessary for fuel design and optimization. Molten salts are uniquely challenging to measure accurately due to their often high melting points, and corrosivity, which require the use of specialized instruments and handling facilities - the main cause of the scarcity of experimental data. In addition, molten salt properties measurements are *expensive*, and so to cope with this lack of information, the use of theoretical models is emphasized more than for more conventional reactor materials. One such technique that was developed to interpolate the composition-dependent thermophysical properties of molten salts is the Redlich-Kister expansion with Muggianu interpolation [2]. Currently, due to the lack of data for binary subsystems, this method may only be applied to the estimation of composition-dependent densities, but lower order approximations for other thermophysical properties are also discussed.

### 3.2.2 Methods

#### 3.2.2.1 Ideal Density

First, we define an ideal mixture: “In chemistry, an ideal solution or ideal mixture is a solution that exhibits thermodynamic properties analogous to those of a mixture of ideal gases.” [10]. In an ideal mixture of  $i$  components, one assumes that the volume of the mixture  $V_m$  is a weighted sum of the molar volumes of the components, i.e.

$$V_m = \frac{\sum_i x_i M_i}{\rho_{id}}$$

where  $\rho_{id}$  is the *ideal density* of the mixture,  $x_i$  is the molar concentration of the  $i$ th component, and  $M_i$  is the molar mass (or molecular weight) of the  $i$ th component. We may use the above equation to express the ideal density  $\rho_{id}$  if we assume molar volumes are additive, that is

$$V_m = \sum_i V_i = \sum_i \frac{x_i M_i}{\rho_i}$$

where  $\rho_i$  is the density of the  $i$ th component. Substituting into the equation and rearranging, we get

$$\rho_{id} = \frac{\sum_i x_i M_i}{\sum_i \frac{x_i M_i}{\rho_i}}$$

The above equation is only valid under the assumption that the enthalpy of mixing is zero [2] (Why? What step was this used in), which is not generally the case. First, note that the enthalpy of mixing is “the enthalpy liberated or absorbed from a substance upon mixing” [9]. A nonzero enthalpy of mixing results when the intermolecular forces between the components in a *mixture* are different than those between the *pure components* - this can happen when the components contain different molecule sizes or dissimilar polarities. For some simple systems, the assumption of ideal mixing to estimate the density of molten salt systems produce good results, but in some cases (perhaps even most cases) the density is highly nonideal [2]. To alleviate this, we need a mathematical framework that accounts for the interaction between the components.

#### 3.2.2.2 RK and Muggianu Interpolation

The density for the case of *nonideal* mixing is given as

$$\rho_{mix} = \rho_{id} + \rho_{ex}$$

where  $\rho_{\text{ex}}$  is an *excess* density term to account for differences in the average interaction energies of two mixed components, resulting in nonideality. For a pseudo binary system (only two components), the RK expansion allows for nonideality via

$$\rho_{\text{ex}} = x_1 x_2 \sum_{j=1}^n L_j^{12} (x_1 - x_2)^{j-1}$$

where  $n$  is the order of the RK expansion, and  $L_j^{12}$  is the  $j$ th order interaction parameter between components 1 and 2, defined as (for the case of density, which is often parameterized as [for a single component]  $\rho = A + BT$ )

$$L_j^{12} = A_j^{12} + B_j^{12}T$$

where the constants  $A_j^{12}$  and  $B_j^{12}$  define the temperature dependence of the interaction parameter. In some cases, only a first order expansion is used, however for cases in which  $A_j^{12} \geq 0.5$  a second order expansion is recommended. The constants  $A$  and  $B$  are determined by fitting the density  $\rho_{\text{ex}}$  to experimentally acquired data over a range of compositions and temperatures for the actual higher-order system. For a pseudo *ternary* system, ignoring the possibility of ternary interactions (which in most cases are negligibly small), the excess density term can be determined by the Muggianu geometric model [2]:

$$\rho_{\text{ex}} = x_1 x_2 \sum_{j=1}^n L_j^{12} (x_1 - x_2)^{j-1} + x_1 x_3 \sum_{j=1}^n L_j^{13} (x_1 - x_3)^{j-1} + x_2 x_3 \sum_{j=1}^n L_j^{23} (x_2 - x_3)^{j-1}$$

which is just the binary RK expansion for each constituent binary subsystem (i.e. 12, 13, 23). In addition, if the density of a pseudo-ternary salt system has been measured of a sufficient range of compositions and temperatures, one may add a ternary interaction term

$$x_1 x_2 x_3 L^{123}$$

where

$$L_j^{123} = A^{123} + B^{123}T$$

and the ternary interaction term only uses a first order expansion under the notion that binary interactions should dominate. This same approach may be used to expand the excess density of an arbitrary higher-order system of  $S$  components (in terms of binary subsystems) via

$$\rho_{\text{ex}} = \sum_{a=1}^{S-1} \sum_{b=2}^S \sum_{j=1}^n L_j^{ab} (x_a - x_b)^{j-1} \quad \text{for } a < b$$

### 3.2.2.3 Other Thermophysical Properties

The same expansion method may be used to expand other thermophysical properties such as viscosity and thermal conductivity (heat capacity can be effectively calculated using an equilibrium thermodynamics code, as it's built into the database [5]), however as shown above, the RK method requires high-quality measurements of all (or at least some) of the constituent pseudo-binary subsystems, but for some of these properties, *none* of the pseudo binary subsystems have adequate data, so the best one can do is an ideal estimation from the following ideal behavior equations

$$\begin{aligned} \log \mu_{\text{id}} &= \sum_i x_i \log \mu_i \\ k_{\text{id}} &= \sum_i x_i k_i \end{aligned}$$

where  $k$  and  $\mu$  are the conductivity and dynamic viscosity respectively. The logarithmic dependence of viscosity on its constituents was shown by Arrhenius [1], and the simplified model for thermal conductivity can be improved if one knows the heat capacity at constant volume and constant pressure ( $C_p$ ,  $C_v$ ) and the speed of sound in the molten salt [3, 6, 8, 7, 4], but the sophisticated models used in the preceding references are largely out of the scope of this project, and the ideal expressions above are sufficient. It is worth noting that there is active development on a user friendly GUI, Saline [5] for the molten salt thermal properties database which would seamlessly integrate both ideal and RK estimation techniques of thermophysical properties, but it seems the current state of the package is incompatible with the format of the thermophysical properties database.

## References

- [1] S. Arrhenius. Über die innere reibung verdünnter wässriger lösungen. *Zeitschrift für Physikalische Chemie*, 1 (1):285–298, 1887.
- [2] A. Birri, R. Gallagher, C. Agca, J. McMurray, and N. Dianne Bull Ezell. Application of the redlich-kister expansion for estimating the density of molten fluoride psuedo-ternary salt systems of nuclear industry interest. *Chemical Engineering Science*, 260:117954, 2022. ISSN 0009-2509. doi: <https://doi.org/10.1016/j.ces.2022.117954>. URL <https://www.sciencedirect.com/science/article/pii/S0009250922005383>.
- [3] G. Dul'Nev and Y. P. Zarichnyak. Thermal conductivity of liquid mixtures. *Journal of engineering physics*, 11 (6):400–402, 1966.
- [4] A. E. Gheribi, J. A. Torres, and P. Chartrand. Recommended values for the thermal conductivity of molten salts between the melting and boiling points. *Solar energy materials and solar cells*, 126:11–25, 2014.
- [5] S. Henderson, C. Agca, J. W. McMurray, and R. A. Lefebvre. Saline: An api for thermophysical properties. Technical report, Oak Ridge National Lab.(ORNL), Oak Ridge, TN (United States), 2021.
- [6] J. F. Kincaid and H. Eyring. Free volumes and free angle ratios of molecules in liquids. *The Journal of Chemical Physics*, 6(10):620–629, 1938.
- [7] M. Mikami, O. Odawara, and K. Kawamura. Sound velocity in heat transfer salt (mixture of molten sodium nitrate-potassium nitrate-sodium nitrite, 7/44/49 mol%) studied by an ultrasonic pulse-echo method. *Journal of Chemical and Engineering Data*, 26(4):411–413, 1981.
- [8] R. Powell, W. Roseveare, and H. Eyring. Diffusion, thermal conductivity, and viscous flow of liquids. *Industrial & Engineering Chemistry*, 33(4):430–435, 1941.
- [9] Wikipedia contributors. Enthalpy of mixing — Wikipedia, the free encyclopedia, 2023. URL [https://en.wikipedia.org/w/index.php?title=Enthalpy\\_of\\_mixing&oldid=1160533318](https://en.wikipedia.org/w/index.php?title=Enthalpy_of_mixing&oldid=1160533318). [Online; accessed 7-February-2024].
- [10] Wikipedia contributors. Ideal solution — Wikipedia, the free encyclopedia, 2024. URL [https://en.wikipedia.org/w/index.php?title=Ideal\\_solution&oldid=1197329062](https://en.wikipedia.org/w/index.php?title=Ideal_solution&oldid=1197329062). [Online; accessed 7-February-2024].

## 4 Trade-Off Analyses and Initial Down-Selection

### 4.1 Scoping Calculation for Natural Convection

#### 4.1.1 Introduction

The goal is to demonstrate the feasibility of cooling a molten salt fuel tube via natural convection, allowing the complete elimination of pumps from the system. First it is necessary to consider the heat transfer coefficient from the fuel tube wall to the coolant. First we review the models for a vertical plate (which are readily extended to a cylinder). Then, we derive the temperature profile in the rod (assuming only conductive heat transfer) for an arbitrary volumetric heat generation rate  $\dot{q}_{\text{gen}}$ . Finally, using a representative salt composition, the thermophysical properties may be evaluated (using the MSTDB) and the rod centerline temperature can be calculated as a function of  $\dot{q}_{\text{gen}}$ .

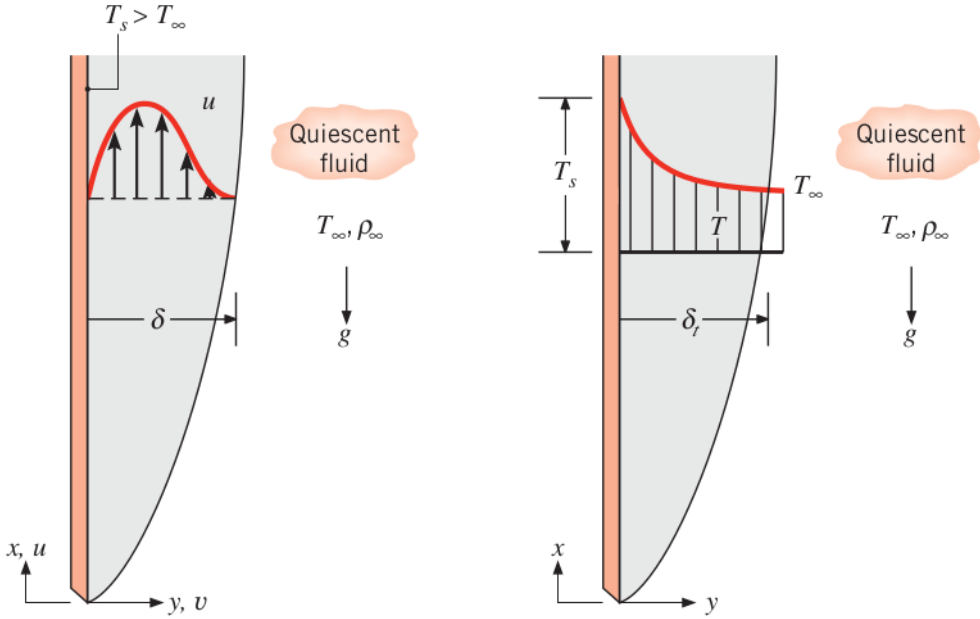


Figure 6: Boundary layer development on a hot vertical plate. Velocity boundary layer (left), thermal boundary (right). Taken from [2]

#### 4.1.2 Free Convection on a Vertical Surface

Considering a laminar boundary layer flow driven by buoyancy forces alone (shown in Fig. 6) and steady, two dimensional, constant property conditions in which gravity acts in the  $-x$  direction. Further, we assume the fluid is *incompressible* except for accounting for the density variation in the buoyancy force as it is the primary driving force of the flow (the validity of assuming incompressibility with respect to all other terms is discussed in [6]). Further, we assume the classical boundary layer approximations are valid (subsection 6.4.1 of [2]), namely that the pressure gradient within the boundary layer can be approximated by the free-stream pressure gradient, i.e.

$$\frac{\partial p}{\partial x} \approx \frac{dp_\infty}{dx}$$

which in this case is just  $-\rho_\infty g$  (the hydrostatic pressure gradient). This is usually a good approximation because the boundary layer is so thin. These assumptions allow us to derive the boundary layer equations (with a body force)

$$\begin{aligned} u \frac{\partial u}{\partial x} + v \frac{\partial u}{\partial y} &= -\frac{1}{\rho} \frac{dp_\infty}{dx} - g + \nu \frac{\partial^2 u}{\partial^2 y} \\ &= \frac{\rho_\infty g}{\rho} - g + \nu \frac{\partial^2 u}{\partial^2 y} \\ &= g \frac{\rho_\infty - \rho}{\rho} + \nu \frac{\partial^2 u}{\partial^2 y} \equiv g \frac{\Delta \rho}{\rho} + \nu \frac{\partial^2 u}{\partial^2 y} \end{aligned}$$

the first term on the right hand side of the above equation is the buoyancy force per unit mass, and is the driver for natural convection. If the density variations are due *only* to temperature variations, the buoyancy term may be related to a fluid property called the *volumetric thermal expansion coefficient* [2], defined as

$$\beta = -\frac{1}{\rho} \left( \frac{\partial \rho}{\partial T} \right)_p$$

which measures the response of density to a temperature variation at constant pressure. This term can be approximated as

$$\begin{aligned}\beta &\approx -\frac{1}{\rho} \frac{\Delta\rho}{\Delta T} = -\frac{1}{\rho} \frac{\rho_\infty - \rho}{T_\infty - T} \\ \implies \rho_\infty - \rho &\approx \rho\beta(T - T_\infty)\end{aligned}$$

this is known as the *Boussinesq approximation* [2], which then allows us to express the buoyancy term solely in terms of the free stream temperature difference and the volumetric expansion coefficient (taken as a known fluid property), yielding

$$u \frac{\partial u}{\partial x} + v \frac{\partial u}{\partial y} = g\beta(T - T_\infty) + \nu \frac{\partial^2 u}{\partial^2 y}$$

The buoyancy term effects only the momentum equation, and the energy and continuity equations take the usual form

$$\begin{aligned}\frac{\partial u}{\partial x} + \frac{\partial v}{\partial y} &= 0 \\ u \frac{\partial T}{\partial x} + v \frac{\partial T}{\partial y} &= \alpha \frac{\partial^2 T}{\partial^2 y}\end{aligned}$$

note that the viscous dissipation term has been neglected in the energy equation, and is typically a good approximation for the low-velocity flows associated with natural convection [2]. Unfortunately, the buoyancy term introduces a critical dependence on temperature in the momentum equation, making it impossible for all of the equations to be decoupled (as is done for forced convection). Now, it's important to introduce the relevant dimensionless parameters

$$\begin{aligned}x^* &= \frac{x}{L} & y^* &= \frac{y}{L} \\ u^* &= \frac{u}{u_0} & v^* &= \frac{v}{u_0} & T^* &= \frac{T - T_\infty}{T_s - T_\infty}\end{aligned}$$

where  $L$  and  $u_0$  are respective characteristic lengths and velocities for the flow. In terms of these dimensionless parameters, the  $x$ -momentum and energy equations reduce to

$$\begin{aligned}u^* \frac{\partial u^*}{\partial x^*} + v^* \frac{\partial u^*}{\partial y^*} &= \frac{g\beta(T_s - T_\infty)L}{u_0^2} T^* + \frac{1}{\text{Re}_L} \frac{\partial^2 u^*}{\partial^2 y^*} \\ u^* \frac{\partial T^*}{\partial x^*} + v^* \frac{\partial T^*}{\partial y^*} &= \frac{1}{\text{Re}_L \text{Pr}} \frac{\partial^2 T^*}{\partial^2 y^*}\end{aligned}$$

It's convenient to define the (as of yet) arbitrary reference velocity  $u_0$  so that the term multiplying  $T^*$  in the first equation is unity, this requires

$$u_0^2 = g\beta(T_s - T_\infty)L$$

which also effects the Reynolds number (because it explicitly involves the reference velocity), making it

$$\text{Re}_L = \left[ \frac{g\beta(T_s - T_\infty)L^3}{\nu^2} \right]^{1/2}$$

it's then customary to define the *Grashof number*  $\text{Gr}_L$  as the square of this Reynolds number

$$\text{Gr}_L \equiv \frac{g\beta(T_s - T_\infty)L^3}{\nu^2}$$

This dimensionless number is a ratio of buoyancy forces to viscous forces (rather than inertial to viscous as was the case for the Reynolds number in the nonbuoyant case). In addition, it's useful to define the Rayleigh number

$$\text{Ra}_L = \text{Gr}_L \text{Pr} = \frac{g\beta(T_s - T_\infty)L^3}{\nu\alpha}$$

Where the Prandtl number is given by

$$\text{Pr} = \frac{\alpha}{\nu} = \frac{\nu}{k/(\rho c_p)}$$

and is the ratio between thermal and viscous diffusivity.

#### 4.1.3 The Correlations

For the case of laminar flow ( $\text{Ra}_L \leq 10^9$ ) the correlation for the surface averaged Nusselt number is given by

$$\overline{Nu}_L = \frac{\bar{h}L}{k} = \frac{4}{3} \left( \frac{\text{Gr}_L}{4} \right)^{1/4} g(\text{Pr})$$

$$g(\text{Pr}) = \frac{0.75\text{Pr}^{1/2}}{(0.609 + 1.221\text{Pr}^{1/2} + 1.238\text{Pr})^{1/4}}$$

For non laminar flows, the correlations suitable for many engineering calculations are often of the form

$$\overline{Nu}_L = \frac{\bar{h}L}{k} = C \text{Ra}_L^n$$

for laminar flow with  $10^4 \leq \text{Ra}_L \leq 10^9$ ,  $C = 0.59$  and  $n = 1/4$ , for combined laminar and turbulent flow ( $10^9 \leq \text{Ra}_L \leq 10^{13}$ ),  $C = 0.1$  and  $n = 1/3$ . Alternatively, a correlation that may be used over the *entire* range of  $\text{Ra}_L$  has been suggested [2] and has the form

$$\overline{Nu}_L = \left[ 0.825 + \frac{0.387\text{Ra}_L^{1/6}}{[1 + (0.492/\text{Pr})^{9/16}]^{8/27}} \right]^2$$

where  $L$  is the plate length. Slightly better accuracy may be obtained for laminar flow by using

$$\overline{Nu}_L = 0.68 + \frac{0.670\text{Ra}_L^{1/4}}{[1 + (0.492/\text{Pr})^{9/16}]^{4/9}} \quad \text{Ra}_L \leq 10^9$$

Critically, the above results may be applied to vertical *cylinders* of height  $L$  if the boundary layer thickness  $\delta$  is much less than the cylinder diameter  $D$ . This condition is known to be satisfied when [2]

$$\frac{D}{L} \geq \frac{35}{\text{Gr}_L^{1/4}} \quad (3)$$

slender cylinders where transverse curvature influences the boundary layer development actually have enhanced heat transfer. Correlations have been provided in the literature for these cases as well.

#### 4.1.4 The Intra-Pin Radial Temperature Profile

Assuming only conduction, the radial temperature profile for a solid sphere with an arbitrary volumetric heat generation rate  $\dot{q}_{\text{gen}}$ , surface temperature  $T_s$ , and outer radius  $r_o$  is given by (subsection 3.5.2 of [2])

$$T(r) = \frac{\dot{q}r_o^2}{4k} \left( 1 - \frac{r^2}{r_o} \right) + T_s$$

We may also relate the surface temperature to the temperature of the cold (coolant molten salt) by performing an energy balance on the outer surface, which gives

$$T_s = T_\infty + \frac{\dot{q}r_o}{2h}$$

Note that the centerline temperature (which will be design limiting in our case) is given by

$$T(0) = \frac{\dot{q}r_o^2}{4k} + T_\infty + \frac{\dot{q}r_o}{2h}$$

#### 4.1.5 Choice of a Reference Salt

We use the same salt compositions as [4] being that it is the only other fast-spectrum reactor concept using the same fuel tube design that has been published. That is, the fuel salt has the following composition NaCl-PuCl<sub>3</sub>-UCl<sub>3</sub> (60-20-20 mol%), and the coolant salt has the composition ZrF<sub>4</sub>-NaF-KF (42-10-48 mol%). However, this exact composition is not available in the molten salt thermal properties database. This can be mitigated by using the Redlich-Kister to expand the (temperature varying) properties as a function of composition (mol fraction of end members) as detailed in [1], but for an initial simplistic analysis, we can just alter the composition to coincide with that in the database i.e. ZrF<sub>4</sub>-NaF-KF (52-5-52 mol%) which is close enough to the Moltex reference in any case. Unfortunately, the Molten Salt Thermal Properties Database (MSTDB [7]) is currently lacking almost all ternary chloride systems, so we will instead perform a *crude* approximation by taking the properties of the ternary system to be the average of those for the individual binary systems (i.e. NaCl – PuCl<sub>3</sub> (75-25 mol%) and NaCl – UCl<sub>3</sub> (75-25 mol%)). First note that in the MSTDB, density is interpolated via

$$\rho = A - BT$$

The exact composition (i.e. (75-25 mol%)) was available for the Pu binary system, which gives density coefficients In

	A (kg/m <sup>3</sup> )	B (kg/m <sup>3</sup> ·K)
NaCl-PuCl <sub>3</sub> (75-25 mol%)	3630	0.846
NaCl-UCl <sub>3</sub> (71.7-28.4 mol%)	3850	0.885
Estimated NaCl-PuCl <sub>3</sub> -UCl <sub>3</sub> (60-20-20 mol%)	3740	0.8655
ZrF <sub>4</sub> -NaF-KF (52-5-52 mol%)	3380	0.84

Table 2: Density expansion coefficients for salt components

this case, since we have an analytical expression for the temperature variation of the density so we can analytically compute  $\beta$  in terms of  $A$  and  $B$  (assuming these values were taken at constant pressure). By definition

$$\begin{aligned}\beta &= -\frac{1}{\beta} \left( \frac{\partial \rho}{\partial T} \right)_p \\ &= -\frac{1}{A - BT} (-B) \\ &= \frac{B}{A - BT}\end{aligned}$$

The remaining values were not available in the database, and may result in *large* errors, but for the sake of concreteness, we choose constant thermal conductivities of 0.5W/mK and 0.7W/mK and melting points of 738 K and 698 K for the fuel and coolant salt respectively (as used in Chapter 14 of [4]). Additionally, we take the fuel salt boiling point to be 1837 K (as in Chapter 14 of [4]).

#### 4.1.6 The Prandtl Number

Finally, to evaluate the Prandtl number (only needed for the coolant, since we're considering free convection of the coolant only) we need the viscosity and heat capacity. In the MSTDB viscosity is parameterized as

$$\nu = A \exp \left( \frac{B}{RT} \right)$$

where  $R$  is the ideal gas constant ( $R = 8.314 \text{ J/K}$ ), and the viscosity is given in units of  $\frac{\text{mN}\cdot\text{s}}{\text{m}^2}$  and so must be multiplied by  $10^{-3}$  in all applications. For the coolant salt, it was found that  $A = 0.161$  and  $B = 26400$ . Unfortunately, no heat capacity data was supplied for the chosen coolant salt, and so a crude estimate had to be employed. In Chapter 14 of [4], the author states that the heat capacity varies between 510 and 700  $\frac{\text{J}}{\text{kg}\cdot\text{K}}$  over the temperature range of 500-1500 °C. This variation was fit to a linear model of the form

$$c_p = A + BT$$

from which it was calculated that  $A = 363.1 \frac{\text{J}}{\text{kg}\cdot\text{K}}$  and  $B = 0.19 \frac{\text{J}}{\text{kg}\cdot\text{K}^2}$ .

#### 4.1.7 The Calculation

For the calculation, a heated rod height of  $L = 2.6\text{m}$  was used (taken from the relevant chapter discussing Moltex's previous design: the SSRU [5]). Additionally it was assumed that the coolant salt inlet temperature is 100 K over the evaluated melting temperature (i.e  $T_\infty = 838\text{ K}$ ). Notably, there are still the heat generation rate and the fuel pin radius  $r_o$  that have yet to be chosen. To explore the design space, these quantities were taken to be variable, and the fuel centerline temperature was calculated as a function of these. The chosen range was  $r_o \in [2 - 10]\text{mm}$  and  $\dot{q} \in [0, 200]\text{kW/L}$  noting that a typical LWR has  $r_o = 4.5\text{mm}$  and  $\dot{q} = 100\text{kW/L}$ .

#### 4.1.8 Iterative Calculation of the Rayleigh Number

The only thing left to note is that the Rayleigh number (which needs to be calculated to evaluate the Nusselt number and the subsequent heat transfer coefficient) depends on the surface temmperature, which is itself a function of the heat transfer coefficient. Additionally, it is customary to evaluate coolant properties at the average temperature  $T_{\text{eval}} = \frac{1}{2}(T_\infty + T_s)$ , so an iterative calculation on the heat transfer coefficient and surface temperature must be performed. In practice, this is performed by iteratively updating the heat transfer coefficient and surface temperature. By performing sensitivity on the number of iterations, it was determined that 100 inner iterations (to converge  $h$  and  $T_s$ ) was adequate (i.e. resulting in no noticeable change in the final results). The python implementation is shown below

```

1 # Need two loops, one over volumetric heat generation rate (in W/m3) and one for fuel
  pin radius ro
2 qgens = np.linspace(0, 200E+06, 100) # W/m3
3 ros = np.linspace(0.002, 0.01, 5) # 2mm-10mm
4
5 for ro in ros:
6     centerlineTemps = np.zeros(len(qgens))
7     for index, qgen in enumerate(qgens):
8         hguess = 1 # initial guess of h
9         Tsguess = 500 # initial guess of surface temp
10        for i in range(100):
11            Teval = 1/2*(Tsguess + Tinf) # Properties evaluated at average temp
12            Nu = NuL(Teval, hguess, qgen, ro)
13            hguess = kc/L*Nu # Update guess of h
14            Tsguess = Ts(hguess, qgen, ro)
15        centerlineTemps[index] = centerlineTemp(Tsguess, qgen, ro)

```

#### 4.1.9 Validity

On each outer iteration (over  $\dot{q}$  and  $r_o$ ) the condition for using the vertical plate correlation (Eq. 3) was evaluated, and not a single iteration did not satisfy the condition (due to the relatively large  $L$ ).

#### 4.1.10 Results

The results are shown in Fig. ???. As compared with an LWR, a much smaller pin radius is needed (around twice as small) to achieve similar power densities while maintaining a reasonable 200 K boiling margin (a 800 pcm reactivity insertion results in a 120 °C temperature increase [3], so 200 K is conservative) which is to be expected because of the poor thermal conductivity of molten salts. What is important is that this calculation demonstrates the feasibility of using *natural convection* to cool the reactor, allowing the complete elimination of pumps from the design, which represent both a safety hazard and a large technical challenge for conventional molten salt reactors.

## References

- [1] C. Agca and J. W. McMurray. Empirical estimation of densities in nacl-kcl-ucl3 and nacl-kcl-ycl3 molten salts using redlich-kister expansion. *Chemical Engineering Science*, 247:117086, 2022. ISSN 0009-2509.

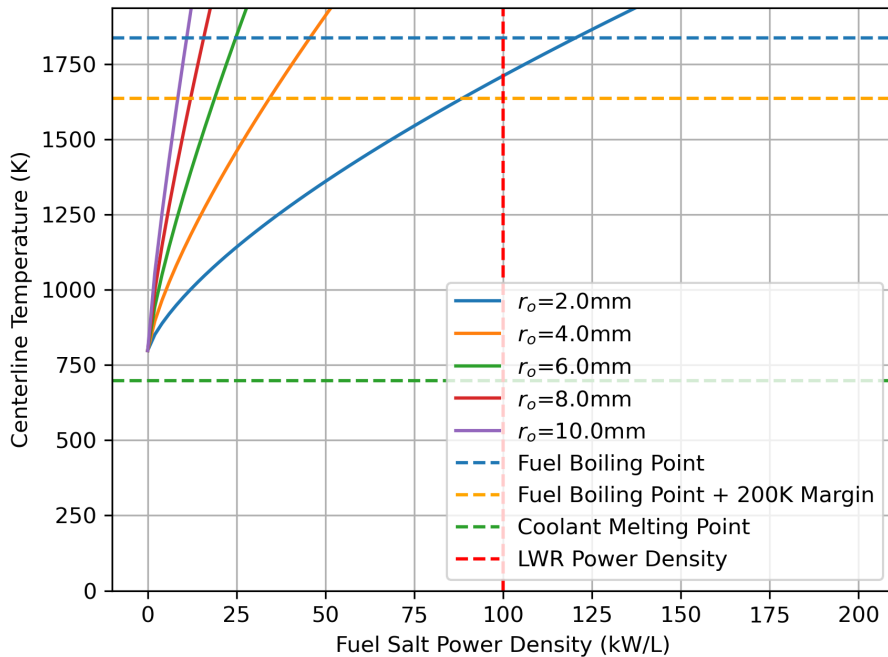


Figure 7: Fuel centerline temperature as a function of volumetric heat generation ( $\dot{q}$ ) and rod outer radius ( $r_o$ )

doi: <https://doi.org/10.1016/j.ces.2021.117086>. URL <https://www.sciencedirect.com/science/article/pii/S0009250921006515>.

- [2] T. L. Bergman. *Fundamentals of heat and mass transfer*. John Wiley & Sons, 2011.
- [3] M. Bushnaga, T. Oha, and Y. Kima. A neutronic study on safety characteristics of fast spectrum stable salt reactor (ssr). 2021.
- [4] T. J. Dolan. *Molten salt reactors and thorium energy*. Woodhead Publishing, 2017.
- [5] D. T. Ingersoll and M. D. Carelli. *Handbook of small modular nuclear reactors*. Woodhead Publishing, 2020.
- [6] P. R. Rubiolo, M. T. Retamales, V. Ghetta, and J. Giraud. High temperature thermal hydraulics modeling of a molten salt: application to a molten salt fast reactor (msfr). *ESAIM: Proceedings and Surveys*, 58:98–117, 2017.
- [7] N. Termini, A. Birri, S. Henderson, and N. D. B. Ezell. An overview of the molten salt thermal properties database–thermophysical, version 2.1.1 (mstdb-tp v.2.1.1). 7 2023. doi: 10.2172/1988348. URL <https://www.osti.gov/biblio/1988348>.

## 4.2 Sensitivity Study in PinCell Model

### 4.2.1 PinCell Modeling

A pincell model was constructed in SCALE for use in sensitivity studies to narrow down operating parameters in the search of a combination that would result in criticality. A “base” case was constructed with properties as shown in Table 3. The exact weight percentages used for fuel composition in the base case are shown in Table 4. Similarly, the weight percentages used for the coolant composition in the base case are shown in Table 5. Note that

these are not the optimized salt parameters as they were explored independently of this sensitivity study. Various parameters for geometry and material ratios were adjusted for simulation including the lattice shape, fuel pin radius, plutonium-to-uranium ratio (p/u), and pitch-to-diameter (p/d) ratio among others.

These models were created with a 1 cm height inside a unit cell corresponding to the lattice shape and pitch. All boundaries were set as mirror boundaries which represents an infinite geometry and accounts for no neutron leakage. The criticality simulations were run using continuous energy groups in the t6-depl SCALE module, which is the Triton depletion module coupled with the KENO-VI Monte Carlo criticality program. This was chosen over 2D deterministic options such as NEWT only due to a greater familiarity with the KENO-VI program. Utilizing the computing power from the Idaho National Lab High Performance Computing Center and multi-core processing, the Monte-Carlo simulations were able to achieve low error while maintaining efficient run-times. Each run took approximately two hours which comprised 10,000 particle histories for 105 generations for each of 11 burnup steps. This runtime was later determined to be hindered by the reflective boundary conditions wherein neutrons would interact with boundaries than the materials since their mean free path is much greater than that of the pincell geometry.

Table 3: Pincell Model base case properties

Fuel Radius	0.14 cm
Clad Thickness	0.06 cm
Pitch to Diameter Ratio	2:1
Lattice	Square
Clad Composition	Stainless Steel
Coolant Composition	48% KF, 10% NaF, 40% ZrF4, 2% ZrF2
Fuel Composition	20% UCl3, 35% ActCl3, 45% KCl
Fuel Temperature	1273K
Clad Temperature	973K
Coolant Temperature	733K

Table 4: Fuel salt isotopic weight percentages in base pincell depletion case

Isotope	Weight Fraction
U-238	0.212511481
U-235	0.000420507
Pu-239	0.167778578
Pu-240	0.084866083
Am-241	0.029587689
Np-237	0.02493312
Pu-242	0.027313533
Pu-241	0.021563601
Pu-238	0.009107344
Am-243	0.008046411
Cm-244	0.002063785
K-41	9.40906E-06
K-40	0.005292585
K-39	0.073340168
Cl-35	0.252406203
Cl-37	0.080759505

Table 5: Coolant salt isotopic weight percentage in base pin-cell depletion case

Isotope	Weight Fraction
Na-23	0.037194496
F-19	0.40335711
K-39	0.28218383
K-40	0.000036311
K-41	0.021408812
Zr-90	0.12971611
Zr-91	0.028602884
Zr-92	0.044200741
Zr-94	0.045768925
Zr-96	0.007530785

The lattice shape was compared between the base square and hexagonal geometries. The pitch over diameter ratio was conserved, however due to the higher packing factor the hexagonal case has a greater fuel to moderator ratio than the square lattice geometry. The hexagonal case has a ratio of 0.293 while the square lattice has a ratio of 0.244; this means that there is approximately a 20% greater fuel to moderator ratio in a hexagonal geometry. This percentage fuel is even greater for lower p/d ratios. For example a p/d ratio of 1.5 would result in a 25% greater fuel to moderator ratio in the hexagonal geometry compared to the square. The results from this modeling is shown in the appendix as Figure 51, wherein you can see a positive correlation between the multiplication factor and the greater fuel to moderator ratio associated with the hexagonal lattice.

The radius was also varied from the base parameter of 2 mm to 4 mm, 6 mm, and 20 mm. The p/d ratio is held constant for the different radii. The fuel to moderator ratio is held almost constant; it increases slightly with increasing radius due to maintaining the clad thickness. Only the size of the continuous regions of fuel and moderator are the contributing factors. Neutrons born inside the fuel are more likely to interact inside a fuel volume of a greater radius before interacting with the moderator, thus increasing the probability for fast fission events. The results from this modeling is shown in the appendix as Figure 52. It should be noted that increasing radius is associated with a greater multiplication factor, however, there are decreasing returns. The jump from 2 mm radius to 4 mm is approximately an increase of 0.11 in  $k_{inf}$ . The next jump from 4 mm to 6 mm results only in an increase of 0.04 in  $k_{inf}$ . The jump from 6 mm to 20 mm, over tripling the radius, only results in an increase of 0.075 in  $k_{inf}$ . Thus, one can interpret that the critical fuel radius most likely resides above 3 mm but below 8 mm to maximize multiplication without wasting fuel volume.

The third geometrical pin-cell sensitivity study conducted was varying the p/d ratio. This is another scenario of directly altering the fuel to moderator ratio, with this being the most direct case. The p/d ratio was modeled at values of one, two, and three. It should be noted that with a p/d ratio of one, the fuel rods would be just touching one another at their closest points, thus it is not a feasible real life option. Moreover, with a value of three the fuel would be much too spread out to form a critical geometry. In thermal spectrum cores, it is shown that a p/d ratio of 1.65 results in maximum multiplication factor due increasing resonance escape probability confounded with decreasing thermal utilization and fast fission probability [1]. For our fast system, the increased resonance escape probability is not incentivized as we are aiming for predominantly fast fissions. Thus, the wide array of values chosen here were to get more general trends and identify the limits in the fast spectrum. The results are shown in Figure 53 in the appendix. It can be seen that minimizing the p/d ratio is always the priority for increasing the neutron economy.

From a material standpoint, a sensitivity study was conducted on the ratio of depleted uranium to plutonium and higher actinides. While the ratio of actinides to plutonium was held constant due to constraints regarding the LWR spent fuel atomic makeup, these amalgamated transuranics could still be put in different ratios with uranium. In the base case, the ratio of uranium to plutonium was 4:7, and this was compared to other cases with ratios of 5:6, 3:8, and 2:9. The results are shown in Figure 54. As expected, the compositions with the greatest plutonium content had the greatest multiplication factor, however as will be explained further in the next section, the lowered uranium content comes with faster depletion. Thus, a fuel cycle from the same starting excess reactivity content would have a cycle length penalty compared to one with greater uranium content.

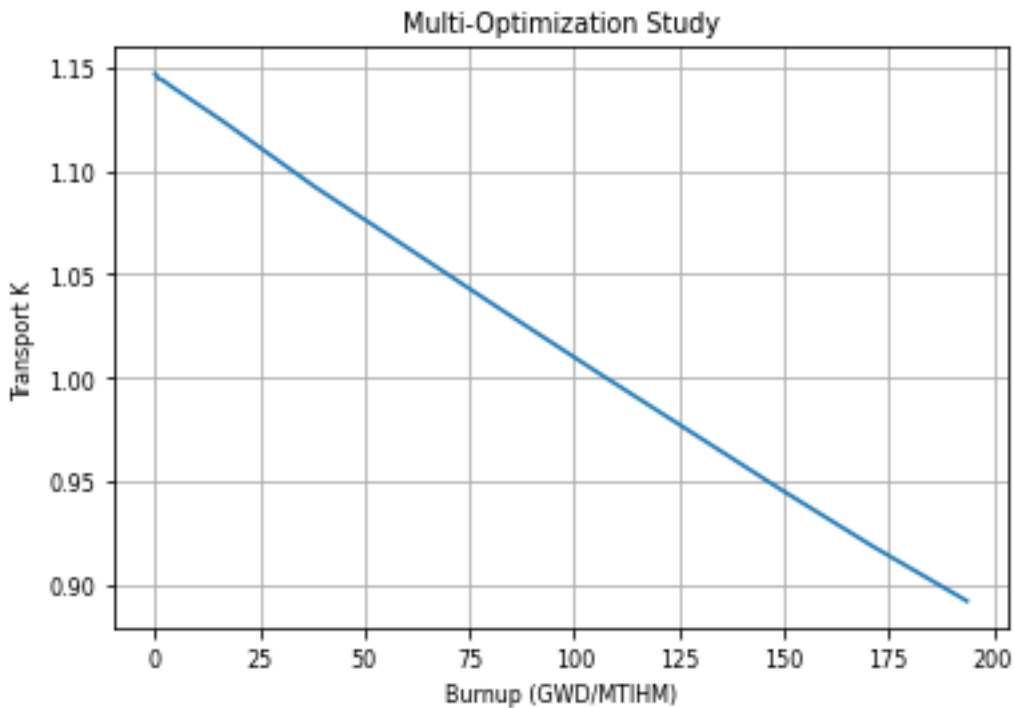


Figure 8: Fuel cycle and depletion analysis for a pin-cell model with multiple optimized parameters inside the design space determined from the pin-cell sensitivity studies.

From this initial pin-cell analysis, we were able to determine a critical operation space with bounds such as 1.1 to 1.5 p/d ratio, 10% to 15% depleted uranium content, and minimum 3 mm fuel radius. Other parameters were solidified; for example the hexagonal lattice shape was selected over square due to its higher packing ratio, which gave greater multiplication factor and thus allows for a wider design space for the other parameters. Inside this space, a combined optimized depletion case was performed with the results shown in Figure 8. This case had parameters such as 2:9 uranium-to-plutonium ratio, hexagonal lattice, 1.25 p/d ratio, and 4 mm fuel radius. The initial infinite multiplication factor is  $1.14689 \pm 0.00067$ , which is supercritical. This shows that the fast spectrum static salt design at minimum can maintain a sustained chain reaction. These parameters were then combined with thermohydraulic scoping as described in Section 4.1 to further refine the design space and determine assembly and greater core parameters such as active height and core power.

#### 4.2.2 Pin-cell Depletion

The other outcome from these studies were an initial depletion analysis. We were able to show that the pin-cell running with a specific power of 100 kW/L was creating a reactivity depletion of approximately 7-9 pcm per day depending on the initial U-238 content. Also important to note, this initial study confirmed that fission fragment poisoning, such as xenon, would not be a factor in our fuel cycle. There is no initial dip in reactivity as would be seen in a thermal reactor, and throughout the cycle the reactivity loss is linear. This is a positive in that there is no initial reactivity swing to manage in our reactor. A straight burn absorber, such as doping the initial fuel salts with boron, can help suppress initial high reactivity without major fuel cycle length penalties. It was shown that boron plate type burnable absorbers were successful at limiting the reactivity swing to less than 1000 pcm in the Compact Molten Salt Reactor (CMSR) design, as well as a less than 1000 pcm reactivity swing in a MSFR when boron was applied as a coating to beryllium reflectors [3] [2].

## References

- [1] J. Duderstadt and L. Hamilton. *Nuclear Reactor Analysis*. Wiley, 1976. ISBN 9788126541218. URL <https://books.google.com/books?id=xWvsswEACAAJ>.
- [2] E. Lee, T. Oh, and Y. Kim. Burnable absorber design study for fast-spectrum molten salt reactors. 2022. URL [https://www.kns.org/files/pre\\_paper/48/22A-209-%EC%9D%B4%EC%9D%80%ED%98%81.pdf](https://www.kns.org/files/pre_paper/48/22A-209-%EC%9D%B4%EC%9D%80%ED%98%81.pdf).
- [3] T. Oh, E. Lee, Y. Son, and Y. Kim. Preliminary analysis of burnable absorber concepts for seaborg compact molten salt reactor. 2022. URL [https://www.kns.org/files/pre\\_paper/48/22A-410-%EC%98%A4%ED%83%9C%EC%84%9D.pdf](https://www.kns.org/files/pre_paper/48/22A-410-%EC%98%A4%ED%83%9C%EC%84%9D.pdf).

### 4.3 Assembly Modeling

The greater components and substructure of an operational nuclear core are also needed, thus three types of assemblies have been modeled in SCALE. These are shown in Figure 9. The first type is a filled assembly, which is a hexagonal lattice of 91 individual fuel rods. The second type is a guide or instrument tube assembly in which it is the same as the filled assembly except the central seven fuel rods have been removed. This allows them to have instrumentation or reactivity control added in their place. This then leads into the third type, which is a control rod assembly. The control rod assembly is the same as the guide tube assembly except that it has the seven central fuel rods replaced with a boron carbide control rod. Boron carbide is traditionally a neutron absorber when used for reactivity control. In the MoSS core, scattering reactions also limit the ability for neutrons to cause fission reactions due to their then lower energy. Thus, one of the major upsides in a MoSS reactor control rod is that its negative reactivity is a sum of its absorption and its scattering cross sections. Each type of assembly is modeled with a stainless steel boundary that is used to create channels that will prevent lateral coolant flow in the core.

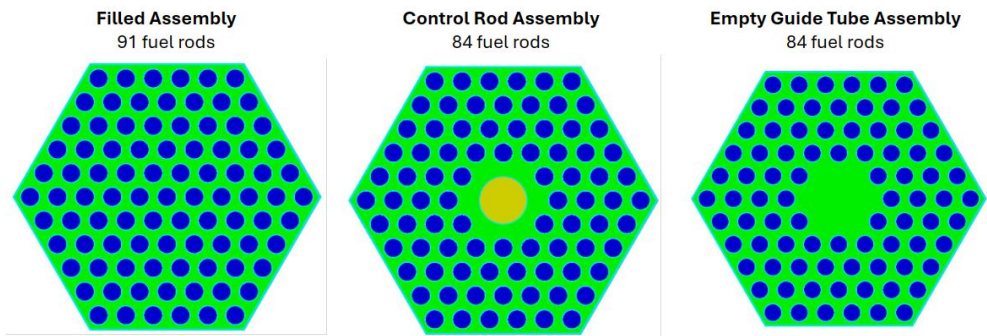


Figure 9: Three types of assemblies designed in SCALE and visualized using FULCRUM

These individual assembly types have been modeled in KENO-VI criticality simulations as an infinite lattice of infinite height. This assumption means no neutron leakage was accounted for, which has large implications on the neutron economy. In a fast system specifically, the larger attenuation length for high energy neutrons results in greater leakage than would be expected in thermal counterparts. This assumption is an expansion of the infinite pin-cell model made earlier in Section 4.2. Early modeling was made with parameters such as 4 mm fuel radius, 1.4 p/d, and the 3:8 uranium to plutonium ratio. Varying these gave promising results in the range of criticality, however, all of these models were for an infinite lattice, and as stated before, leakage in a fast spectrum reactor can reach up to 20%. This necessitates finding assembly parameters that have supercritical results.

A finalized parameter set of 5.5 mm outer clad radius, 1.35 p/d, and 2:9 uranium to plutonium ratio. The salts used in this analysis are the same as the pre-optimized solution shown in Tables 4 and 5. These geometry and material selections were used to get a sense of the multiplication factor for each assembly type, the results are shown in Table 6.

	Full Assembly	CR Assembly	GT Assembly
$k_{inf}$	$1.307560 \pm 0.000031$	$0.683238 \pm 0.000038$	$1.268513 \pm 0.00004$
Dryout $k_{inf}$	$1.549011 \pm 0.000051$		
Dryout $k_{eff}$	$0.083320 \pm 0.000019$		

Table 6: Table of multiplication factor results from the assembly modeling

An infinite lattice of the 91 rod filled assemblies has a multiplication factor value of over 1.31, which is extremely supercritical. This is compared to the empty guide tube assembly comprised of only 84 rods, which has a value of approximately 1.27. This is a drop of 2.99% whereas the number of rods drops disproportionately more by 7.69%. This shows that there is not a linear relationship between the ratio of fuel to coolant and the multiplication factor. The infinite lattice of control rod assemblies has a multiplication factor value of 0.68, which is a 47.75% drop from the filled assembly. The reactivity worth of the control rods is shown to be great enough to reduce the extremely supercritical lattice to an extremely subcritical one. Considering that these results are derived from the assumption of an infinite lattice, the addition of leakage and absorption in neighboring assemblies should result in a core that requires less than a quarter of assemblies to house guide tubes and/or control rods.

There were also results checked for dryout conditions. The filled assembly was remodeled with all of coolant salt replaced with dry air at atmospheric pressure and density. This showed a massive increase in the multiplication factor, going from 1.31 to just under 1.55. This is an increase of 18.47%. As described later in Section 6.2, this is because of the coolant salt's positive temperature reactivity coefficient. Decreasing density decreases slowing down interactions which leads to greater fission events from the higher energy flux profile. Comparatively, the same analysis was conducted without mirror boundary conditions, i.e. a single assembly on its own. This is to model an assembly say in transit between its fabrication site and the reactor. It is extremely subcritical exhibiting a multiplication factor of 0.08 caused by the extreme leakage of neutrons out of the small assembly. Even in the presence of reflectors or a containment, the individual assembly will remain subcritical. It is only when in the presence of a much larger lattice that the fuel can maintain a nuclear reaction.

## References

## 5 Materials Selection and Justifications

Molten salt reactors are notoriously harsh environments, involving highly corrosive fuel at high temperatures in addition to the radiation field of a reactor. These factors have made materials selection and design one of the main development thrusts of the molten salt reactor community. Historically, corrosivity of molten salts has necessitated the use of high-nickel alloys such as Hastelloy-N (such as in the MSRE [81]) which even still are not sufficient to allow for a long operational lifetime by themselves - the redox state of the fuel/coolant salt must be controlled to prevent unacceptable levels of corrosion. In a static fueled design, the inherent corrosivity of the fuel has the potential to be compounded by the high fuel temperatures (as shown by the scoping calculations in Section 4.1), however as the subsequent calculations will show, with proper redox control, not only are high nickel alloys not required, but conventional stainless steel 316H may be used as a clad and experience minimal corrosion, allowing for a long operational plant lifetime.

### 5.1 Methodology and Relevant Considerations

Why Thermochimica is needed in the first place and why we can't just use phase diagrams etc. that are directly reported in the literature (not the same temperatures compositions, etc.). Make sure to consider the fact that solubility is much lower at the periphery of the fuel tube, because *much* lower temperature. Safety concerns with formation of solid actinides.

### 5.1.1 Materials Under Consideration

Due to the time constraints of this project, it's not feasible to consider every reasonable material, so at the outset some considerations about our design were used to select candidate materials for which the justification is given below.

#### 5.1.1.1 Structural Materials

When developing a next-generational reactor design, it is important to take a look at upcoming and potentially exotic structural materials. Selecting materials that show resilience under high neutron flux and temperature while maintaining strong thermal performance is critical to the operation of a molten salt reactor. One such material to take a look into was the use of ceramics. Although they have high thermal resistance, they in general have much lower thermal conductivity than their metal counterparts.

Silicon carbide has also been proposed for its strength in high temperature environments like that of the VHTR [13], and was considered due to the possibility of very high fuel temperatures, but as is discussed in Section 8, it was ultimately not required. Among neutronic issues with advanced materials, there are still development challenges relating to their production, measurement, and before any reactor can be built with them, there must be an established ASME code. For these reasons (along with the supporting thermal hydraulic calculations) stainless steel 316H was chosen for the structural materials of the core (the vessel, etc.) as well as the clad.

##### 5.1.1.1.a Stainless Steel 316

A typical range of compositions of various stainless steels are given in Table 3 of [14]. For stainless steel 316, the average of each composition given in the table was taken for this work, and is shown in Table 7. These compositions will be used as input to thermochemistry calculations for estimating the worst-case corrosion. In addition, ASME Code Case N-201-5 provides justification for the use of type 316H in core support structure applications up to 1089.15 K, which is lower than the expected operational clad temperature (shown in Section 8) [6].

Element	Range (wt%)	Average (wt%)	Average (mol%)
Cr	16-18	17	18.1
Ni	10-14	12	11.3
Mo	2-3	2.5	1.4
Mn	2	2	2
Si	0.75	0.75	1.5
C	0.08	0.08	0.37
Ti	-	-	-
Nb	-	-	-
Fe	Remaining	67.67	65.2

Table 7: A range of typical compositions of stainless steel 316, and their averages, taken for the purposes of this project from [14]

#### 5.1.1.2 Salt Constituents

In general, the nuclear industry has been interested in using molten salts as either a fuel and/or a coolant for decades largely due to the solubility of fission products that are volatile in conventional UO<sub>2</sub> fuel, and because of their favorable thermophysical properties (high thermal expansion, heat capacity, and boiling points). In addition molten salts have been successfully used in solar cogeneration plants as a heat storage fluid since 2009 [3]. From a technical standpoint, the definition of a salt is quite broad, and can apply to salts constructed from rare elements, or even organic molecules such as acetate, but these are rarely practical for industrial use. For nuclear applications, chloride and fluoride based salts are most commonly considered, while nitrate salts are primarily used in solar cogeneration. Recently, iodine and bromine-based salts have also been considered for nuclear applications [12].

### 5.1.1.2.a Exclusion of Bromides and Iodides

Data availability is already an issue for most molten salts as they are difficult to measure (have high melting points, and some sublimate at atmospheric pressure or are otherwise volatile) but for bromides and iodides, as they have only recently been considered for nuclear applications, there is an extreme lack of data on basic thermophysical properties. In addition, bromides and iodides are generally inferior for wasteburning and in terms of neutronics [12].

### 5.1.1.2.b The Coolant Salt

In general, fluoride-based molten salts are more suited to use as a coolant due to their lower melting temperatures, higher thermal conductivity, and *much* higher heat capacity, so a fluoride-based coolant was chosen. It then remains to choose the endmembers of the salt (e.g. KF, LiF, etc.) and later their exact compositions will be obtained via constrained optimization.

In [31], Scott argues that LiF should be excluded because enrichment of Li to prevent tritium production is costly, and even with 99.9% enriched Li, ORNL still had tritium issues (in addition, lithium enrichment can lead to severe environmental pollution). However, LiF is important for maintaining a reasonably low coolant melting point. Not only does a higher melting point require more costly heaters for startup, but it also decreases the heat transfer capabilities of the coolant (by decreasing the  $\Delta T$ ). Scott claims that the following coolant salt (without LiF) ZrF<sub>4</sub>-NaF-KF (42-10-48 mole%) has a remarkably low melting point of 658 K, however the authors' were not able to recreate this result using thermochemistry calculations, and LiF was *necessary* for achieving a reasonable melting point. This discrepancy could be due to a different choice of thermochemistry solver or perhaps a different database, but for the purposes of this project, the use of a LiF-free salt could not be justified.

It's worth noting that more environmentally acceptable methods for lithium enrichment have been proposed such as electromigration [17], and [19] suggests that, at the very least, the effect on the neutronic performance is much less severe for a fast system like ours, and due to the lower absorption cross section in a fast spectrum reactor, it is reasonable to expect that there would be less tritium production, though this is something that would need to be investigated in the future, along with an assessment of the radiological concerns/regulations regarding tritium production in the coolant salt.

Finally, in agreement with Scott [31], BeF<sub>2</sub> was excluded because of its relatively high chemical toxicity and high cost; and similar thermophysical performance can be achieved with other salts. Aside from the exclusion of BeF<sub>2</sub>, every other fluoride salt that was present in MSTDB-TC was considered.

### 5.1.1.2.c The Fuel Salt

Due to its larger atomic number, higher actinide solubility, and favorable wasteburning characteristics [12], chloride is the salt of choice for fast molten salt systems (e.g. Terra Power's MCFR, Moltex's SSR-W), with some exceptions such as the SAMOFAR [4]. A notable exclusion is MgCl<sub>2</sub>, which is often considered due to its ability to control redox or lower the melting point of the salt, which can be a concern for chlorides which generally have higher melting points than fluorides although RbCl can also be used for this purpose, however, no thermophysical properties are currently available in MSTDB-TP, so it has been excluded. Additionally, it was determined that Zr additives would be used for redox control, so Mg is not necessary. Also, actinide chlorides were considered fixed by neutronic requirements, so only the non-actinide components of the fuel salt were considered for the optimization in Section 5.4.4.

## 5.1.2 Safety Margins

As described in Section 6.2, during startup, a nominal reactivity of 1000pcm will need to be controlled by the fuel salt alone, resulting in a required temperature increase of (using the calculated fuel reactivity coefficient at 1550 K, near the expected maximum fuel temperature at the top of the fuel tube, given in Table 15)  $\approx 53$  K. There will also be a subsequent increase in the coolant temperature, which, due to the positive reactivity coefficient of the coolant (in Table 15) will require an even larger fuel temperature rise to offset, the coolant reactivity coefficient is much smaller, around 1.6 pcm/K for each of the temperatures used in the calculation, and so was neglected. In a study performed by Bushnag [27], they assumed a worst case reactivity insertion of  $\approx 1500$  pcm. For a *much* more conservative reactivity insertion of 4000 pcm, the fuel salt temperature rise is only 228 K, so an adequate fuel salt boiling margin is 300 K, although it's likely that a cladding failure will occur before that limit is ever reached.

## 5.2 Benchmarking ThermoChimica

Though the use of thermoChimica for modelling systems is relatively simple (the user specifies a temperature, pressure, and salt composition, and thermoChimica outputs the results) the quality of the results is variable, and it is always best practice to benchmark a new tool against published results before applying it to new systems. In the following analysis, thermoChimica will be used to calculate solubility, binary phase diagrams, ternary phase diagrams, and heat capacity, melting and boiling points, so it is necessary to benchmark each of these capabilities.

### 5.2.1 The LiCl-KCl-PuCl<sub>3</sub> System

Although lithium is not under consideration as a fuel salt component, the LiCl-KCl-PuCl<sub>3</sub> system was chosen for benchmarking the calculation of binary/ternary phase diagrams, and the calculation of PuCl<sub>3</sub> solubility due to the ease of data availability in the publication [20], which gives pseudo-binary plots, ternary plots, and evaluations of the PuCl<sub>3</sub> solubility (in a eutectic mixture of LiCl-KCl 0.586:0.414).

#### 5.2.1.1 Calculation of Binary Phase Diagrams

##### 5.2.1.1.a A Note on Stoichiometry

Before proceeding with the benchmarking, it is worth noting a subtle detail in executing thermoChimica calculations. When executing a pseudo binary phase diagram calculation, the user must specify the left and right endmember compositions (and the number of composition steps to take between them). When inputting the endmember compositions (e.g. KCl and PuCl<sub>3</sub> for the case of Fig. 10) it is important to use moles rather than mole fractions. For example, if the left endmember is KCl, and the right is PuCl<sub>3</sub>, the left and right endmembers specified in terms of mole fraction vs. moles are shown in Table 8. The *correct* input is in terms of moles (i.e. shown on the right). It may seem like a minor difference, but since thermoChimica is expecting an input in terms of moles, an input in terms of mole fraction (as in Table 8) will fundamentally alter the stoichiometry of the system, and result in the wrong pseudo binary phase diagram, as shown in Fig. 10. In Fig. 10b, we see the phase diagram has the same features, but they appear at the wrong mole fractions, as compared with the reference diagram in Fig. 10c, because, as the plot titles show, they are *different* pseudo binary systems with *different* stoichiometries. We see (in Fig. 10a), however, that the input using moles produces the correct phase diagram.

Mole Fraction		Moles	
Left Endmember	Right Endmember	Left Endmember	Right Endmember
K 0.5	Pu 0.25	K 1	Pu 1
Cl 0.5	Cl 0.75	Cl 1	Cl 3

Table 8: Different specifications of the KCl-PuCl<sub>3</sub> system, i.e. in terms of mole fractions of endmember elements and moles of endmember elements

##### 5.2.1.1.b A Custom Pseudo Binary Phase Diagram Plotter

As shown in the previous section (Sec. 5.2.1.1.a), the built-in pseudo binary plotting routine in thermoChimica produces highly accurate phase diagrams (though the explicit phases in each region are not shown on the plots in Fig. 10). However, the built-in thermoChimica plotting routine is only capable of plotting pseudo binary systems involving three or less components (see [this](#) issue on the thermoChimica github repo), and thus cannot handle the pseudo-binary system (0.586LiCl-0.414KCl)-PuCl<sub>3</sub>, which is necessary for calculating the solubility of PuCl<sub>3</sub> in the eutectic KCl-LiCl salt and benchmarking against the corresponding figure in [20]. Thus a custom pseudo binary phase diagram plotting function was developed ([hosted here](#)) for this project which simply reads the thermoChimica output.json and plots the stable phases at each composition and temperature. So, in addition to benchmarking thermoChimica, it is also necessary to benchmark this new plotting tool.

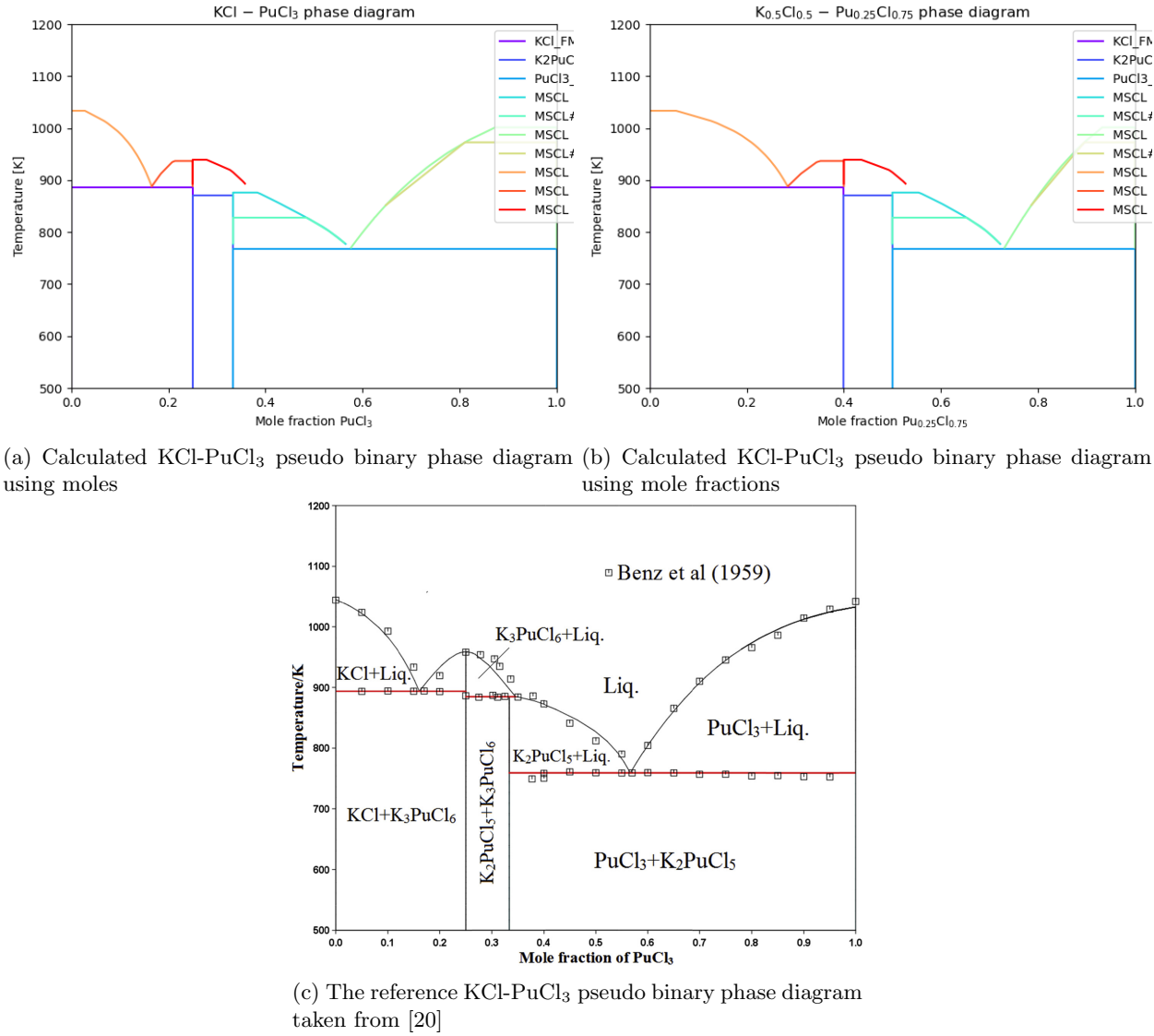
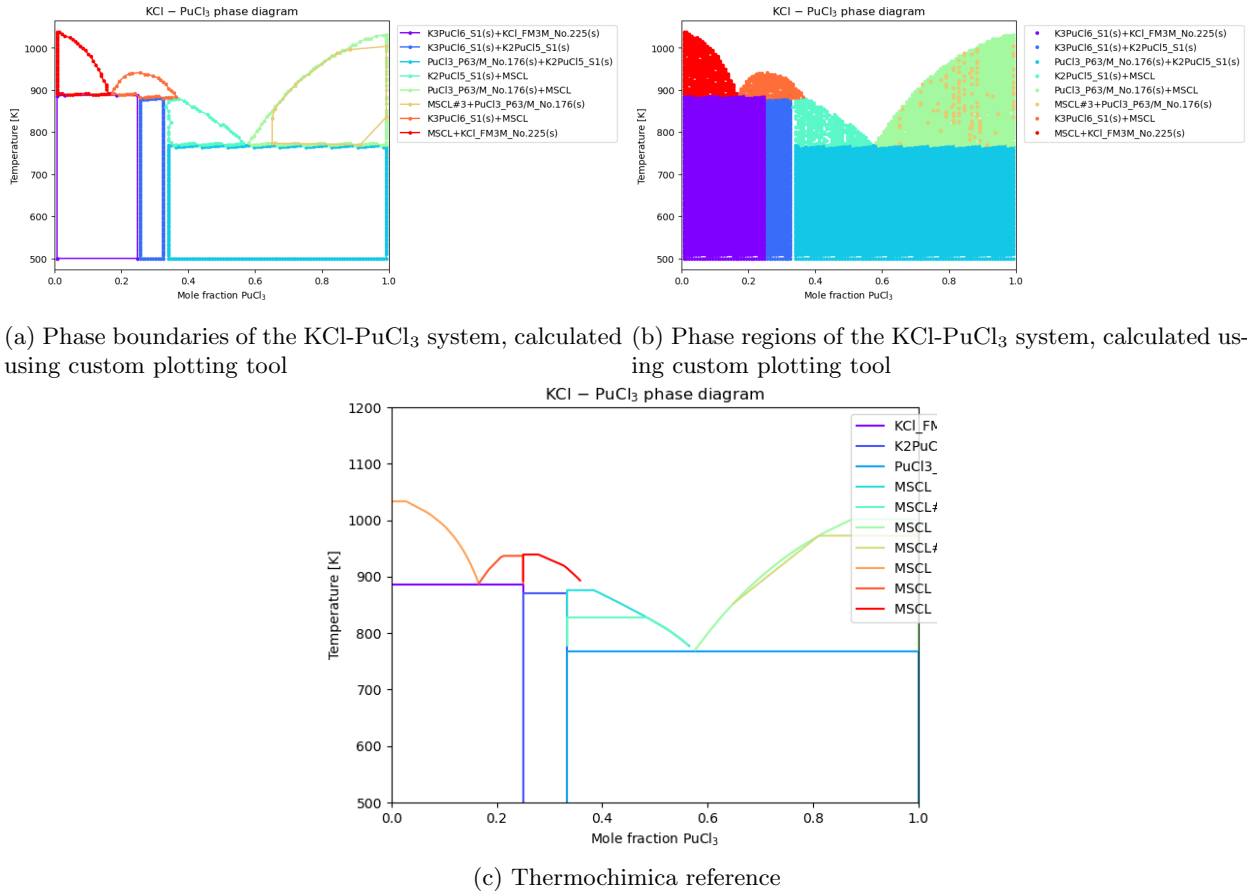


Figure 10: The importance of stoichiometry in phase diagram calculation

### 5.2.1.1.c Benchmarking the Custom Phase Diagram Plotter

First, we benchmark the custom plotting utility against thermochimica's, built-in plotting routine. Note that MSCL is an abbreviation for "molten salt chloride" and is to be compared with the liquid phase of Fig. 11c. Also, MSCL#3 is a different variety of molten salt chloride that may have been included to represent short range ordering effects in the liquid phase, but documentation on this phase is absent and conveniently it rarely appears in calculations except as a numerical artifact (see Section 5.2.1.1.d). We see that the plots generated with the custom plotting utility (Figs. 11a, 11b) replicate all of the essential features of the phase diagram calculated using the built-in plotting tool (Fig. 11c) such as the melting points of endmembers (i.e. the highest phase boundary at  $x = 0$  and  $x = 1$ ), the occurrence of the phase boundaries (e.g. between K<sub>3</sub>PuCl<sub>6</sub> + K<sub>2</sub>PuCl<sub>5</sub> and K<sub>3</sub>PuCl<sub>6</sub> + KCl), and the eutectic point at  $x \approx 0.6$ . One thing to note is that the thermochimica plot correctly distinguishes the two varieties of the K<sub>3</sub>PuCl<sub>6</sub> + MSCL phase (as shown in Fig. 10c) by extending the lower boundary all the way to the liquidous surface, while the custom plotting tool does not. For the purposes of this project, this is not an issue, and will not bar us from drawing meaningful conclusions about pseudo binary phase diagrams and solubility.

Figure 11: Benchmarks of the custom plotting tool to thermochimica for KCl-PuCl<sub>3</sub>

#### 5.2.1.1.d Numerical Artifacts

It is also worth mentioning that the MSCL#3 + PuCl<sub>3</sub> phase shown in Fig. 11a, 11b is a numerical artifact, and a result of the inherent convergence issues in equilibrium thermodynamics codes applied to molten salt systems [15]. This is further confirmed in the region plot (Fig. 11b) where the points in this “phase” are sparse, and do not form a cohesive region like the other “real” phases. These numerical artifacts are also present in the built-in thermochimica plot (Fig. 11c), and can be easily identified going forward by comparison with the reference phase diagram (in this case, Fig. 10c) or by looking at the region plot.

### 5.2.1.1.e LiCl-KCl

The plots comparing the calculated phase diagrams to those in the literature is shown in Fig. 12, from which we see that all of the important features have been preserved, even the presence of a pure solid LiCl and KCl phase and low and high  $x$  respectively (the triangular region on the sides of Fig. 12c) though it is not explicitly plotted. For completeness, note that FM3M is a name used internally by the MSTDB [8] that refers to any solid chloride (in this case LiCl or KCl), and more information on solid solution naming conventions can be found [here](#). There are a higher density of numerical artifacts in this figure, potentially owing to particular convergence issues with this system, but nonetheless the “real” phases may be distinguished in each case.

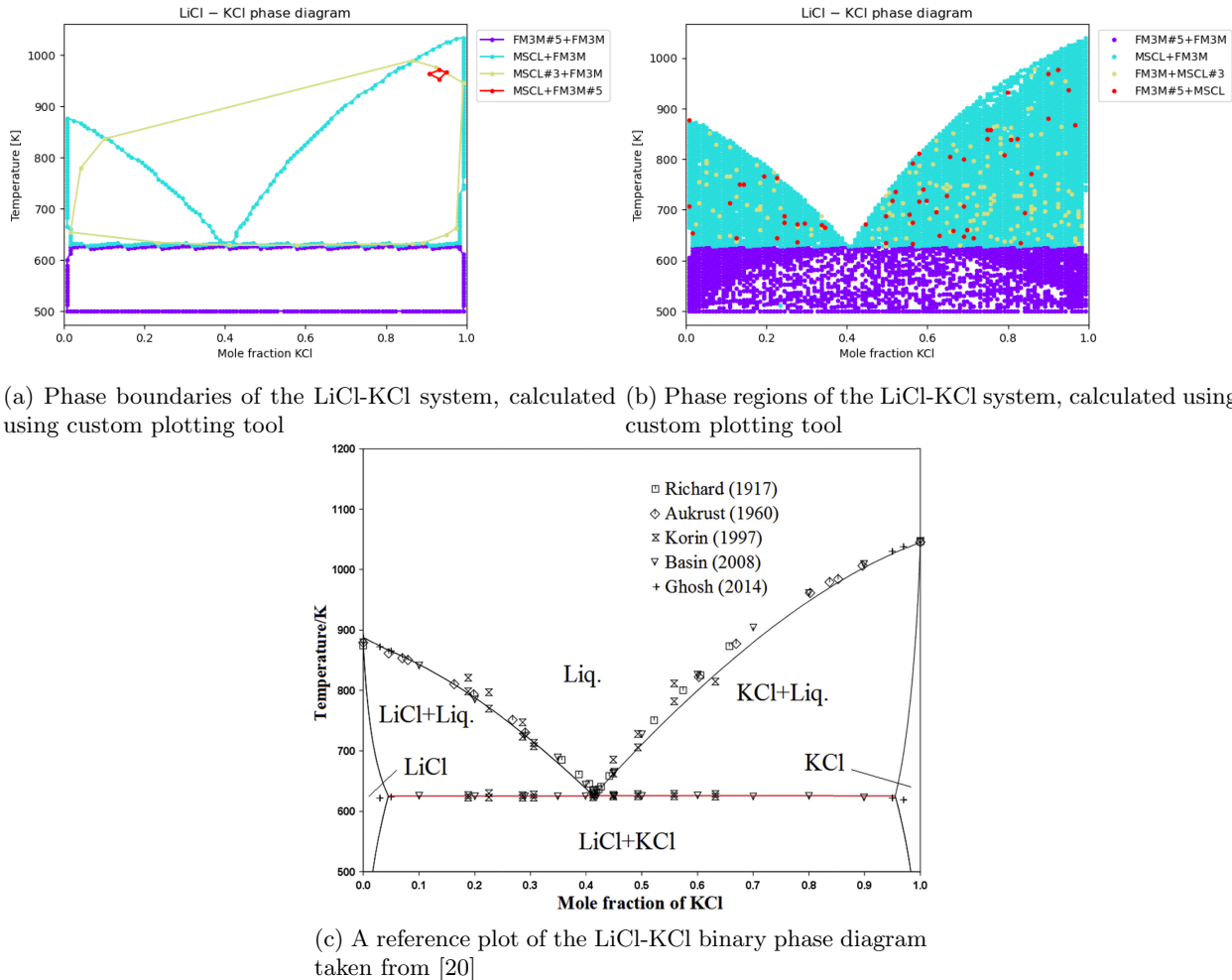


Figure 12: Comparisons for the LiCl-KCl system

### 5.2.1.1.f LiCl-PuCl<sub>3</sub>

The comparisons between the calculated diagrams and the reference phase diagram from the literature is shown in Fig. 13. Again, all of the essential features like the eutectic point, the melting points, and the stable phases have been accurately represented. Although, in this case there was a substantial amount of the MSCL#3 phase, which may be a numerical artifact or perhaps a genuine expression of the short range ordering of this binary system - in this case it is hard to determine; a more thorough literature search is recommended to determine this. In any case, assuming MSCL and MSCL#3 are both indicative of the “liquid” phase in Fig. 13c, the phase diagram is nonetheless accurate.

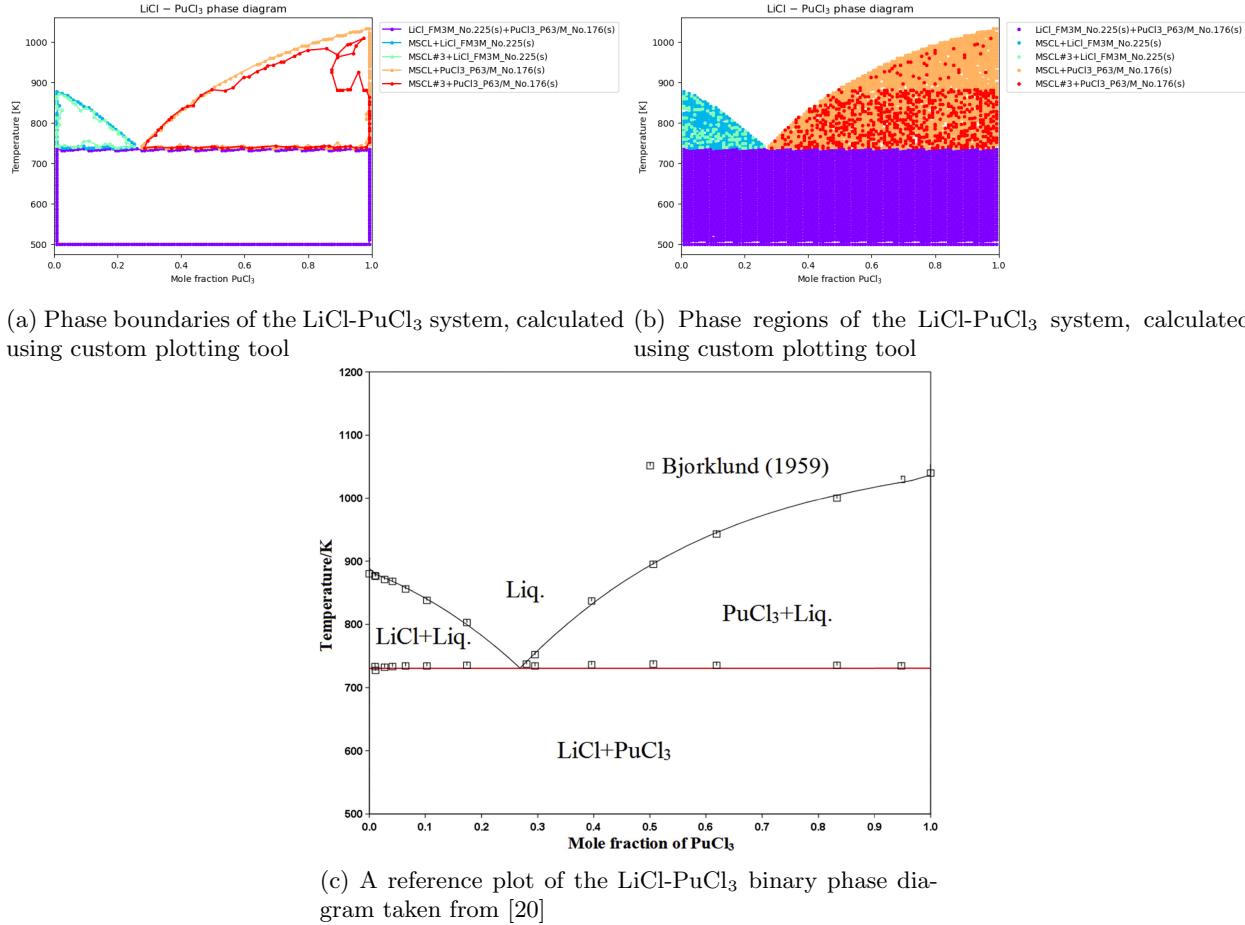


Figure 13: Comparisons for the LiCl-PuCl<sub>3</sub> system

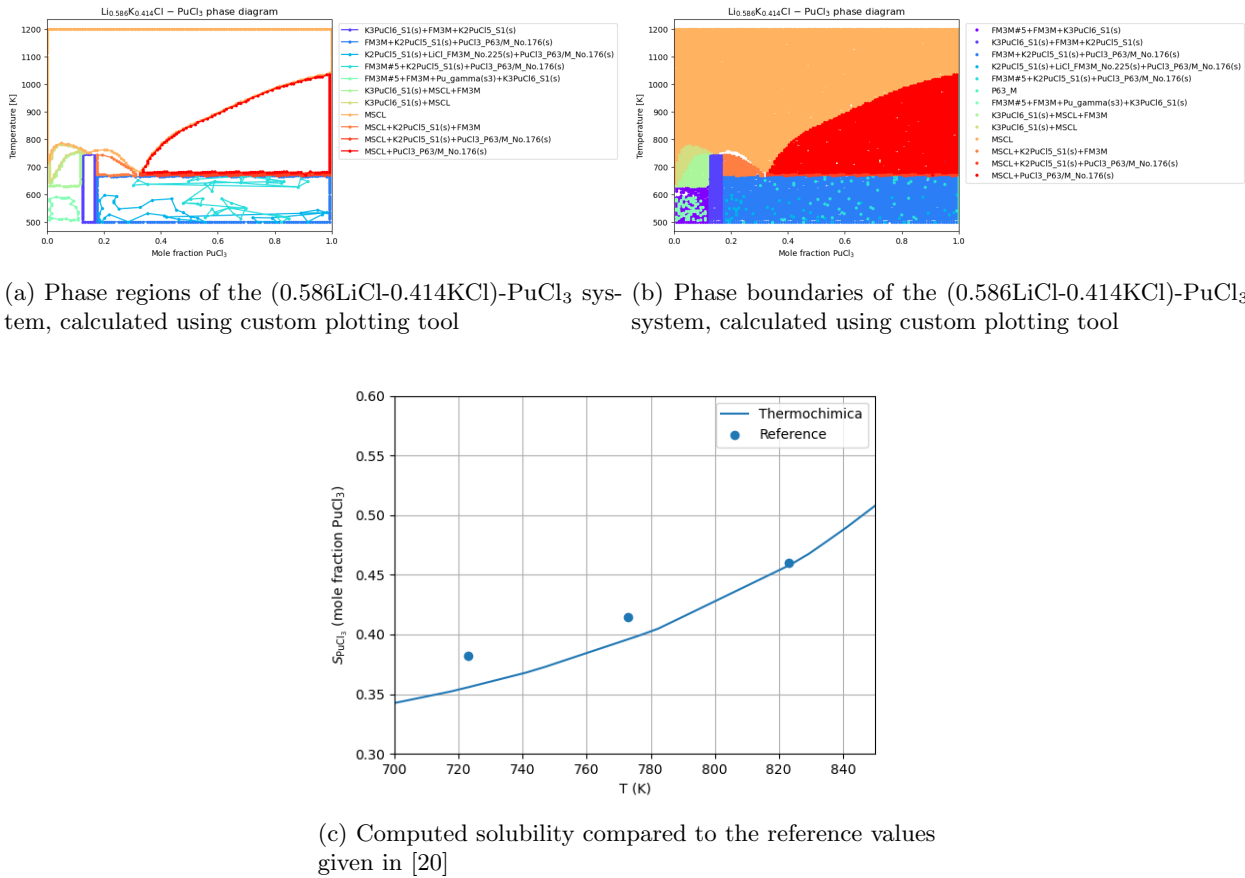
### 5.2.1.2 Calculation of Ternary Phase Diagrams

The calculation of ternary phase diagrams in thermochimica is wholly unsupported at the time of writing, so a custom plotting routine had to be developed for this project (hosted [here](#)).

### 5.2.1.3 $\text{PuCl}_3$ Solubility

For the temperatures considered by [20], the solubility of  $\text{PuCl}_3$  in the eutectic melt  $\text{LiCl} - \text{KCl}$  (58.6-41.4 mol%) is defined as the point (mole fraction of  $\text{PuCl}_3$ ) at which  $\text{PuCl}_3$  solid first forms, which is represented by the  $\text{PuCl}_3\text{-P63/M.N.176(s)}$  phase (in red) in Figs. 14b, 14a. We note that, at the temperatures considered in [20], other pure solid phases may form first, which may also be problematic from a reactor engineering standpoint (such as  $\text{K}_3\text{PuCl}_6\text{(s)}$ ,  $\text{K}_2\text{PuCl}_5\text{(s)}$ , etc. as shown in Fig. 14a) but for the sake of comparison, we adopt the same solubility criteria (which is truly indicative of Pu solubility in the salt at higher temperatures [ $T \approx 800\text{K}$  and above] where the only stable phases are MSCL and  $\text{PuCl}_3\text{-P63/M.N.176(s)} + \text{MSCL}$  as a function of mole fraction  $\text{PuCl}_3$ ). Thus solubility was calculated by finding the first intersection of the boundary of the MSCL +  $\text{PuCl}_3\text{-P63/M.N.176(s)}$  phase region with the line  $T = T_0$  for varying  $T_0$ . The result is plotted along with the reference data take from [20] in Fig. 14c, from which we see decent agreement.

It's worth noting that the MSTDB has been updated since the paper [20] was published, and could potentially contain more accurate results from recent measurements. It is also worth noting that the analysis in [20] is not based on calphad, but rather on the gibbs energy functions of only a select few salt components, so it is also plausible that, in the context of these few components, the gibbs energy functions of [20] are more accurate than those of the MSTDB, but the MSTDB gives a better holistic representation of all salts considered in the database. In short, the methodological differences between the two databases make direct comparisons difficult, but the agreement shown in Fig. 14 is promising nonetheless, and should be sufficient for benchmarking thermochimica, and especially so if we take all of our future solubility calculations with an assumed (conservative) error of 0.05.

Figure 14: Solubility Comparisons for the (0.586LiCl-0.414KCl)-PuCl<sub>3</sub> system

### 5.2.2 Heat Capacity, Melting, and Boiling Points

Following the recommendation for heat capacity calculations with the MSTDB: “While accurate heat capacity values are used for components in system assessments, heat capacity values obtained from an equilibrium calculation for a mixture may not be accurate as extended temperature-dependent terms for the component heat capacities may not have been utilized in the system optimization. When looking to use heat capacity values for higher order systems caution should be exercised and references for the MSTDB-TC system assessment should be reviewed. In general, heat capacity values for melt solutions are best obtained from MSTDB-TP.” [2] heat capacity values were taken from the MSTDB-TP using the proper expansion techniques.

### 5.3 Redox Control and Corrosion Resistance

First it’s necessary to explain the methodology for performing corrosion calculations (really worst case estimates by the nature of the equilibrium calculation, see Sec. 3.1.3). We want to analyze the equilibrium state of a mixture of, for simplicity, equal parts fuel and structural material and a fixed amount of sacrificial metal  $n_{\text{sac}}$ , and calculate the number of moles of the structural steel components that are dissolved (in the MSCL/MSFL phase) at a given temperature and pressure, denote this composition as  $n_{\text{corr}}$ . Our ultimate goal is to calculate the corrosion penetration  $p$ , i.e. the effective amount of material leached from a metal surface, which is given by

$$p = \frac{m_{\text{corr}}}{\rho_{\text{clad}} A}$$

where  $A$  is the area exposed to the corrosive salt, and  $m_{\text{corr}}$  is the mass of structural material dissolved in the salt (in equilibrium). Note that

$$\hat{m}_{\text{corr}} = \frac{\bar{M}_{\text{corr}} n_{\text{corr}}}{n_{\text{fuel}}}$$

where  $\hat{m}_{\text{corr}}$  is the mass corroded *per mole* of fuel salt, and  $\bar{M}_{\text{corr}}$  is the average molecular weight of the corroded species. Now, we can model one mole of fuel and one mole of structural material, so the above becomes

$$\hat{m}_{\text{corr}} = \bar{M}_{\text{corr}} n_{\text{corr}}$$

Now, to calculate the total mass corroded, we need to calculate the number of moles of fuel salt in an arbitrary volume  $V_f = \pi r^2 z$ . Note that

$$V_f = n_f \hat{V}_f \implies n_f = \frac{V_f}{\hat{V}_f}$$

where  $\hat{V}$  is the molar specific volume, i.e. the volume per mole of fuel salt, which can be calculated from the density and the average molecular weight of the fuel salt

$$\hat{V}_f = \frac{\bar{M}_f}{\rho_f}$$

So, the number of moles of fuel in a volume  $V_f$  is

$$n_f = \frac{\pi r^2 z}{\frac{\bar{M}_f}{\rho_f}} = \frac{\pi r^2 z \rho_f}{\bar{M}_f}$$

so, the total mass corroded is given by

$$m_{\text{corr}} = n_f \hat{m}_{\text{corr}} = \frac{\pi r^2 z \rho_f}{\bar{M}_f} \cdot \bar{M}_{\text{corr}} n_{\text{corr}}$$

Now, since  $A = 2\pi r z$ , we have

$$\begin{aligned} p &= \frac{m_{\text{corr}}}{\rho_{\text{clad}} A} = \left( \frac{\bar{M}_{\text{corr}}}{\bar{M}_f} \right) \left( \frac{\rho_f}{\rho_{\text{clad}}} \right) \left( \frac{\pi r^2 z}{2\pi r z} \right) n_{\text{corr}} \\ &= \boxed{\frac{1}{2} \left( \frac{\bar{M}_{\text{corr}}}{\bar{M}_f} \right) \left( \frac{\rho_f}{\rho_{\text{clad}}} \right) r n_{\text{corr}}} \end{aligned} \quad (4)$$

### 5.3.1 Corrosivity of Fresh Fuel

To justify the use of stainless steel 316, it is necessary to perform some bounding corrosion calculations similar to those done by Scott [31]. Due to the time constrains, this calculation was only done for fresh (containing no fission products) and *pure* fuel (no hydrogen or oxygen impurities) though the corrosion is expected to be worse for burnt fuel with impurities, but Scott shows that this difference is small [31].

#### 5.3.1.1 Parameters and Surrogates

A clad inner radii of  $r = 2.5\text{mm}$  were used, and we calculate the corrosion of stainless steel 316, whose density has a minimum of  $7870 \text{ kg/m}^3$  near its melting point [1] which we will take as a conservative estimate. We consider the corrosion of 316 stainless steel in a fuel salt consisting of 80% actinides of the composition given in Table 4, and 20%. Note that not all elements are included in the MSTDB ([here](#)), namely Am and Cm. Bessman in [9] suggests that U be used as a chemical surrogate for Am, and Bhandari in [10] suggests using Nd as a surrogate for Cm. The remaining surrogates are shown in Table 9, where the surrogate for C and Si was taken to be Fe because no elements

Element	Surrogate	Reference
Cm	Nd	[10]
Am	U	[9]
Np	U	[9]
C	Fe	-
Si	Fe	-
Mn	Fe	-
Mo	Fe	-

Table 9: Chemical surrogates for elements used in corrosion calculation along with references

in group 14 are included in the MSTDB-TC, and Fe at the very least has a similar melting point (using Al as a surrogate, which is an adjacent group, produced unphysical results). This is a crude approximation, but should have little effect on the results because C and Si are only present in small amounts.

The fuel salt used for the calculations is shown in Table 10 and was based on the fuel salt used by Scott [31]. The fuel salt is notably different from the final fuel salt composition (determined in Section 5.4.4), but the effect of the fuel salt composition was assumed to not affect the corrosion much, especially in the presence of sufficient redox control (which often has an overwhelmingly strong effect on the corrosion, as will be shown below).

Element	Moles of element
Pu	0.289756607
U	0.200000000
Am	0.027444106
Np	0.023517078
Cm	0.001890731
K	0.449999550
Cl	2.100000000

Table 10: The composition of the fuel salt used for the fuel corrosion calculation

### 5.3.1.2 Results

To obtain the results, the thermochimica calculation was run, producing a .json output containing the stable phases, and their fractions, from which the stable phases and liquid metal phases (corresponding to elements that are corroded) could be extracted. The results are shown in Figs. 15 - 17.

First, it's worth noting that there are no current regulations for the specific type of corrosion experienced in molten salt reactors, and most corrosion guidelines reference a maximum oxide layer thickness (in the case of zircaloy cladding for LWRs). That said, it's hard to say what kind of corrosion depth is expected to lead to serious degradation of mechanical properties, but the total (worst case) corrosion depth exceeded 1  $\mu\text{m}$  for fresh fuel with *no* sacrificial zirconium (as shown in Fig. 15), which is 0.2% of the 0.6 mm clad thickness. Based on concerns about corrosivity of molten salts in contact with standard materials, it was assumed that this corrosion penetration would *not* be acceptable. However, with the use of sacrificial Zr (which could be either an insert or a coating on the inner clad surface) the total (worst case) corrosion depth is reduced by nearly three orders of magnitude.

It's still unclear that this reduced corrosion penetration would be sufficient, but calculations of the fraction of corroded chromium (which is leached in the greatest proportion, as shown in Fig. 17, in accordance with the literature) can be directly compared with those of Scott, shown in Figs. 16a and 16b respectively. First, note that the results of Scott are given only in the range of 773.15 to 1173.15 K, and at the maximum temperature of 1173.15 K, the chromium concentration was around  $10^{-7}$ . At 1173.15 K in Fig. 16a the results are only pessimistic by an order of magnitude. Since at the *average* fuel temperature of 1000 K (which will be calculated in Section 8) the chromium concentration is around  $0.5 \times 10^{-6}$ , which is near the upper end of Scott's calculation, which was claimed to be feasible in [31], it will be assumed that our results imply a sufficiently low level of corrosion as well, even in

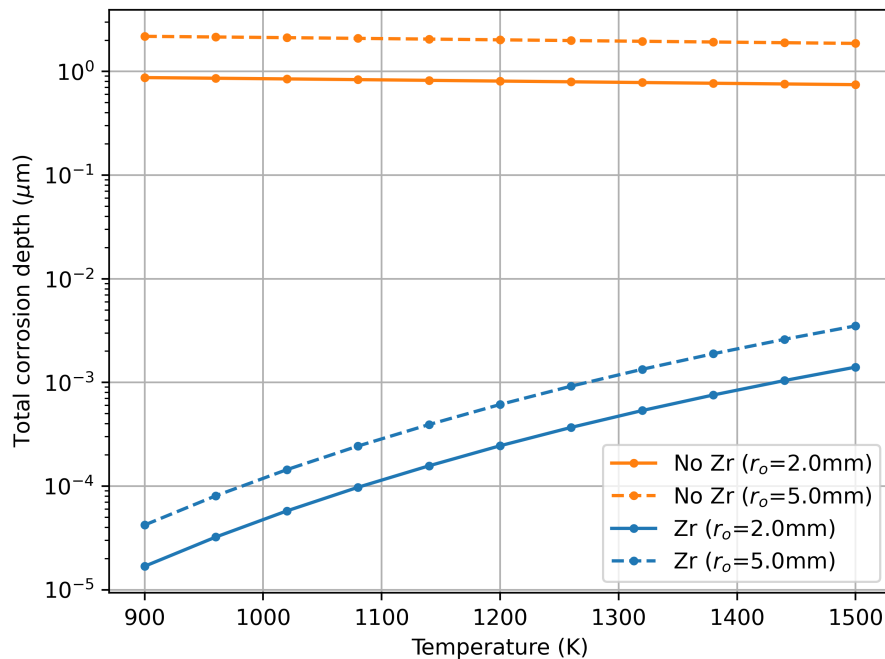
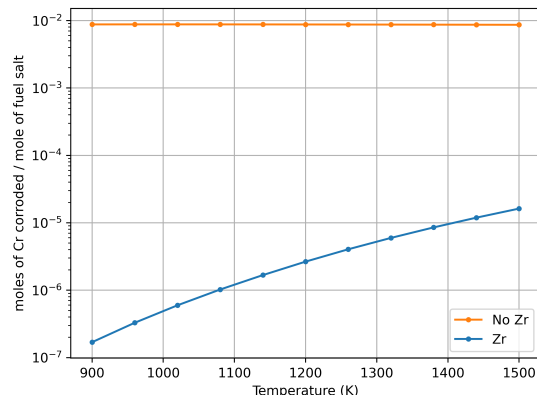
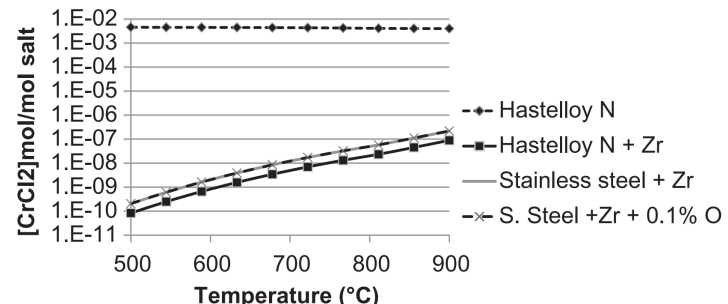


Figure 15: The total corrosion depth with and without sacrificial Zr



(a) Thermochimica calculation



(b) Reference calculation from Scott in [31]

Figure 16: Fraction of corroded chromium

the worst case, justifying the use of stainless steel, at least from a corrosion perspective, on the fuel side.

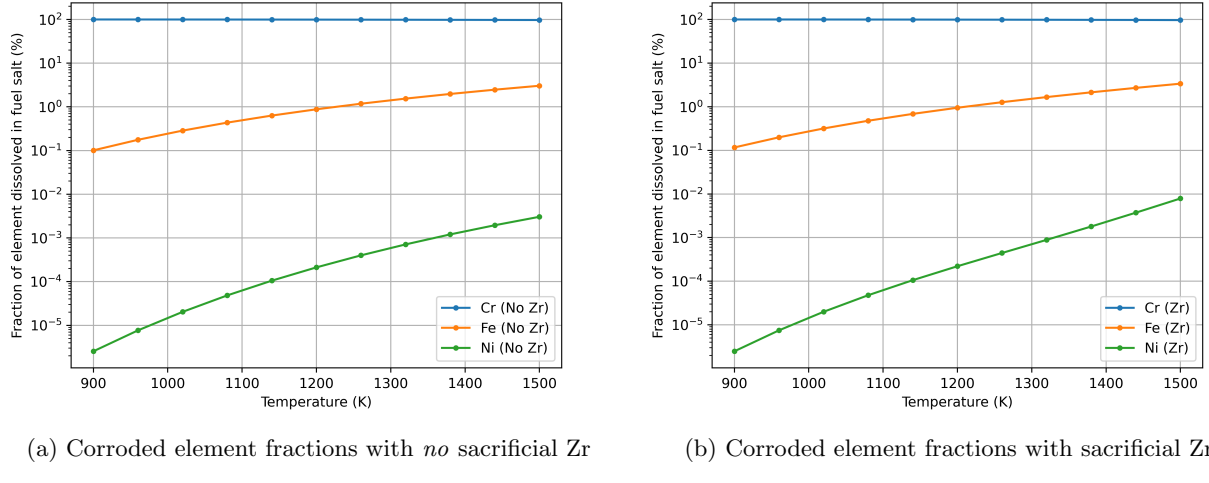


Figure 17: Composition of corroded components

### 5.3.2 Corrosivity of the Coolant

Controlling the ratio of  $ZrF_2$  to  $ZrF_4$  in the coolant salt was presented by Scott in [31] as a means of redox control for the coolant salt. To verify this, corrosion calculations were done using the final coolant salt composition (calculated in Section 5.4.3).

#### 5.3.2.1 Parameters and Surrogates

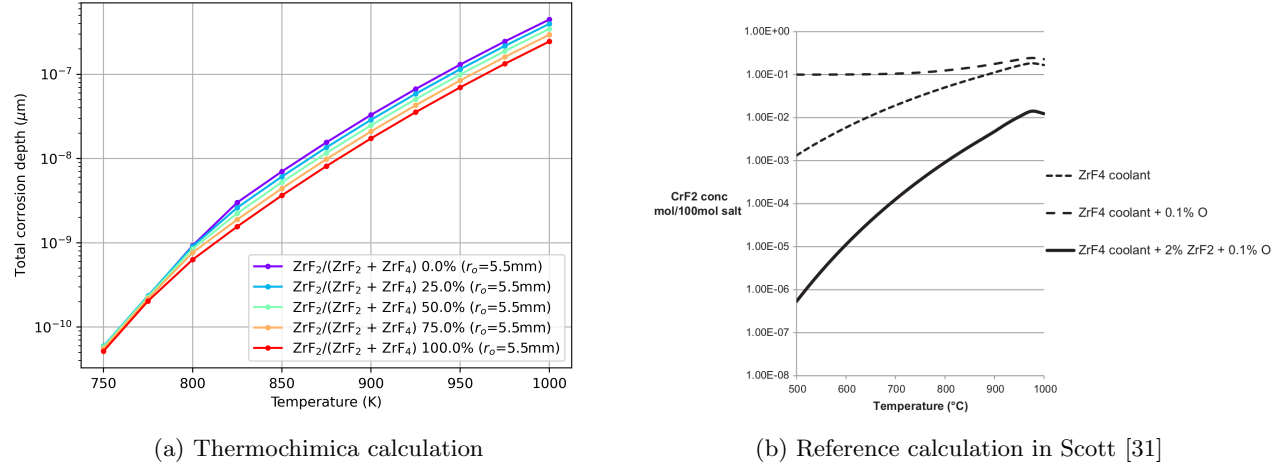
The coolant salt composition is given in section 5.4.3, and since all of the components are in the coolant salt are represented in MSTDB-TC, the only surrogates that must be used are those that were used for the components of the stainless steel given in Table 9. The fuel rod outer radius was taken to be  $r_o = 5.5$  mm in accordance with our final design parameters.

#### 5.3.2.2 Results

The results are shown in Fig. 18, and they show that for all expected coolant temperatures, the coolant side corrosion is less than the fuel side corrosion regardless of the ratio of  $ZrF_2$  to  $ZrF_4$  and is on the order of  $10^{-6} \mu\text{m}$  at most. Note that in the final coolant salt, the fraction of  $ZrF_4$  is 3.2%, so at the very most, with  $ZrF_2/(ZrF_2+ZrF_4) = 100\%$ , the coolant salt only consists of 3.2%  $ZrF_2$ , and so it might be expected that the effect of changing the ratio of  $ZrF_2$  to  $ZrF_4$  has a smaller effect than in the calculations done by Scott, which is 42 mole% Zr-based. In this case, the corrosion is manageable regardless, and it is not necessary to control the ratio of  $ZrF_2$  to  $ZrF_4$ . With these results, the use of stainless steel 316 is fully justified from a corrosion standpoint.

## 5.4 Optimization of Thermophysical Properties

Even when constrained to a specific carrier (i.e. F or Cl), and with the exclusions made before, the design space of coolant and fuel salts is *very* large. Since the thermophysical properties of the fuel and coolant salts depend on the endmember compositions, and each of the possible endmembers can be varied arbitrarily (except for the case of the fuel salt, in which the non-actinide parts are constrained to 45 mole%), the range of thermophysical properties is very large. In addition, since our design uses zirconium for redox control, and operates at higher temperatures than conventional molten salt reactors, it is not clear apriori that the optimum fuel/coolant salts chosen by other reactor designers will be applicable to our design. Further, there seem to be some discrepancies in the fuel and coolant salts used by Scott in [31] (which is most similar to our design), and the authors were not able to reproduce the claimed thermophysical properties. As a result, it's necessary to find an optimum salt composition for our specific operating

Figure 18: Effect of controlling the ZrF<sub>2</sub> to ZrF<sub>4</sub> ratio

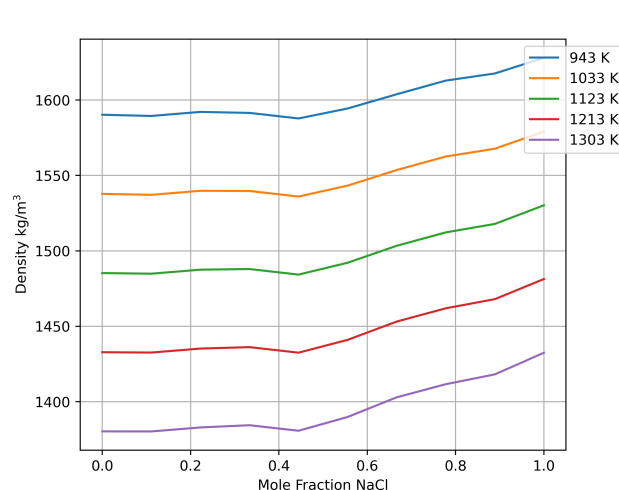
temperatures and endmembers, and there's a chance that the proper choice of composition will have a large affect on the feasibility of our design.

#### 5.4.1 Thermophysical Property Benchmarking

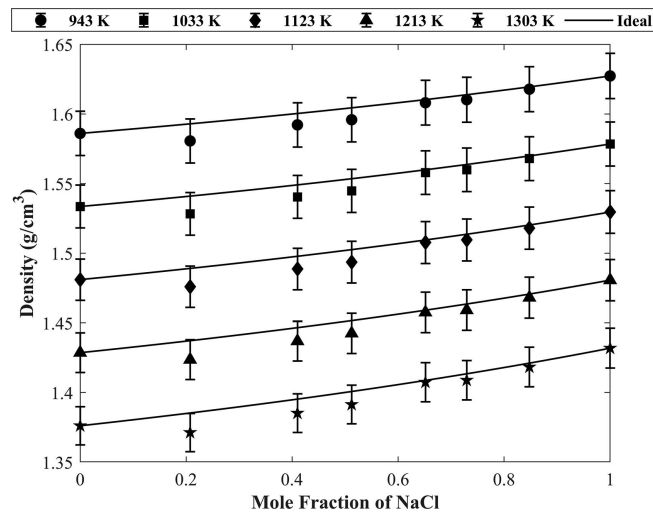
A custom python module was created for calculating the thermophysical properties of an arbitrary high order salt system based on the theoretical expansion methods detailed in Section 3.2, and that code can be found [here](#)). To benchmark these capabilities, several test cases were considered. In each of the comparisons below, note that, when there was experimental data available in the database and the composition was within some tolerance (5 mole% for each endmember), then the experimental data was used instead of an ideal/RK property estimation, which results in some jagged graphs in Figs. 19 and 20, but in any case the calculations still match the data quite well in each case. Note also that, to test the accuracy of the Redlich Kister expansion method discussed in Section 3.2, there are three test cases for which salts with RK expansion coefficients in the database were compared with experimental data. The culmination of the benchmarking below justifies the use of the custom python module as well as the theoretical expansion techniques to accurately estimate thermophysical properties of high order molten salt systems.

##### 5.4.1.1 Chloride RK Comparisons

1. Calculating the density of the KCl-NaCl binary system using the RK expansion. The results are compared with the relevant plots from [5].
2. Calculating the density of the ternary KCl-NaCl-UCl<sub>3</sub> system along the slice NaCl:UCl<sub>3</sub> = 0.25:0.75, again the results are compared to corresponding plots from [5]

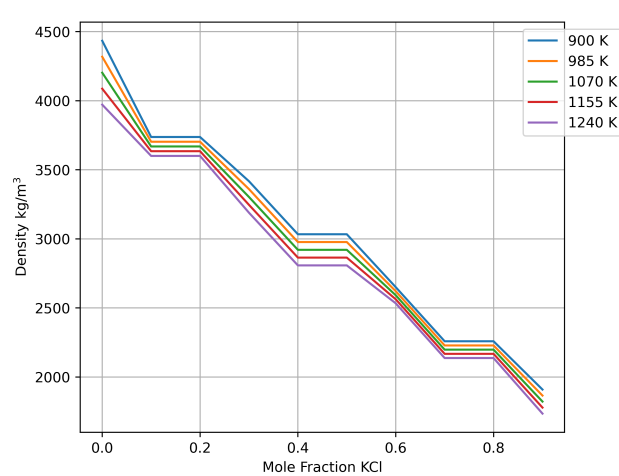


(a) Calculated thermophysical properties

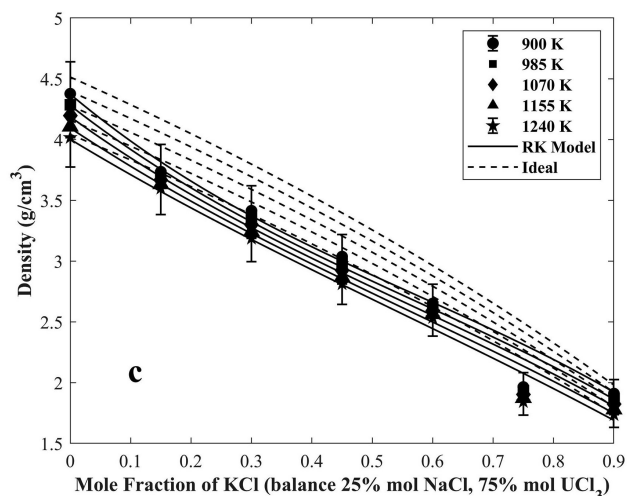


(b) Experimental data from [5]

Figure 19: Comparisons of calculations of the density of the KCl-NaCl pseudo binary system with experimental data



(a) Calculated thermophysical properties



(b) Experimental data from [5]

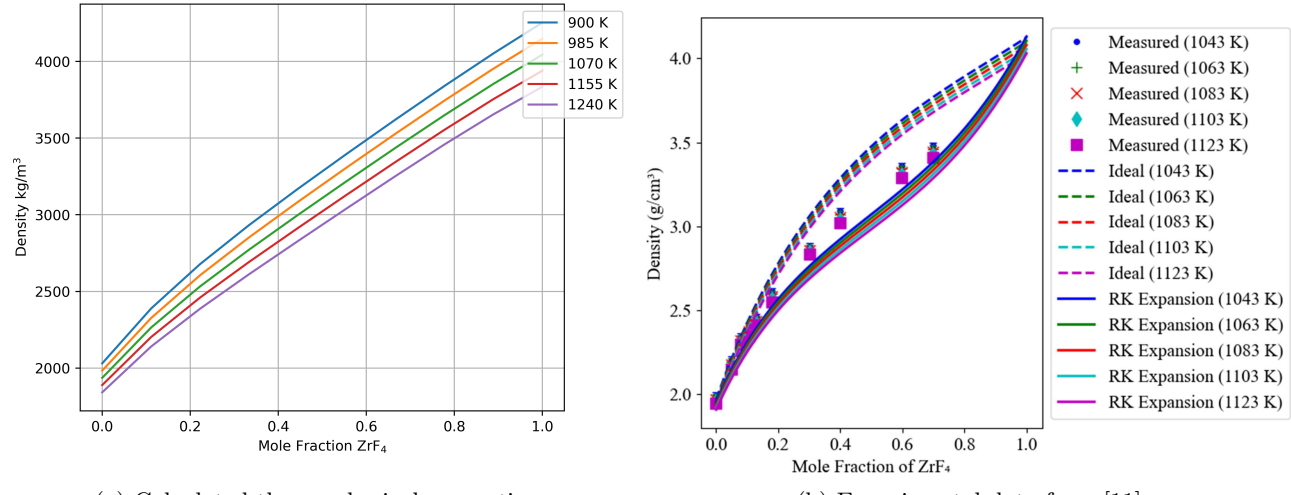
Figure 20: Comparisons of calculations of the density of the ternary KCl-NaCl-UCl<sub>3</sub> system along the slice NaCl:UCl<sub>3</sub> = 0.25:0.75 with experimental data

#### 5.4.1.2 Fluoride RK Comparisons

- Calculating the density of the ternary NaF-LiF-ZrF<sub>4</sub> system along the slice NaF:LiF = 0.4:0.6. These results are compared to plots from [11]

#### 5.4.1.3 Heat Capacity

- The heat capacity of the following pseudo binary systems was calculated and compared to the data given in [7]:



(a) Calculated thermophysical properties

(b) Experimental data from [11]

Figure 21: Comparisons of calculations of the density of the ternary NaF-LiF-ZrF<sub>4</sub> system along the slice NaF:LiF = 0.4:0.6 with experimental data

- (a) LiF-KF
- (b) LiF-NaF

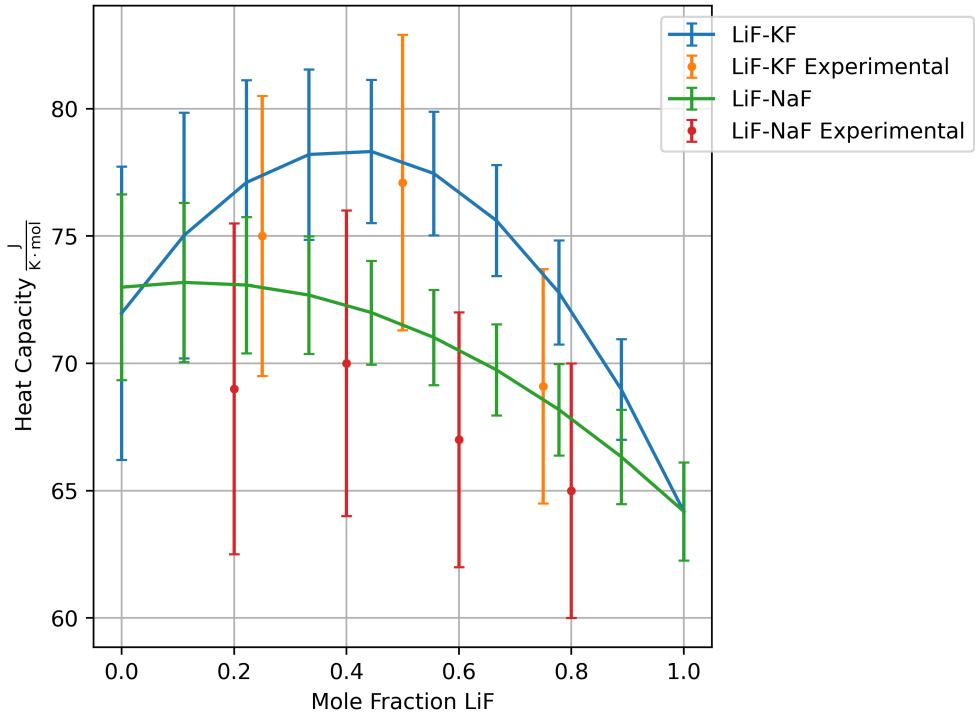
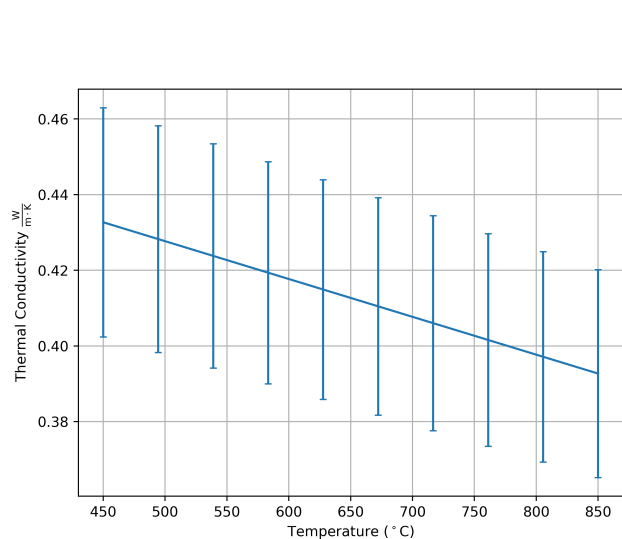


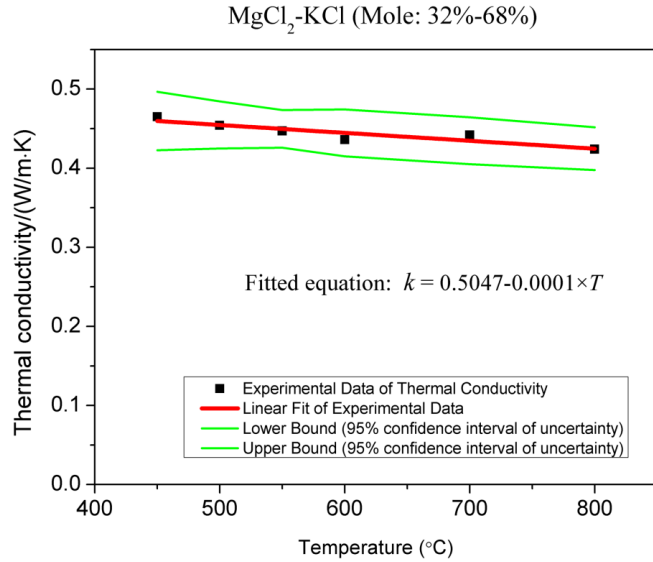
Figure 22: Comparisons of calculations of the heat capacity of the two binary systems: LiF-KF, LiF-NaF, with experimental data given in [7]

#### 5.4.1.4 Thermal Conductivity

1. The thermal conductivity of the KCl-MgCl<sub>2</sub> system was calculated, and compared with the corresponding plot in [18]



(a) Calculated thermophysical properties

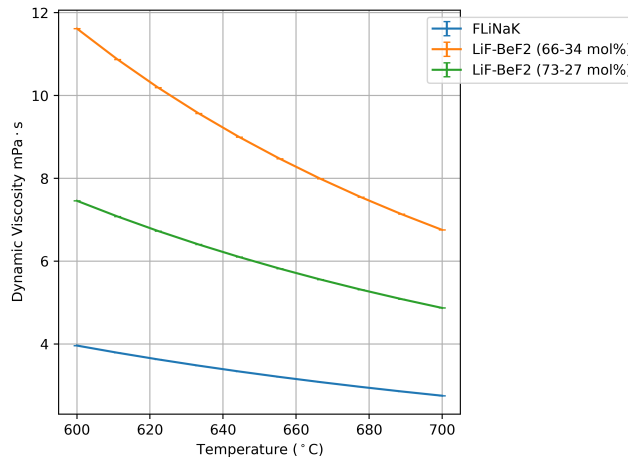


(b) Experimental data from [18]

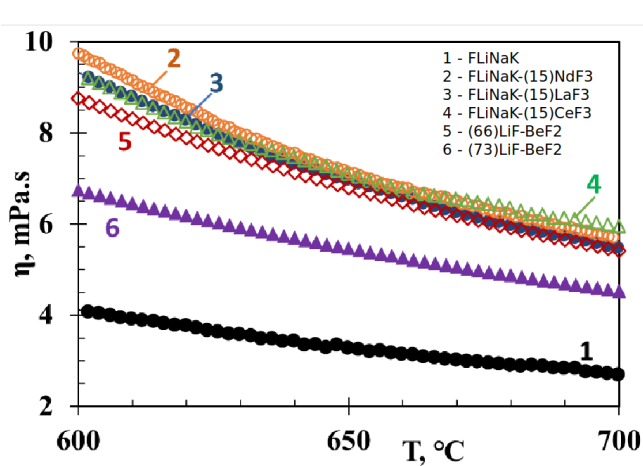
Figure 23: Comparisons of calculations of the thermal conductivity of the KCl-MgCl<sub>2</sub> system with experimental data

#### 5.4.1.5 Viscosity

1. The dynamic viscosity of LiF-NaF-KF (FLiNaK), LiF-BeF<sub>2</sub> (66-34 mol%), and LiF-BeF<sub>2</sub> (73-27 mol%) were calculated and compared to the reference [16].



(a) Calculated thermophysical properties



(b) Experimental data from [16]

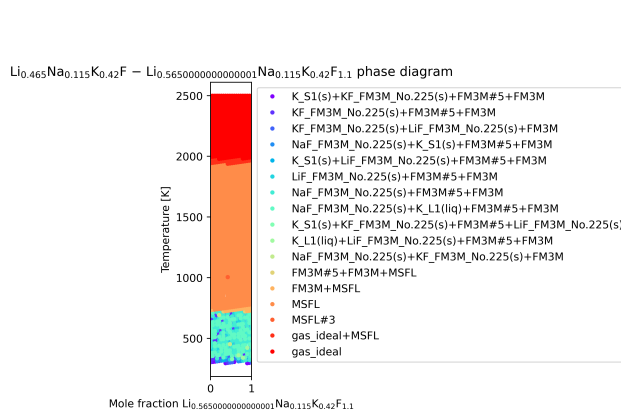
Figure 24: Comparisons of calculations of the dynamic viscosity of LiF-NaF-KF (FLiNaK), LiF-BeF<sub>2</sub> (66-34 mol%), and LiF-BeF<sub>2</sub> (73-27 mol%) with experimental data

### 5.4.2 Melting and Boiling Point Benchmarking

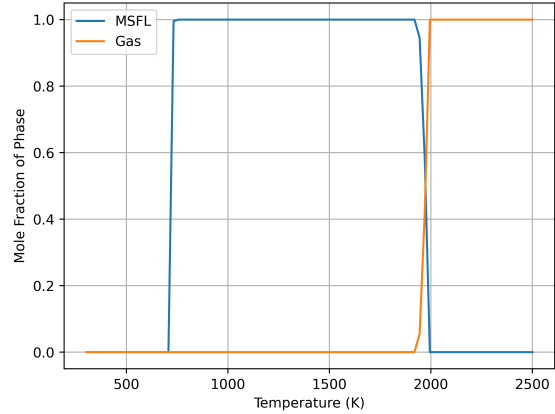
Another important capability is the calculation of melting and boiling points using Thermochimica, for which custom python code was also written (hosted [here](#)). Since everything is custom, it's necessary to benchmark the capabilities against experimental data to verify both the methods and the implementation.

#### 5.4.2.1 The Benchmark Case

For the purposes of benchmarking the calculation of melting and boiling points (of molten salts), a single test case, namely the salt LiF-NaF-KF (0.465-0.115-0.42 mol%) for which the melting and boiling points are (as listed in MSTDB-TP 3.0)  $T_m = 735$  K,  $T_b = 1843$  K (it's assumed these values are at atmospheric pressure). This benchmark just consists of comparing the calculated melting and boiling points to those found in the database. We see in Fig. 25 that the melting and boiling transition occurs sharply at a well defined temperature, so how we define the cutoff has little affect on the calculated values of  $T_m = 732$  K and  $T_b = 1944$  K. However, other salts may not have such sharp melting and boiling transitions, and in fact liquid and gas or solid and liquid phases can in general be in equilibrium over a range of temperatures (unlike e.g. water). Although this has little relevance to the final results (because the melting and boiling transitions are sharp like that in Fig. 25), the melting and boiling points were defined as the point at which the phase fraction of the liquid/gas phase reached 90%, which is a more practically useful definition of a melting/boiling point (the coolant must be mostly melted to really work well as a coolant).



(a) A pseudo binary phase diagram about the true salt composition



(b) The phase fractions of LiF-NaF-KF (0.465-0.115-0.42 mol%) as a function of temperature

Figure 25: The melting and boiling transitions for LiF-NaF-KF (0.465-0.115-0.42 mol%)

#### 5.4.2.2 A Note on Special Salts

Some salts don't have melting points (at least at ambient pressure), but rather they sublime (transition directly from solid to gas at a specific temperature). A good example of one such salt is ZrF<sub>4</sub>, which sublimates at around 1173 K (at atmospheric pressure). For these salts, the custom code will rightfully throw an error. Luckily, none of these salts were encountered in the process of constrained optimization outlined in Section 5.4.3, but it's worth noting.

### 5.4.3 Coolant Salt Optimization

The following endmembers are under consideration

1. NaF
2. KF

3. ZrF<sub>4</sub>
4. CaF<sub>2</sub>
5. LiF

#### 5.4.3.1 Optimization Criteria

The following criteria were considered for optimization

1. High heat capacity
2. Large volumetric expansion coefficient (i.e.  $\beta = -\frac{1}{\rho} \left( \frac{\partial \rho}{\partial T} \right)_p$ )
3. Low viscosity

This is inherently a multiobjective problem, so we must have a method for evaluating each salt based on its thermophysical properties. To simplify the analysis, consider the following expression for the heat transfer rate

$$\dot{q}_{cool} = 2\pi r L \bar{h} (\bar{T}_s - \bar{T}_\infty) = 2\pi r L \bar{h} \Delta T$$

where  $L$  is the core height, and  $2\pi r L$  represents the heated surface area of a single fuel rod of outer radius  $r$ .  $\bar{h}$  is the heat transfer coefficient, and  $\bar{T}_s$  and  $\bar{T}_\infty$  are the average surface temperature of the fuel rod and the average ambient coolant temperature respectively. The heat transfer rate increases if the surface temperature increases, however this is constrained by material integrity, in addition, increasing the core height or the fuel rod radius will also increase the heat transfer rate, but doing so will lead to higher temperatures within the fuel rod, and these changes are also constrained. The only variable that can be nontrivially changed is the heat transfer coefficient, which depends on the thermophysical properties of the coolant. It is for this reason that we fix  $r = 4$  mm,  $L = 5$  m, and consider a (limiting)  $\Delta T = 200$  K (and  $T_\infty = 1000$  K), however it is the hope that these values should not affect the optimum salt composition, otherwise our minimum is conditional on the assumed operating parameters.

So, for a simplified analysis, it is sufficient to optimize the heat transfer coefficient  $h$ , which is given in terms of the Nusselt number via

$$\bar{h} = \frac{\overline{Nu}_L k}{L}$$

where  $\overline{Nu}_L$  is the surface averaged Nusselt number. Note that we evaluate all coolant properties at the film temperature

$$\begin{aligned} T_f &= \frac{1}{2}(T_\infty + T_{cool}) \\ &= 1100\text{K} \end{aligned}$$

So, our objective function is

$$\overline{Nu}_L k$$

(since  $L$  is taken to be constant). Although it may reasonably be assumed that the flow is laminar, for the sake of generality, we use the following expression for the Nusselt number for flow over a heated plate (as in the previous scoping calculations for the fuel centerline temperature) which is valid for general Rayleigh number

$$\overline{Nu}_L = \left[ 0.825 + \frac{0.387 Ra_L^{1/6}}{[1 + (0.492/\Pr)^{9/16}]^{8/27}} \right]^2$$

where

$$\Pr = \frac{\alpha}{\nu} = \frac{\mu}{k/c_p}$$

and

$$Ra_L = Gr_L \Pr = \frac{g \beta \rho (T_s - T_\infty) L^3}{\mu \alpha}$$

### 5.4.3.2 Constraints

It is often the case in MSR salt design where, due to the difficulty of installing large heaters necessary to melt the coolant/fuel salt on startup, a low melting point eutectic salt is sought without regard to thermophysical properties. In this project, it is thought that heaters could be feasibly implemented, and melting temperature is not the primary objective, but rather a *constraint*. That is, we want to avoid trivial solutions that result in unrealistically high melting points while still allowing for the opportunity to choose a non eutectic point that could potentially result in better thermophysical properties.

There are also safety implications of choosing a salt with a high melting point, as coolant salt freezing can cause blockages which may disturb the flow of coolant through the core. Although not very relevant for the relatively low temperature coolant salt, it *is* desirable for the fuel salt to have a *high* boiling point to allow for higher temperatures. Although a full multicriteria optimization is outside the scope of this project, the boiling point will be taken as a constraint (a minimum boiling point) and optimizations will be performed with various constraining boiling points to examine the tradeoff between boiling point and favorable thermophysical properties (like thermal conductivity). It may be the case that increasing the boiling point necessarily degrades the thermophysical properties (like thermal conductivity) to the point where the poorer heat transfer (in the fuel) may actually lead to higher average temperatures, effectively countering the increased boiling point.

### 5.4.3.3 Choice of Solver

For convenience, `scipy.optimize.minimize` (detailed [here](#)) was used for performing the constrained optimization. Since the constraints of this system are the melting point, which depends in a very nonlinear way on the composition, most solvers available with `minimize` (such as “COBYLA” and “SLSQP”) would not converge, and so a more robust solution method “`trust-constr`” based on the “trust radius” method was chosen. This method is also better at enforcing constraints (which must be violated at some point in most constrained optimization methods to allow for greater exploration of the parameter space) which are very important to ensure a physical and practical solution.

### 5.4.3.4 Results

It was found early on that optimal solutions contained a very small mole fraction of  $\text{CaF}_2$ , and so  $\text{CaF}_2$  was excluded from the optimization at an early stage to decrease the runtime. The resulting coolant salt composition is shown in Table 11, which attained an objective function value only marginally higher than the initial guess salt  $\text{NaF-ZrF}_4\text{-KF-LiF}$  (13.0-4.0-42.0-41.0 mole %), but this initial guess was carefully chosen to be below the melting point constraint (750 K), and was the result of a great amount of trial and error, and isn’t really representative of a “randomly chosen salt”. For example, a common choice of coolant salt is  $\text{LiF-NaF-KF}$  (46.5-11.5-42.0 mole %) which produced an objective function value of -36979.6, much larger than that of the optimized salt -42548.0. The same is true for the salt proposed by Scott in [31]:  $\text{ZrF}_4\text{-NaF-KF}$  (42-10-48 mole %), which produces an objective function value of -36558, as well as a melting point of 1057.0 K, much higher than the claimed value of 658 K (although it’s unclear how they defined their melting point - it could be the case that their phase threshold for melting wasn’t 90%, as was the case in the authors’ calculation).

Endmember	Mole Fraction (%)
NaF	13.2
ZrF <sub>4</sub>	3.2
KF	41.09
LiF	41.77

Table 11: Final coolant salt composition

The final melting and boiling points of the coolant salt were:  $T_m = 721$  K,  $T_b = 1980$  K respectively, which is well under the melting point constraint, and should allow for low temperature coolant operation. Additionally, Fig. 26 shows that the melting transition occurs sharply at a single temperature, as claimed before, but it boils more gradually. The final properties of the coolant salt (used for all subsequent calculations) are shown in Fig. 27 along with their polynomial fits that were used to input thermophysical properties into the CFD calculations in Section 8. Interestingly, we see that the coolant salt has a *large* (near constant) heat capacity, a large thermal conductivity, and favorable thermal expansion properties.

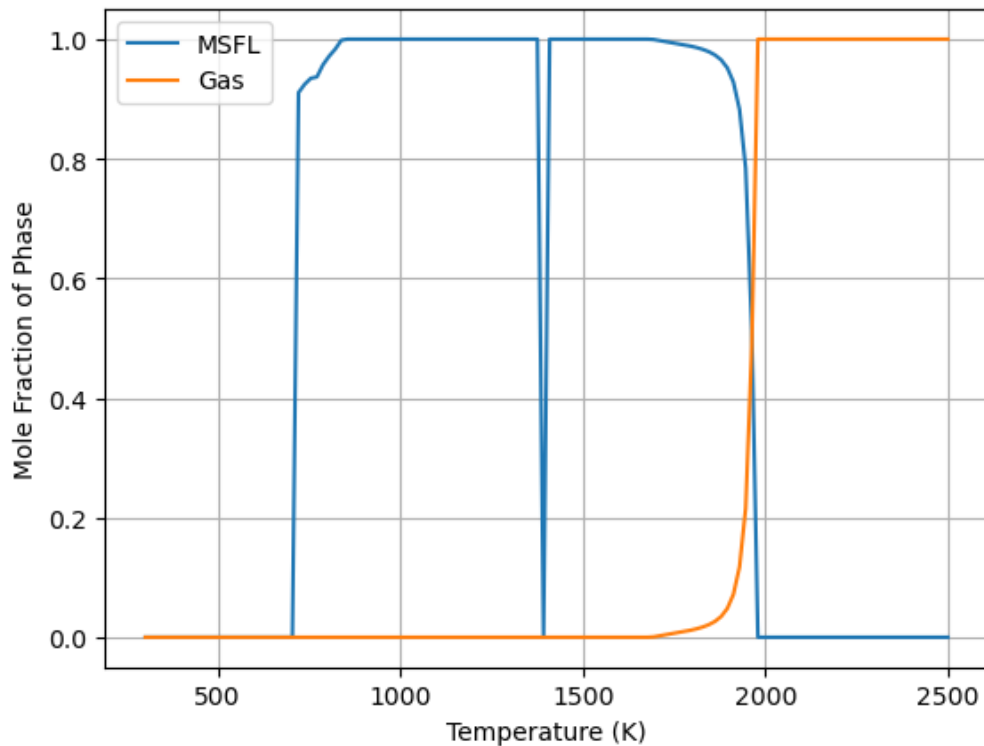


Figure 26: The phase transition of the finalized coolant salt

#### 5.4.4 Fuel Salt Optimization

For the fuel salt, a chloride salt was chosen, and has been identified as a good choice for fast systems by a number of reactor designers (e.g. Terra Power) due to its relatively high  $A$  (minimal moderation) and various fissile components and fission products tend to have high solubilities in chloride melts, making them good fuel carriers. The base components under consideration are

1. KCl
2. NaCl
3. ZrCl<sub>4</sub>
4. AlCl
5. UCl<sub>3</sub> (the most common redox state of U in chloride melts)
6. PuCl<sub>3</sub> (also the most common redox state)
7. NdCl<sub>3</sub> (only used as a surrogate for Cm)

PuCl and UCl are both present in the salt, however we will consider their ratio fixed (these components are more relevant for neutronics than thermal hydraulics) and also the fraction of actinides in the fuel salt is also constrained by criticality and fuel cycle requirements. We will perform this calculation with a fixed actinide fraction with the hope that they're soluble at the periphery of the fuel tube, and we will verify this after the fact.

For the fuel salt, the heating requirements are also a concern, and we would like the salt to not have a prohibitively high melting point, but in this design, the fuel salt will actually reach very high temperatures on the centerline, and the boiling temperature of the fuel salt becomes a relevant consideration. To achieve a high power density in the

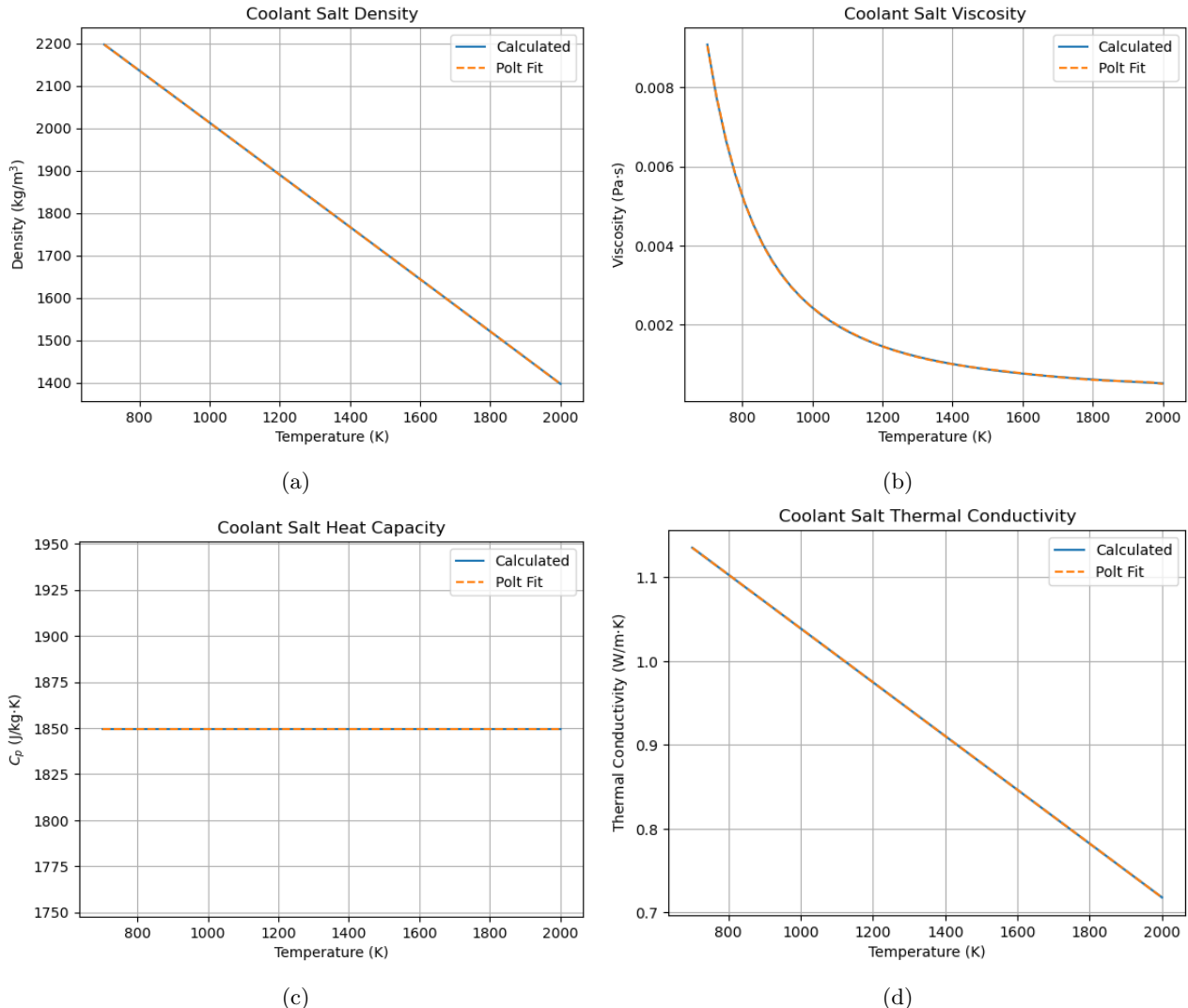


Figure 27: Final coolant salt thermophysical properties

Pure Compound	$\rho$	$\mu$	$k$	$c_p$
KCl	✓	✓	✓	✓
NaCl	✓	✓	✓	✓
ZrCl <sub>4</sub>	✓	✓	✗	✗
AlCl	✓	✓	✗	✓
UCl <sub>3</sub>	✓	✗	✗	✗
PuCl <sub>3</sub>	✗	✗	✗	✓
NdCl <sub>3</sub>	✓	✓	✗	✓

Table 12: Availability of thermophysical properties for fuel salt components

salt (comparable to a LWR at 100 kW/L) a boiling point of around 1800 K is desirable, based on rudimentary thermohydraulics scoping calculations.

Which is admittedly quite sparse, but is more than sufficient to fully calculate all of the thermophysical properties of a salt of interest (so long as we don't exclude some endmembers).

#### 5.4.4.1 Optimization Criteria

An important consideration in the fuel salt is the centerline temperature. In our design, since molten salt is a relatively poor conductor, the centerline can reach *very* high temperatures, and the constraint then becomes the fuel salt melting point. The temperature profile (assuming pure conduction) is parabolic, and the centerline temperature is given by

$$T(0) = \frac{\dot{q}r_o^2}{4k} + T_\infty + \frac{\dot{q}r_o}{2h}$$

Where  $T(0)$  is the centerline temperature,  $\dot{q}$  is the volumetric heat generation rate within the rod (our target is around 100 kW/L),  $r_o$  is the outer fuel rod radius,  $k$  is the fuel salt thermal conductivity,  $h$  is the heat transfer coefficient from the outer rod surface to the coolant salt (which is not affected by the fuel salt), and  $T_\infty$  is the bulk coolant temperature away from the thermal boundary layer near the rod surface. From this expression, it's clear that increasing the thermal conductivity of the fuel salt and/or raising its boiling point will loosen the constraints on our design. However, we also want our fuel salt to melt at a reasonable temperature (say 800-900 K). So our goal will be to maximize the thermal conductivity while keeping the melting point below 800-900 K, and the boiling point above 2000 K.

Note that the fuel composition is (representing an actinide fraction of 55 mole %):  $\text{PuCl}_3\text{-NdCl}_3\text{-UCl}_3$  (39.8-0.2-15.0 mole %) which is notably *mostly*  $\text{PuCl}_3$ , the rest of the fuel salt (45 mole %) is unconstrained. Note also that the `trust_constr` solver was also used for the fuel salt optimization.

#### 5.4.4.2 Results

Initially, the optimum fuel salt was calculated to be:  $\text{NaCl}\text{-KCl}\text{-AlCl}_3\text{-ZrCl}_4\text{-PuCl}_3\text{-NdCl}_3\text{-UCl}_3$  (25.2-14.1-3.9-2.0-39.8-0.2-15.0 mole %), however the presence of  $\text{AlCl}_3$  caused numerical issues with subsequent thermochimical calculations (likely due to poor data availability in the MSTDB-TC) so it was excluded from the optimization, and the final fuel salt composition is shown in Table 13, which has melting and boiling points of  $T_m = 788.6$  K, and  $T_b = 2164.4$  K, which is a surprisingly large operational temperature range, allowing for relatively easy melting, and a allowing for a *large* boiling margin.

Endmember	Mole Fraction (%)
$\text{NaCl}$	25.0
$\text{KCl}$	14.1
$\text{ZrCl}_4$	5.9
$\text{PuCl}_3$	39.8
$\text{NdCl}_3$	0.2
$\text{UCl}_3$	15.0

Table 13: Final fuel salt composition

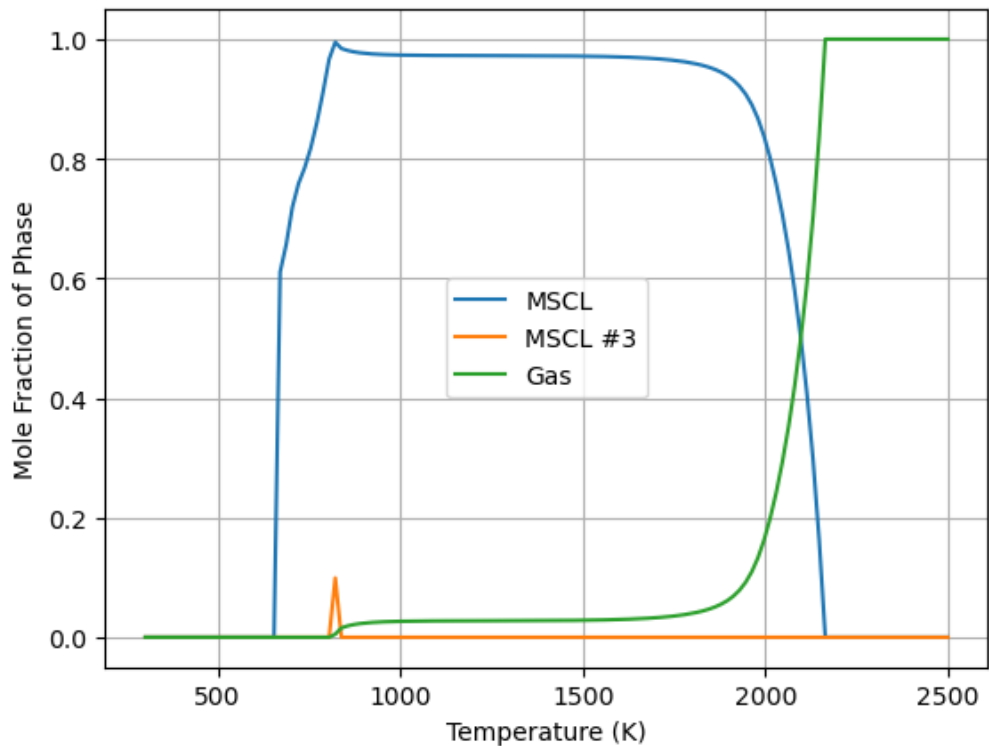
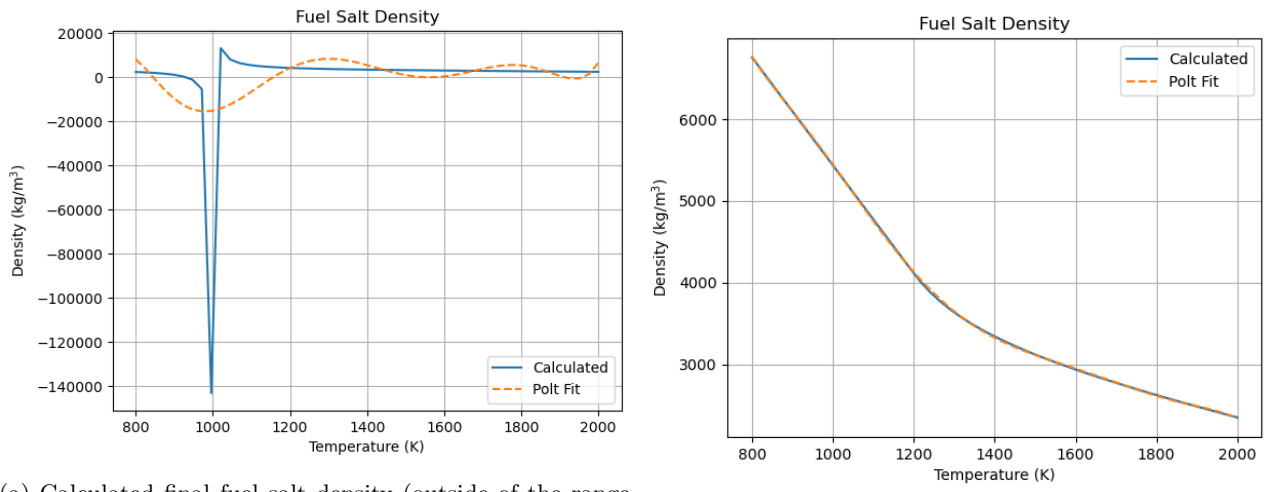


Figure 28: The phase transition of the finalized fuel salt



(a) Calculated final fuel salt density (outside of the range of validity)

(b) Linear extrapolation

Figure 29: Graphs showing initial attempts at calculating the final fuel salt density

Now, because of the way that thermophysical properties are estimated (i.e. by essentially taking a weighted sum of the thermophysical properties of the components) the estimations are not very good (perhaps not even physical) at temperatures where the property functionalizations given in the MSTDB-TP (e.g.  $\rho = A - BT$ ) are not applicable (e.g. at low temperatures *pure* PuCl<sub>3</sub> is not even liquid, so its density functionalization, which is calculated for a liquid state, is very inaccurate). In the MSTDB-TP, each functionalization is given with an applicable temperature

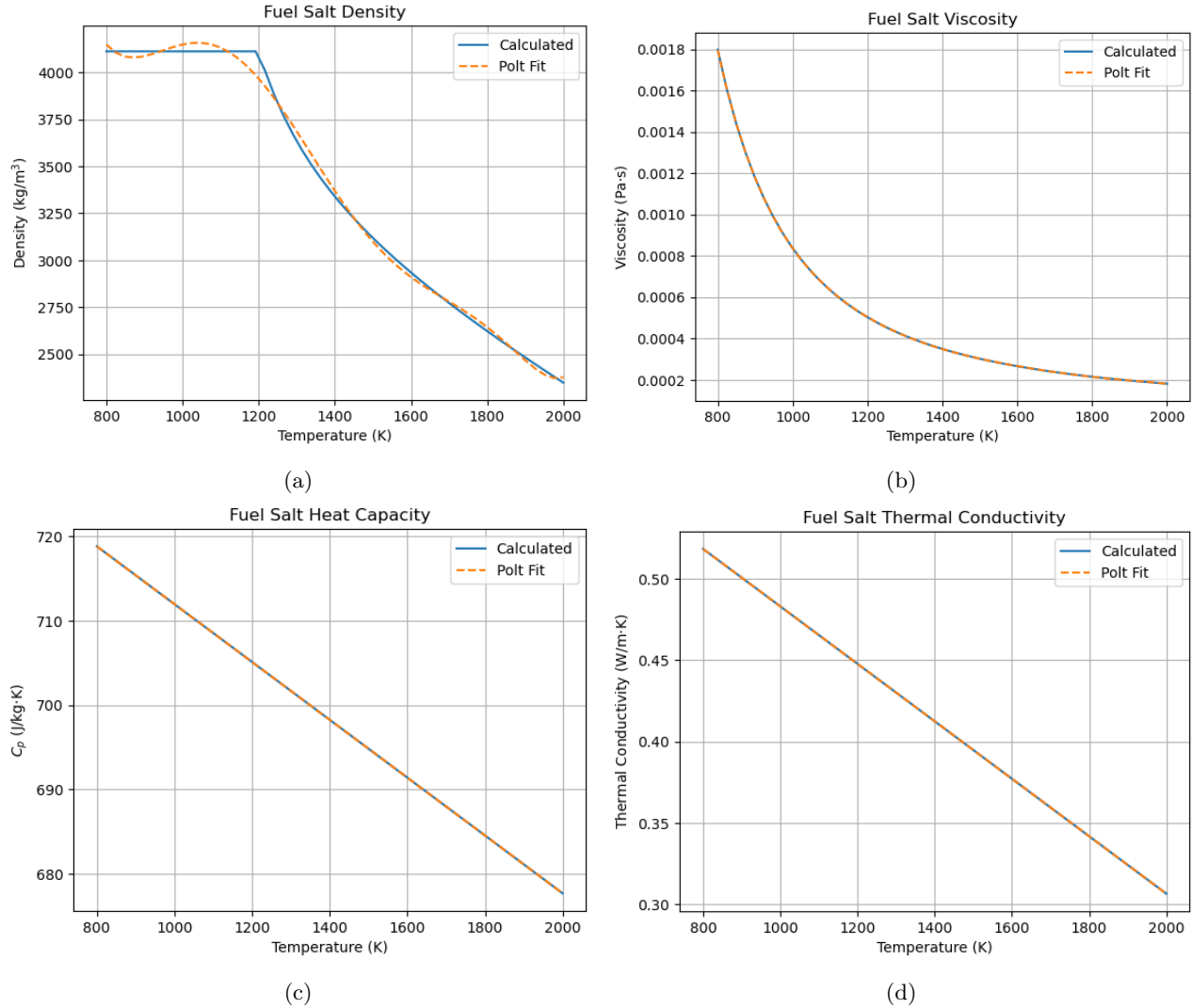


Figure 30: Final fuel salt thermophysical properties

range, and in this case the density estimation is using the component density functionalizations outside of their applicable ranges, which leads to unphysical results at low temperatures as shown in Fig. 29 (a). So, to get a density value that's usable over the entire operational range of the fuel salt (i.e. from around 800 K to 2000 K), we must extrapolate the density to low temperatures. Fig. 29 (b) shows an attempt at a linear extrapolation, which results in likely unphysically high densities at low temperatures, so a conservative constant extrapolation was performed using the (accurate) density estimate at 1200 K, this is the density function that was ultimately used for the thermal hydraulics calculations, and is shown in Fig. 30 (a) along with its polynomial fit. Although the chosen 7th order polynomial crudely approximates the density at low temperatures, it was chosen for compatibility with OpenFOAM's data format, and is nonetheless sufficient for the purposes of this project.

Compared to the coolant salt, the fuel salt has a lower thermal conductivity and heat capacity (perhaps explaining why chlorides are rarely considered over fluorides for use as coolants). However, the fuel salt has a lower viscosity (lower by nearly a factor of 6), and a higher density (which is preferable for a fuel, allowing for a higher power density).

#### 5.4.4.2.a Fuel Salt $\text{PuCl}_3$ Solubility

An important constraint is actinide solubility of the fuel salt. During the salt optimization, the actinide fraction of the salt was taken from neutronic constraints as 0.55, so we need to make sure that this fraction of actinides (mainly  $\text{PuCl}_3$ ) will be soluble in the fuel salt at the operating temperatures. The solubility of  $\text{PuCl}_3$  (the most important actinide that will constrain actinide solubility) was calculated using ThermoChimica as described previously, and the result is shown in Fig. 32. This shows that, even at very low temperatures, near the melting point of the fuel salt, the  $\text{PuCl}_3$  solubility is greater than the mole fraction of  $\text{PuCl}_3$  in the fuel salt, and hence solubility is guaranteed in all cases. The pseudo binary phase diagram used to calculate the  $\text{PuCl}_3$  solubility is shown in Fig. 31, where the phase of interest is the  $\text{PuCl}_3\text{-P}63/\text{M}_\text{No.176}(s)$  + gas\_ideal + MSCL phase, which represents solid plutonium chloride (i.e.  $\text{PuCl}_3\text{-P}63/\text{M}_\text{No.176}(s)$ ), which is defined under the solid solutions [here](#)) in equilibrium with the liquid and gas phases, representing the first point at which  $\text{PuCl}_3$  begins to fall out of solution.

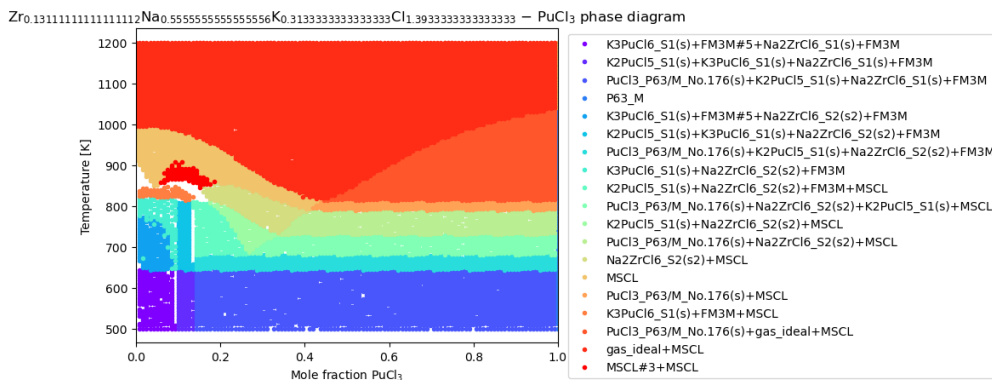
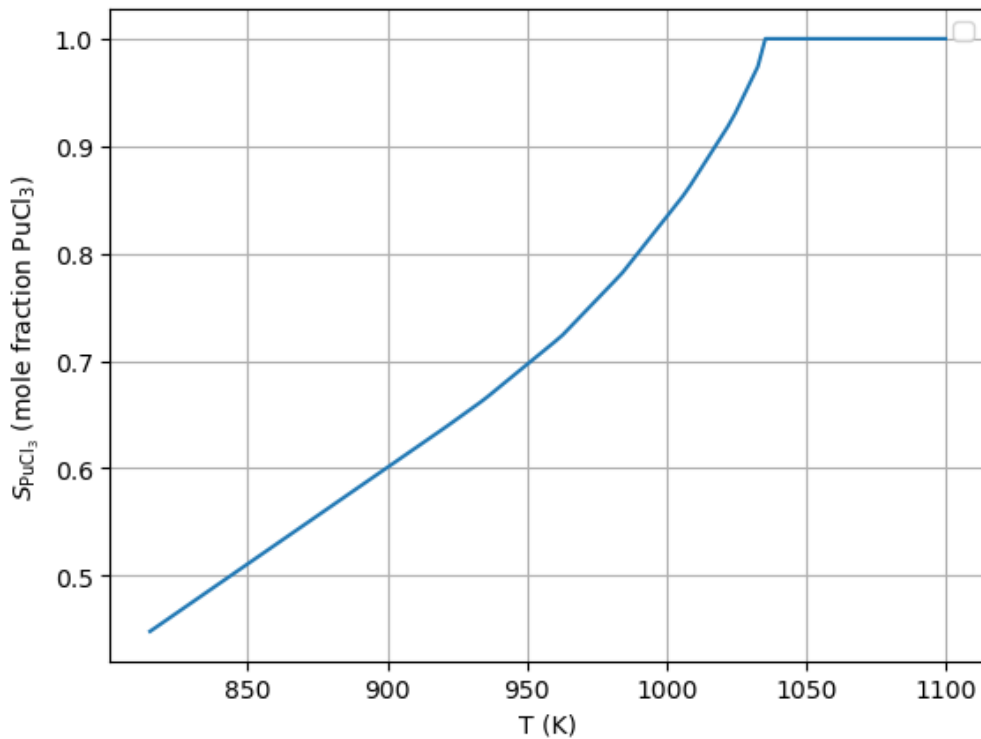


Figure 31: A pseudo binary phase diagram showing the solubility of  $\text{PuCl}_3$  in the fuel salt

Figure 32: The solubility of  $PuCl_3$  in the fuel salt

## 5.5 Summary

In this section, it was identified that, from a corrosion standpoint, plain stainless steel 316H is acceptable for use as a clad given proper redox control (via a solid zirconium insert) of the fuel salt, thus removing the dependence on advanced materials or otherwise that have yet to be qualified for use in nuclear reactors. In addition, using constrained optimization, a fuel and coolant salt were identified that satisfy the maximum melting point requirements of 750 K for the coolant and 800 K for the fuel salt, and the actinide solubility requirements for the fuel. Further, polynomial fits of each of the thermophysical properties were calculated for input to the CFD calculationss in Section 8. It remains only to show that the clad temperature is sufficiently below the code, and that the fuel centerline temperature is sufficiently below the boiling point for the chosen fuel and coolant salts, which is done in Section 8.

## References

- [1] Properties: Stainless Steel - Grade 316 (UNS S31600) — azom.com. <https://www.azom.com/properties.aspx?ArticleID=863>. [Accessed 28-02-2024].
- [2] Description &xAB; MSTDB — mstdb.ornl.gov. <https://mstdb.ornl.gov/description-tc/>. [Accessed 19-04-2024].
- [3] The Andasol Solar Power Station Project — power-technology.com. <https://www.power-technology.com/projects/andasolsolarpower/?cf-view>. [Accessed 19-04-2024].
- [4] Home - SAMOFAR — samofar.eu. <http://samofar.eu/>. [Accessed 19-04-2024].
- [5] C. Agca and J. W. McMurray. Empirical estimation of densities in nacl-kcl-ucl3 and nacl-kcl-ycl3 molten salts using redlich-kister expansion. *Chemical Engineering Science*, 247:117086, 2022.

- [6] M. Basol, J. F. Kielb, J. F. MuHooly, and K. Smit. Updating of asme nuclear code case n-201 to accommodate the needs of metallic core support structures for high temperature gas cooled reactors currently in development. Technical report, ASME Standards Technology, LLC, 2007.
- [7] M. Beilmann, O. Benes, E. Capelli, V. Reuscher, R. Konings, and T. Fanghanel. Excess heat capacity in liquid binary alkali-fluoride mixtures. *Inorganic Chemistry*, 52(5):2404–2411, 2013.
- [8] T. M. Besmann and J. Schorne-Pinto. Developing practical models of complex salts for molten salt reactors. *Thermo*, 1(2):168–178, 2021. ISSN 2673-7264. doi: 10.3390/thermo1020012. URL <https://www.mdpi.com/2673-7264/1/2/12>.
- [9] T. M. Besmann, J. Schorne-Pinto, M. Aziziha, A. M. Mofrad, R. E. Booth, J. A. Yingling, J. Paz Soldan Palma, C. M. Dixon, J. A. Wilson, and D. Hartanto. Applications of thermochemical modeling in molten salt reactors. *Materials*, 17(2), 2024. ISSN 1996-1944. doi: 10.3390/ma17020495. URL <https://www.mdpi.com/1996-1944/17/2/495>.
- [10] K. Bhandari, V. Grover, A. Roy, M. Sahu, R. Shukla, and J. Banerjee. Nd<sub>3</sub>+-y<sub>3</sub>Al<sub>5</sub>O<sub>12</sub> system: Iso-valent substitution driven structural phase evolution and thermo-physical behavior. *Journal of Molecular Structure*, 1264:133206, 2022. ISSN 0022-2860. doi: <https://doi.org/10.1016/j.molstruc.2022.133206>. URL <https://www.sciencedirect.com/science/article/pii/S0022286022008638>.
- [11] A. Birri, R. Gallagher, C. Agca, J. McMurray, and N. D. B. Ezell. Application of the redlich-kister expansion for estimating the density of molten fluoride psuedo-ternary salt systems of nuclear industry interest. *Chemical Engineering Science*, 260:117954, 2022.
- [12] B. Faure and T. Kooyman. A comparison of actinide halides for use in molten salt reactor fuels. *Progress in Nuclear Energy*, 144:104082, 2022.
- [13] Y. Katoh and L. L. Snead. Silicon carbide and its composites for nuclear applications–historical overview. *Journal of Nuclear Materials*, 526:151849, 2019.
- [14] P. J. Maziasz and J. T. Busby. Properties of austenitic steels for nuclear reactor applications. 2020.
- [15] M. Piro, S. Simunovic, and T. M. Besmann. Thermochemica user manual v1. 0. *Oak Ridge National Laboratory, Oak Ridge* 2012, 2012.
- [16] O. Y. Tkacheva, A. V. Rudenko, and A. A. Kataev. Viscosity of fluoride melts promising for molten salt nuclear reactors. *Electrochemical Materials and Technologies*. 2023. Vol. 2. № 4, 2(4), 2023.
- [17] C. Wang, P. Zhang, Q. Meng, Z. Xue, X. Zhou, H. Ju, L. Mao, F. Shao, Y. Jing, Y. Jia, and J. Sun. Electromigration separation of lithium isotopes: The effect of electrolytes. *Journal of Environmental Chemical Engineering*, 11(3):109933, 2023. ISSN 2213-3437. doi: <https://doi.org/10.1016/j.jece.2023.109933>. URL <https://www.sciencedirect.com/science/article/pii/S2213343723006723>.
- [18] X. Xu, X. Wang, P. Li, Y. Li, Q. Hao, B. Xiao, H. Elsentriecy, and D. Gervasio. Experimental test of properties of kcl–mgcl<sub>2</sub> eutectic molten salt for heat transfer and thermal storage fluid in concentrated solar power systems. *Journal of Solar Energy Engineering*, 140(5):051011, 2018.
- [19] J. Zhou, J. Chen, J. Wu, S. Xia, and C. Zou. Influence of <sup>7</sup>Li enrichment on Th-U fuel breeding performance for molten salt reactors under different neutron spectra. *Progress in Nuclear Energy*, 120:103213, 2020. ISSN 0149-1970. doi: <https://doi.org/10.1016/j.pnucene.2019.103213>. URL <https://www.sciencedirect.com/science/article/pii/S014919701930321X>.
- [20] W. Zhou and J. Zhang. Thermodynamic evaluation of LiCl-KCl-PuCl<sub>3</sub> system. *Journal of Alloys and Compounds*, 695:2306–2313, 2017.

## 6 Design Overview

### 6.1 Reactor Design

The MoSS reactor design can be described as the cross section between traditional light water reactors and the more novel future pool-type molten salt reactors. Similar to the light water reactors, a defining characteristic is the stationary fuel rods that house the fuel as well as provide a primary barrier against radionuclide release. Also similar to the light water reactors, the working fluid is heated by direct contact with the fuel rods. Although the working fluid has been replaced with a salt, it still operates in much the same manner. The coolant flows into the bottom of the core barrel from the heat exchangers in the primary loop wherein it goes through baffle plates to receive heat from the fuel rods, decreases in density, and rise to the top. The heated coolant salt can then spill over into the heat exchangers. This terminology is used because at atmospheric pressure, even with pumps, the coolant is not constrained by the top of the reactor vessel, but rather only by the sides and bottom. This is more similar to a traditional molten salt reactor in that pressure is used mostly to increase the boiling temperature of water, whereas boiling occurs at much higher temperatures for salts. Salt as a working fluid and fuel, however, come with challenges not experienced by light water reactors. For example, the corrosive environment that salts create must be carefully managed with sacrificial metals as stated in Section 3.1.3.

A sample schematic is shown as Figure 33. This image is an edited picture of the TerraPower Molten Chloride Fast Reactor due to its similar pool and primary loop structure [1]. The core proper has been edited to better show the static salt structure, wherein the yellow lines are representing fuel rods, the black lines represent the structural materials, and the crimson lines represent control rods which extend out of the core. The light green space is the coolant salt as it flows in through the core and out through the heat exchangers. The light red space at the top of the reactor vessel shows the gaseous space that exists above the equilibrium coolant level. This is the space that the vented gaseous fission products are able to reside in. This also accommodates any change in coolant salt volume due to density change without risking a greater increase in pressure. This is a temporary feature, as release valves into or out of the salt chemical processing system would be necessary to handle large increases in coolant volume, or to add more in the case of coolant condensing.

## References

- [1] URL <https://www.terrapower.com/benefits-molten-chloride-fast-reactor-technology/>.

### 6.2 Core Modeling

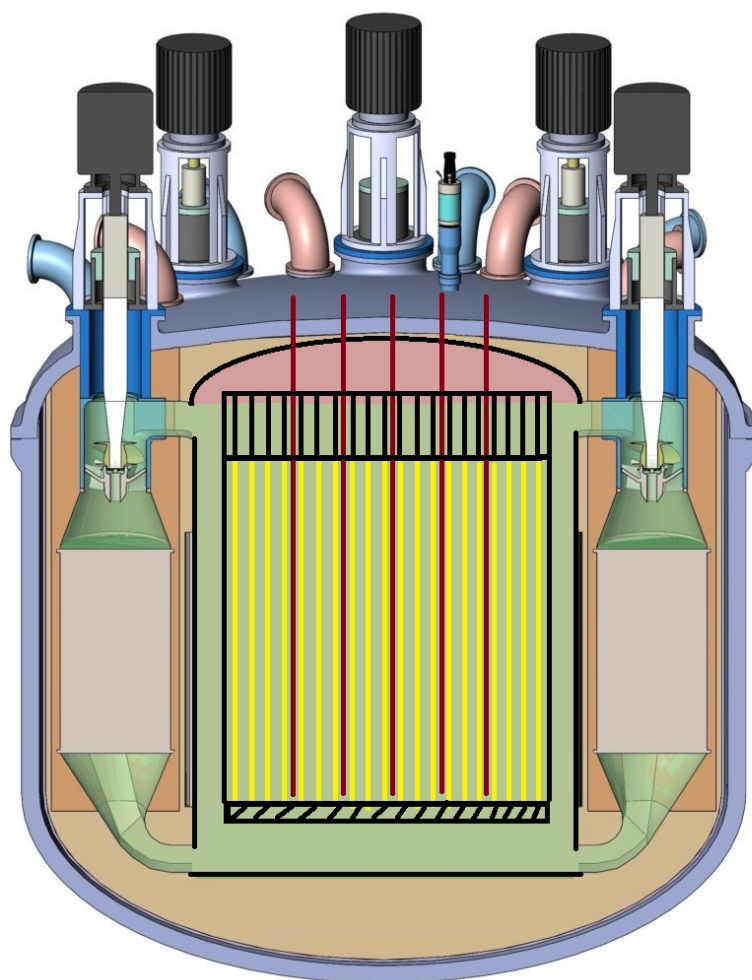


Figure 33: A basic core graphic that shows the side profile of the reactor and primary loop. The original image was taken from [1].

The trends discovered using the pincell and assembly down selection studies were utilized to analyze a full-sized core. The individual components that were described before in 4.2 and 4.3 are combined to create the greater MoSS core. A visual representation of the core barrel is shown in Figure 34. There are 211 individual assemblies made of up 18858 fuel rods to form a core that is just under 2.5 meters in diameter. The active height is 3 meters, with a total rod height of 5 meters which will allow for fuel expansion and gas venting. The reader should notice that not each assembly is colored the same in the figure. Each color corresponds to a different fuel loading region. The darkest blue color is for fresh fuel rods, and is labeled as Zone 1. The light yellow color is for the once-burned fuel rods, and is labeled as Zone 2. The teal colored fuel assemblies are for the twice-burned fuel, and is labeled as Zone 3. Zone 1 is comprised of 79 individual assemblies, with 60 being filled and 19 the guide tube types. Zone 2 is comprised of 72 individual assemblies, 54 filled and 18 guide tube. Zone 3 is the remaining 60 assemblies, 48 filled and 12 guide tube.

### 6.2.1 Control Rod Worth

Using the KENO-VI module in SCALE, the core was modeled as having infinite height using mirror boundary conditions only on the xy-plane faces. This accounts for leakage out of the core through the sides. Loading all three zones with fresh fuel, the results are as expected more moderate than that of the individual assembly modeling. The core-wide multiplication factor is  $1.16003 \pm 0.00011$  with zero control rods inserted (ARO). For the condition with 37 control rods inserted (ARI), the multiplication factor drops to  $0.985433 \pm 0.000085$  which is safely subcritical. The dryout condition for the core was also modeled, and in the ARO case the multiplication factor increases marginally to  $1.176280 \pm 0.000063$ . This, as said before, is due to the coolant's moderating effect reducing fast fission probability. In the ARI case, it is concerning to see that the multiplication factor is still supercritical at  $1.02451 \pm 0.00010$ . This would mean that the control rods do not have sufficient worth to stop criticality during a LOCA. However, it is important to note that this worth calculation is conservative in that it does not account for axial leakage, nor does it account for the decreased multiplication factor in a multi-batch core or with the optimized salt compositions. In the case of the first fuel cycle, however, it may be necessary to include more guide tube assemblies to reduce the excess reactivity in the core. Further research should also be conducted on worst stuck rod analysis to determine individual rod worth and account for its potential accident scenarios.

As for startup excess reactivity, it has been shown that burnable poisons can suppress the high central neutron flux and thus the excess reactivity that is required to reach high burnup. Research into the use of boron and gadolinium burnable absorbers is referenced from [72] and [62] wherein the researchers found that burnable absorbers in a fast, molten salt system can maintain a reactivity swing of less than 1000 pcm.

### 6.2.2 3-Batch Core

When considering the core in operating conditions, each zone will have fuel of different compositions due to the depletion from previous burn steps. To configure these compositions, an iterative process was utilized to converge on average zone compositions. These results were accomplished using the base fuel compositions shown in Tables 4 and 5. The core analysis was done in parallel with the salt selection analysis, and thus the finalized salt compositions were not available for this section. A TRITON depletion simulation was performed with the entire core set as a one-batch fuel cycle for two years. The flux averaged depletion in zone one was used to calculate the isotopic composition of the fuel at the end of the two year cycle. The top fifty isotopes by mass were saved and divided by the total mass to attain their respective weight percentages. These were then used as the material input for Zones 2 and 3 in a new TRITON depletion run. Following this simulation, the same process was used and the depleted composition from Zone 1 was set as the input for Zone 2, and the depleted composition from Zone 2 was set to the input for Zone 3. This third depletion run now contained three separate fuel compositions, one for each zone. The process was iterated one more time to further converge the results, and then a final depletion run was performed to identify the zone outputs. The results for each composition are attached in the Appendix as Table 27.

### 6.2.3 Burnup

The discharge burnup and average fluence for each core loading region is shown in Table 14. The discharge burnup is the sum of the fuel burnup after having experienced all three regions, which is averaged at 84.598 GWD/MTIHM. This is high compared to current licensed reactor limits, but for a novel liquid fuel type this may be acceptable. A

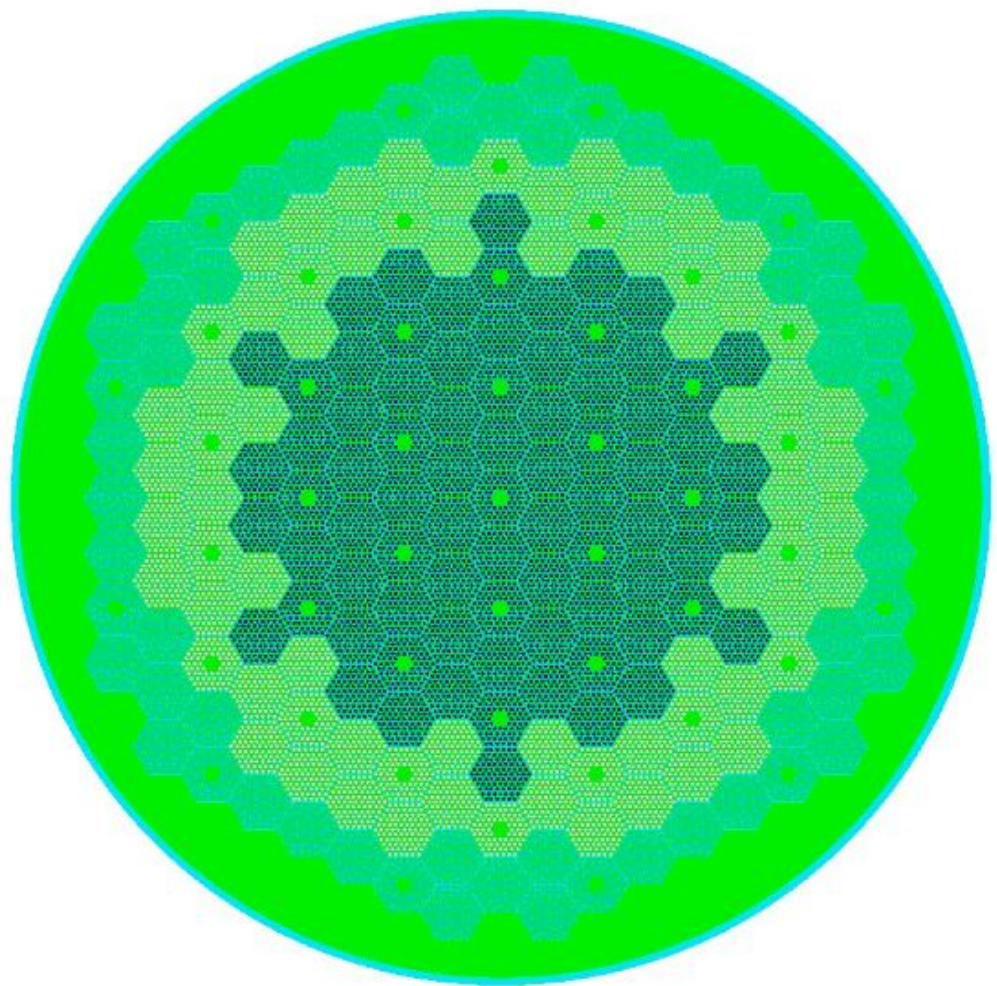


Figure 34: A visual representation of the core layout produced in SCALE and visualized using FULCRUM. There are 211 individual assemblies arranged in a symmetrical hexagonal grid comprised of 18858 fuel rods.

	Power (MW)	Flux ( $n/cm^2 - s$ )	Fluence ( $n/cm^2$ )	Burnup (MWd/MTIHM)
Z1	2.38640e+01	7.49871e+14	4.58392e+22	4.44351e+04
Z2	1.22090e+01	4.50481e+14	2.73079e+22	2.59483e+04
Z3	5.84587e+00	2.51459e+14	1.51645e+22	1.52146e+04

Table 14: Core loading regions and their average burnup and neutron fluence at 730 days at full power operation

main concern with high burnups is the affects on the material properties, and especially in a solid pellet type fuel this is manifested as cracking due to gaseous fission products and lattice deformities which can reduce heat transfer. For a liquid fuel salt, these deformities are not concerning as there was never a structured lattice. This reactor also has an uneven flux profile, mainly driven by the high leakage on the core periphery. The ratio is approximately 3:1 is cause for concern, especially due to the peaking factors it alludes to. Moreover, this results in lower burnup for the same cycle time in zone 3, and thus lower fuel utilization and actinide burning. As stated before, the use of reflectors would help limit the core leakage, and thus more equal burning can be achieved. Further analysis into the use of reflectors and absorbers would be a primary goal to achieve a flatter flux profile.

#### 6.2.4 Reactivity Coefficient

Utilizing the final optimized salts, a reactivity coefficient analysis was performed over the core geometry. The core was modeled to use all fresh fuel rods, or in other words set the system to a single batch core. The base temperatures used for this model were a fuel temperature of 1500K and a coolant temperature of 850K. The densities of each were  $3.118\ g/cm^3$  and  $2.105\ g/cm^3$  respectively. The salt compositions used are the fully optimized compositions determined in Tables 11 and ???. Running the KENO-VI module for 350 generations (50 skipped) and 500,000 neutrons per generation resulted in an infinite multiplication factor of  $1.125367 \pm 0.000063$ . In general, the reactivity of fuel is defined as its departure from the critical multiplication factor of one as shown in Equation (5). Thus reactivity in the base case was calculated to be  $0.111401 \pm 0.000063$ . In general, a temperature reactivity coefficient in  $\text{pcm/K}$  is defined as the change in reactivity with respect to change in temperature. This is shown as Equation (6).

$$\rho = \frac{k - 1}{k} \quad (5)$$

$$\alpha = \frac{\Delta\rho}{\Delta T} \quad (6)$$

To calculate the temperature reactivity coefficient of the fuel, the geometry was left alone while the fuel salt and coolant salt had their densities and temperatures varied. Since the salts are liquid and able to expand vertically higher into the fuel tube as their density decreases, the geometry of the case was not altered to preserve the number of atoms in the model. The model assumes infinite reactor height due to its mirror boundary conditions, thus there is no need to preserve atomic content when instead the geometry can be preserved with lowered atomic densities.

Table 15: Reactivity Coefficients calculated from temperature and density changes in the MoSS Reactor

	T (K)	dT	Kinf	$\pm\sigma$	$\rho$	$\pm\sigma$	$\alpha$	$\pm\sigma$
Base	850	0	1.125367	0.00005	0.111401	0.000063		
Coolant	900	50	1.126392	0.000043	0.112210	0.000054	0.000016	0.0000017
Coolant	1000	150	1.128689	0.000057	0.114016	0.000071	0.000017	0.0000006
Coolant	1100	250	1.130877	0.000057	0.115730	0.000071	0.000017	0.0000004
Base	1500	0	1.125367	0.00005	0.111401	0.000063		
Fuel	1550	50	1.114399	0.000069	0.102655	0.000088	-0.000175	0.0000022
Fuel	1600	150	1.103085	0.00006	0.093451	0.000077	-0.000120	0.0000007
Fuel	1700	200	1.079941	0.000059	0.074023	0.000077	-0.000187	0.0000005

The coolant salt was varied using a density-temperature curve calculated from the material properties. These combinations are shown in Table 15 as well as their coolant temperature reactivity coefficient outputs. The results show a weakly positive reactivity coefficient in the one sigma range of 1.4 to 1.9 pcm/K associated with the lower density. This is expected as the coolant has a moderating effect on the neutrons, which moves them into lower energy groups and away from the high fission cross sections in the fast region. Thus, decreasing coolant density would harden the spectrum and result in more fission events as seen by this analysis. This also further shows that a LOCA event would be extremely disastrous for our reactor in that it would represent a positive reactivity insertion. In comparison, for light water reactors the analogous moderator temperature coefficient would be negative.

Using the fuel salt density-temperature curve generated for the final optimized salt, three further cases were run. The values for temperature and density combinations are given in Table 15 as well as their Doppler reactivity coefficient outputs. The results show a strong negative fuel temperature reactivity coefficient in the one sigma range of -12.0 to -18.7 pcm/K. This is most likely due to the fuel density decrease which would result in fewer fission reactions in combination with the less-impactful increased absorption due to Doppler broadening. Thus, it is noted that our reactor is much more sensitive to fuel temperature and can dampen its own power swings reliably.

If the coolant and fuel change temperature at a one to one ratio, then the overall feedback reactivity would be on the order of -10 to -16 pcm/K. This is most likely an underestimate due to two primary reasons. Firstly, two results of the doppler of the results have much stronger negative reactivity feedback than the case with the fuel at 1600K, thus while we have provided a full range, there is a greater likelihood that the reactivity coefficient is more negative than we state here. The second is that a one Kelvin increase in fuel temperature would result in less than a one Kelvin increase in temperature in the coolant due to the unequal volumes, heat capacities, and overall heat transfer of the differing salts. Thus, again, it should be noted that the overall temperature feedback may be more negative than stated before. In conclusion, the MoSS reactor has a strongly negative temperature feedback coefficient, meaning that it is largely capable of inherently controlling its own power swings and hot spots without the need for active controls such as control rod insertion. These active controls provide necessary protection in accident scenarios, but are not necessary to operate in constant control of small voiding or other reactivity insertions.

## References

## 7 Fuel Cycle and Waste

### 7.1 Fuel Cycle

The fuel cycle was analyzed via a core-wide model utilizing the three batch solution determined in Section 6.2. Further, this analysis was completed using the base, pre-optimized salt characteristics. The initial fuel cycle analysis occurred in tandem with the salt optimization, thus, it was not available at the start and the authors did not have the requisite computing time to re-perform it. Instead, the trends will be extrapolated to that of the optimized composition as they showed comparable results in Section 6.2.

The fuel cycle for the core is shown in Figure 35. The reactivity swing from BOC to EOC extrapolated at 730 days (two years) is shown to be 4336 pcm, which is a reactivity drop of 5.94 pcm per day. As stated before, the combined use of burnable absorbers can more closely match a cycle wherein the excess reactivity at shutdown is zero. There was an initial drop in the multiplication factor of 0.026159 from the one-batch core to three-batch core with the pre-optimized salt compositions. Using this same multiplication factor drop and the daily reactivity losses to depletion, the second curve in Figure 35 is generated. This is a purely extrapolated set of values since the same trends are expected to be observed. The reactivity swing for the optimized salt is then 4540 pcm, which is a reactivity drop of 6.22 pcm per day. It is left for future study to quantify a formal solution for the required burnable absorber and reflector concentrations that can be garnered from this data.

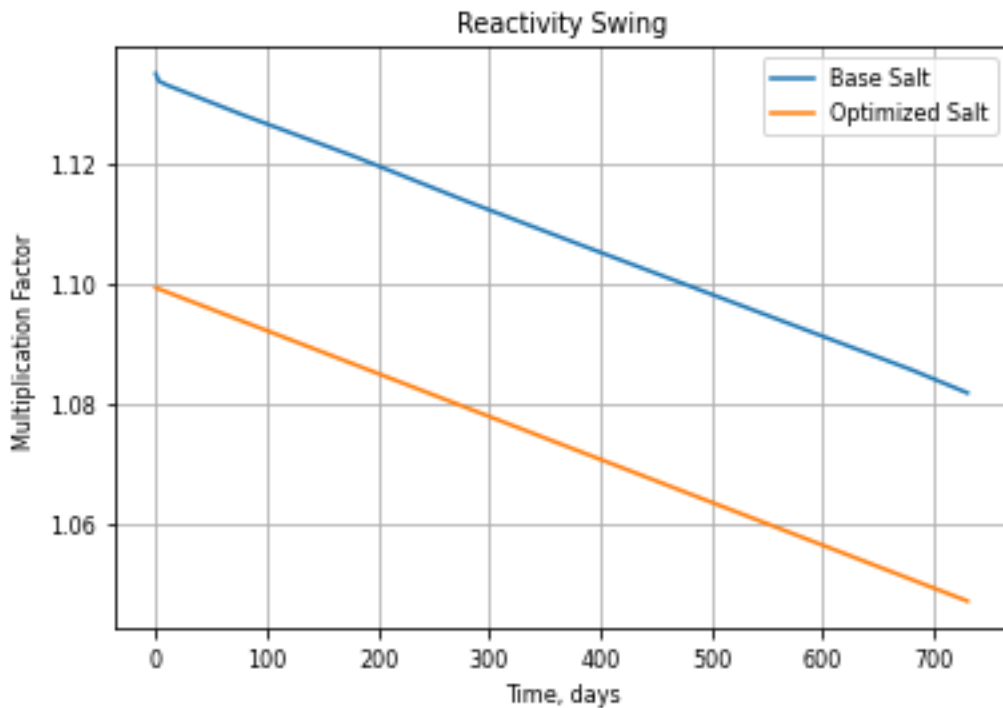


Figure 35: The reactivity swing the core experiences in a 3-batch core at HFP ARO conditions over 730 days

## 7.2 Decay Heat

Table 16: Decay Heat in Watts Thermal Post-shutdown in the MoSS Reactor

	0 year	1 year	50 year
Zone 1	1394000	38459	10346
Zone 2	734110	32270	10422
Zone 3	360320	23456	9054.5
Total Core	2488430	94185	29822.5

The decay heat from the reactor was calculated using the ORIGEN module in SCALE. The isotopic concentrations from all three zones of the three-batch core were saved after two years of irradiation at full power. Using an ORIGEN input, the decay heat generated by each zone was evaluated at shutdown, 1 year post shutdown, and 50 years post shutdown. The results are shown in Table 16. The total decay heat at shutdown is just under 2.5 MWt, which is 0.58% of the active core power. Each zone contains different amounts of initial material due to the differing number of assemblies per zone, thus normalizing to decay heat per rod in each zone would be necessary to evaluate. If this is done, at shutdown the rods in Zone 1, once burned fuel, produce an average decay heat of 197 Watts. The rods in Zone 2, twice burned fuel, produce an average decay heat of 114 Watts. The rods in Zone 3, the thrice burned fuel, produce an average decay heat of 67 Watts. The overall decay heat per rod in the core is 132 Watts. After 1 year, the decay heat drops to 3.8% of its value at shutdown to just over 94 kW total. After 50 years, the fission products have mostly all decayed away leaving the decay heat at 29.8 kW, or 1.2% of its shutdown value.

## 7.3 Waste

The discharged fuel salt was further analyzed as reactor waste. This analysis was performed using the ORIGEN module in SCALE. The isotopic concentrations from zone three of the three-batch core after two years of depletion, i.e.

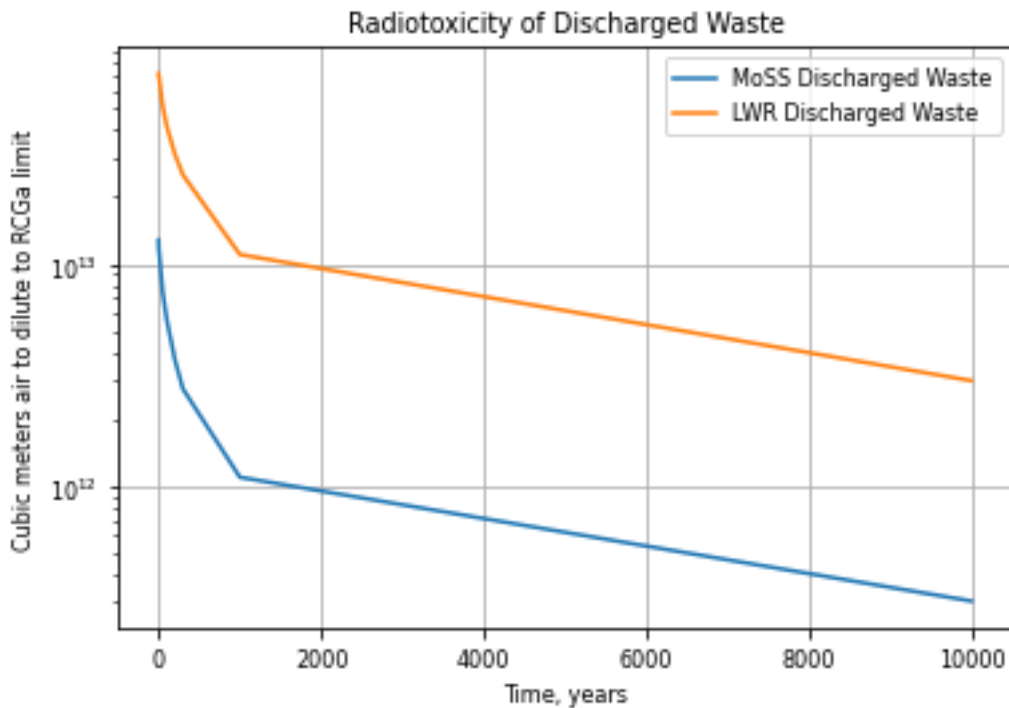


Figure 36: Radiotoxicity of 1 gram of MoSS Reactor waste compared to one gram of actinides from discharged LWR fuel

thrice-burned fuel, were saved and used as the input for ORIGEN analysis. Using the prebuilt decay transmutation library, the composition was re-evaluated at 1 year, 50 years, 100 years, 200 years, 300 years, 1000 years, and 10000 years post removal from the reactor. The values were chosen to read out in radiotoxicity measurements, specifically as airborne toxicity. This is defined as the volume in cubic meters of air required to dilute the source to the Radioactivity Concentration Guidelines for air (RCGa) [2] [1]. These radiotoxicity measurements were then normalized to a per gram of initial transuranics, such that they could be compared against one gram of the plutonium-actinide mixture used in the fresh fuel. A measurement was also made for one gram of natural uranium. The results are shown in Table 17.

Table 17: Radiotoxicity in  $m^3$  required to dilute to RCGa limit of one gram of discharged fuel in the MoSS Reactor compared against one gram of the starting actinides or one gram of natural uranium

	0y	1y	50y	100y	300y	1000y	10000y
Discharged Fuel	1.28E+13	1.19E+13	7.49E+12	5.62E+12	2.74E+12	1.10E+12	3.04E+11
LWR Discharged Fuel	7.19E+13	7.12E+13	5.14E+13	4.18E+13	2.51E+13	1.10E+13	2.98E+12
Natural Uranium	3.62E+6	3.62E+6	3.63E+6	3.65E+6	3.71E+6	3.95E+6	6.95E+6

One goal of this reactor design was the reduce the radiotoxicity in spent legacy nuclear waste. It is shown by this data that on a per gram of actinide waste, the MoSS reactor reduces the radiotoxicity to humans by 82% at shutdown and approximately 89% at 300 years post shutdown. This is an order of magnitude decrease in the radiotoxicity stemming from the breaking down of long-lived fissile actinides into comparatively short-lived fission products and light elements. Look to Figure 36 and see that the radiotoxicity curves between the MoSS reactor and LWR discharged fuel closely resemble one another. This is because the greatest portion of the radiotoxicity stems from the heavy metal actinides which decay slowly in both. The goal of reaching the radiotoxicity of natural uranium has proven to be too lofty in its ambition. It is shown that even after 10,000 years of decay, the radiotoxicity of

discharged fuel from the reactor is still over five orders of magnitudes greater than the same mass of natural uranium ore. While this is a disappointing outcome, it should be noted that uranium ore in of itself is only weakly radioactive due to its long half-life, and its toxicity reflects this. This is shown in the Appendix as Figure 55. Achieving an end to the fuel cycle through depositing discharged waste is still possible for our reactor, it will just require greater safety measures for the public compared to the uranium that exists there naturally. Alternatively, it is also proposed to refresh the discharged fuel with more fissile plutonium, allowing the mixtures to be continuously reused for future cycles.

A major concern not analyzed here is the control of fission products from the discharged legacy LWR fuel. These fission products are held in tight solid pellets inside the pressurized fuel rods. To access the plutonium and actinides for MoSS fuel, these barriers to the radiotoxic contents must be breached. During the refining and separation processes, these fission products are thus allowed to disperse outside of the barriers meant to hold them. It is pertinent to ask what happens to these radioisotopes: what harm can they cause to workers, how are they recaptured, how are the disposed of, and where can they be sent off to for safe storage. Analysing on the fission products of the MoSS fuel, we found that the radiotoxicity decreased to below natural uranium between the 200 and 300 year marks, thus whatever fission products are released from the LWR fuel will most likely need to be tracked and stored for at least 200 years. Although comparatively short to the actinides, this is still a long time span that needs further research to show that the potential harms associated with reprocessing do not outweigh the benefits of the decreasing long-term radiotoxicity.

These results, of course, does not reflect that the waste discharged from the MoSS reactor is safe. In fact, it is still highly toxic and will need to be kept under tight controls for millennia. However, it is a proof of concept that current legacy nuclear waste can simultaneously be harnessed for its latent energy while also becoming comparatively safer to the environment and humans alike.

## References

- [1] I. C. Gauld, G. Radulescu, G. Ilas, B. D. Murphy, M. L. Williams, and D. Wiarda. Isotopic depletion and decay methods and analysis capabilities in scale. *Nuclear Technology*, 174(2):169–195, 2011. doi: 10.13182/NT11-3. URL <https://doi.org/10.13182/NT11-3>.
- [2] O. R. N. Laboratory. *The Radioactivity Concentration Guidelines*. Environmental Protection Agency, 1984. URL [https://www.epa.gov/sites/default/files/2015-06/documents/fgr\\_10.pdf](https://www.epa.gov/sites/default/files/2015-06/documents/fgr_10.pdf).

## 8 Thermal Hydraulics

For this concept, thermal hydraulics have had a large impact historically, being the reason that this design was not pursued, and are probably the most constraining aspect. Previous calculations relying on simplified correlations and assuming pure conduction in the fuel salt have shown that the centerline temperature can be kept within a reasonable margin of the boiling point (i.e. Fig. 7) for a sufficiently small ( $r_o \approx 2.0$  mm) fuel rod while maintaining the power density of a conventional light water reactor. The scoping calculations performed in Section 4.1 were done using reference fuel and coolant salt compositions, and it's necessary to redo them with the finalized fuel and coolant salts, which at the very least have *very* different melting and boiling points.

The revised centerline calculation is shown in Fig. 37 and shows just how much extra margin the increased boiling point gives. However, neutronic constraints require a fuel tube radius of  $r_o = 5.5$  mm, for which the boiling point would be exceeded unless the power density were reduced by nearly a factor of 4, providing a thermal power of  $\approx 100$  MW<sub>t</sub>, a pitiful amount given the required size and capital of the core design. Also, there was a glaring omission in the calculations of Section 4.1: the exclusion of the clad temperature. The fuel boiling point is also constraining, but given that the calculations assumed pure conduction in the fuel tube, and the relatively small radius, we might assume very high clad temperatures, and that's what Fig. 38 shows. In fact, the clad temperatures are over the code for stainless steel 316H again unless the power density is decreased by a factor of 4.

However, these initial scoping calculations were conservative, and assumed pure conduction in the fuel salt, when in actuality there will be free convection within the rod that will increase the heat transfer, potentially decreasing the

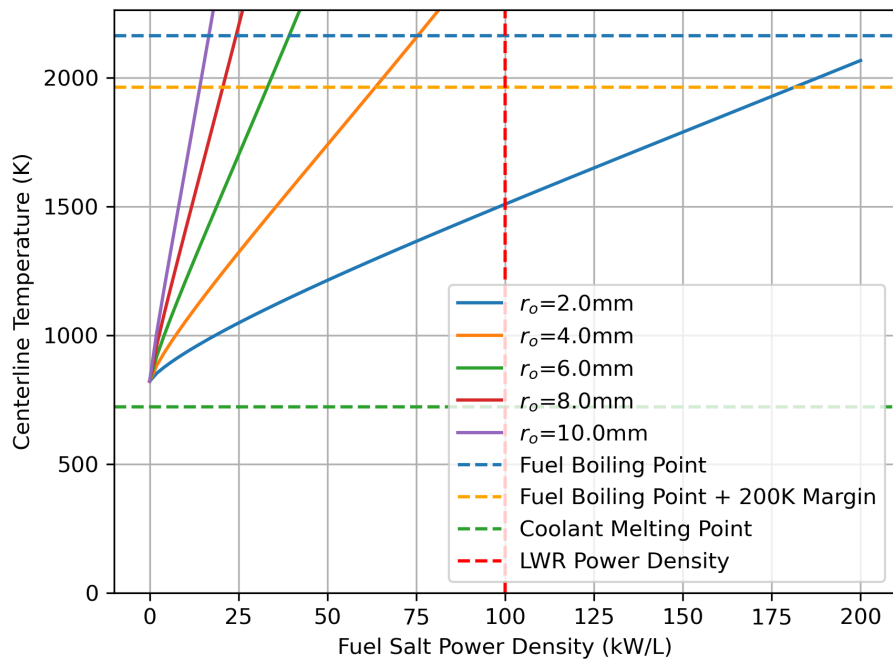


Figure 37: The centerline temperatures calculated using the finalized coolant and fuel salts

clad temperature while maintaining the centerline temperature below the boiling margin and allowing for a power density comparable to a LWR. To accurately model these effects, however, it is necessary to resort to computational fluid dynamics (CFD).

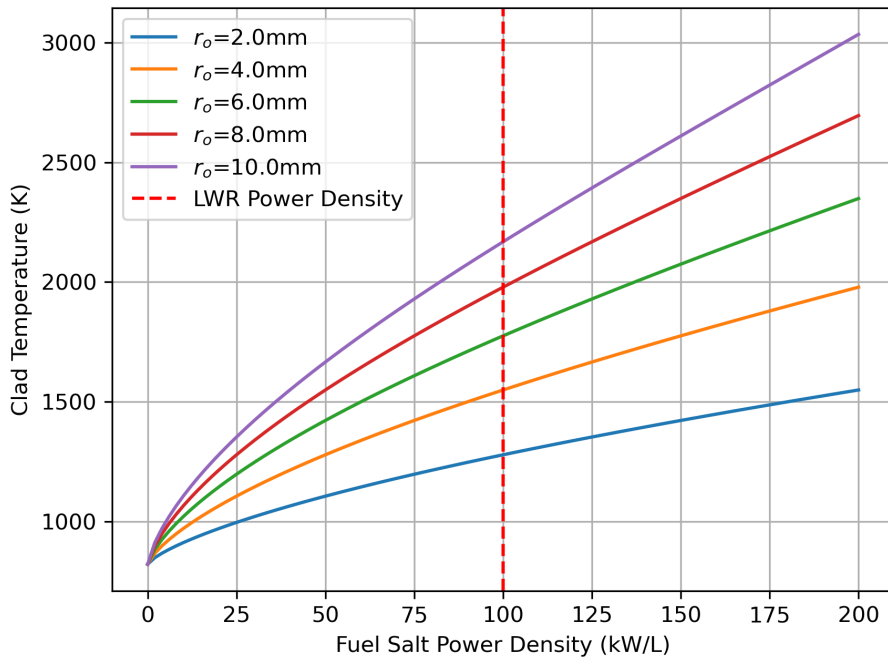


Figure 38: The clad temperatures calculated using the finalized coolant and fuel salts

## 8.1 CFD Methodology

There are a plethora of CFD codes available for general engineering use of which the following were considered

1. Ansys Fluent
2. NEK 5000/NEK RS
3. OpenFOAM [2]

Ansys is industry standard for nuclear engineering, and provided a user friendly UI, but as a commercial code, obtaining access was judged to be too difficult. NEK 5000/NEK RS is a modern CFD tool that claims to outperform standard CFD solvers and contains algorithms that scale very well on HPC platforms, but at least compared to OpenFOAM, it's not very well documented. For these reasons, OpenFOAM was chosen for this project.

### 8.1.1 Goals

As described, current scoping calculations do not support the use of a larger fuel tube radius ( $r_o = 5.5\text{ mm}$ ) or a power density of  $100\text{ kW/L}$  (really the minimum required for the concept to be competitive with LWRs) due to the elevated clad temperature. In addition, a smaller pitch to fuel tube diameter is required for neutronic feasibility, which further constrains the thermal hydraulics. The goal of these calculations is to show that with a pitch to tube diameter ratio of 1.35, a power density of  $100\text{ kW/L}$ , and a tube diameter of 11 mm

1. The clad temperature is below the code for stainless steel 316H (otherwise advanced materials such as SiC or ceramic refractory materials would have to be considered)
2. The fuel salt is sufficiently below its boiling point

### 8.1.2 Modelling Approach

To accurately represent the hexagonal lattice of fuel tubes and simplify the problem specification in OpenFOAM, the calculation was split into two steps

1. Calculate the coolant temperature distribution in a hexagonal pincell with symmetric boundary conditions given a fixed heat flux (calculated from the given power density). Note in this calculation, *only the coolant exists*, and the clad is assumed to have negligible thermal resistance.
2. Calculate the the fuel temperature using the clad temperature calculated from the coolant simulation as a boundary condition and including a volumetric source of 100 kW/L. Note in this calculation *only the fuel salt exists*.

Dividing the calculation in this way avoids the need for a multiregion solver, which is difficult to set up and often difficult to converge. For both simulations, the `buoyantSimpleFoam` solver was used, which models compressible steady state buoyancy driven flow. The finite volume schemes used to discretize the governing equations are difficult to synthesize, and so were primarily based on those used in similar calculations available on [GitHub](#).

#### 8.1.2.1 CFDOF

Although OpenFOAM is very general, mesh generation using the built-in mesh generator `blockMesh` is *very* difficult, requiring the user to *manually* define each of the vertices of the geometry. To aid in mesh generation and case set up, an open source extension for the FreeCAD workbench: `CFDOF` was used. CFDOF allowed generating the meshes for both cases using a classic CAD GUI, and the resultant meshes (as well as the FreeCAD workspace) are shown in Fig. 39.

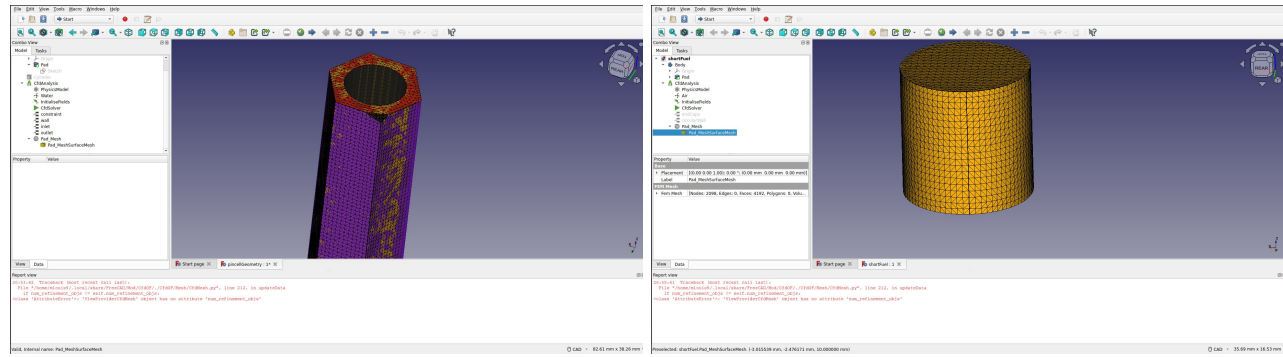


Figure 39: CFD meshes

Note that, for each calculation, the thermophysical properties of the coolant and fuel had to be manually specified in the case setup. The complete case setups for the coolant and fuel calculations are found [here](#) and [here](#), respectively.

## 8.2 The Coolant Calculation

### 8.2.1 Boundary Conditions

The heat flux is used as a boundary condition in OpenFOAM, and can be calculated from the given pin geometry and the core power density

$$d_{pin} = 11.0 \text{ mm} \quad (\text{Pincell diameter})$$

$$h = 3.0 \text{ m} \quad (\text{Active core height})$$

$$R_{pincell} = 8.73 \text{ mm} \quad (\text{Circumradius of hexagonal pincell}) \quad q''' = 1 \times 10^2 \frac{\text{kW}}{\text{l}} \quad (\text{Volumetric power density})$$

$$t_{clad} = 0.6 \text{ mm} \quad (\text{Clad thickness})$$

$$r_{pin} = \frac{\sqrt{3}}{2} \cdot R_{pin} = \frac{\sqrt{3}}{2} \cdot 8.73 \text{ mm} = 7.56 \text{ mm} \quad (\text{Pin cell inradius - the lattice pitch})$$

$$A_{fuel} = \pi \cdot \left( \frac{d_{pin}}{2} - t_{clad} \right)^2 = 3.142 \cdot \left( \frac{11.0 \text{ mm}}{2} - 0.6 \text{ mm} \right)^2 = 75.4 \text{ mm}^2 \quad (\text{Fuel cross sectional area})$$

$$\begin{aligned} A_{subchannel} &= 2 \cdot \sqrt{3} \cdot (r_{pin})^2 - \pi \cdot \left( \frac{d_{pin}}{2} \right)^2 \\ &= 2 \cdot \sqrt{3} \cdot (7.56 \text{ mm})^2 - 3.142 \cdot \left( \frac{11.0 \text{ mm}}{2} \right)^2 \\ &= 1.03 \times 10^2 \text{ mm}^2 \quad (\text{Coolant cross sectional area}) \end{aligned}$$

$$q = A_{fuel} \cdot h \cdot q'' = 75.4 \text{ mm}^2 \cdot 3.0 \text{ m} \cdot 1 \times 10^2 \frac{\text{kW}}{1} = 22.6 \text{ kW} \quad (\text{Power per rod})$$

$$SA_{pin} = 2 \cdot \pi \cdot \left( \frac{d_{pin}}{2} \right) \cdot h = 2 \cdot 3.142 \cdot \left( \frac{11.0 \text{ mm}}{2} \right) \cdot 3.0 \text{ m} = 0.104 \text{ m}^2 \quad (\text{Heated surface area of fuel pin})$$

$$q'' = \left( \frac{q}{SA_{pin}} \right) = \left( \frac{22.6 \text{ kW}}{0.104 \text{ m}^2} \right) = \boxed{2.18 \times 10^5 \frac{\text{W}}{\text{m}^2}}$$

This is the boundary condition that was imposed on the inner boundary in the OpenFOAM case setup. Also, it was assumed that the coolant inlet velocity was uniformly  $U_z = 1 \text{ m/s}$  and at a somewhat conservative temperature of 800 K (around 70 K above the coolant salt melting point).

Due to the large computational domain (3 meters long) and the relatively fine mesh, for the calculation to complete in a reasonable amount of time, HPC resources were necessary. Calculations were performed using resources available through Idaho National Lab's Nuclear Computational Resource Center (NCRC) [3]. The simulation was decomposed into 480 domains each run using 1 CPU on the Sawtooth cluster.

### 8.2.2 The Profiles

The qualitative velocity and temperature profiles are shown in Fig. 40, and show qualitatively the no slip boundary conditions imposed on the velocity field at the clad surface, and the symmetry condition on the hexagonal pin cell that causes the velocity to peak near the vertices of the pin cell. Likewise, it is seen that the thermal boundary layer is on the order of millimeters, and the temperature quickly rises to around 950 K at the clad surface near the top of the pin cell. Though not visible in this view, the inlet boundary conditions can be visually seen to be satisfied well by the results. All of the above, along with the adequately small residuals (set to less than  $10^{-6}$  for each field) imply that these calculations are well converged and physically reasonable. Although it would be preferable to first benchmark the calculation, due to time constraints this was not possible.

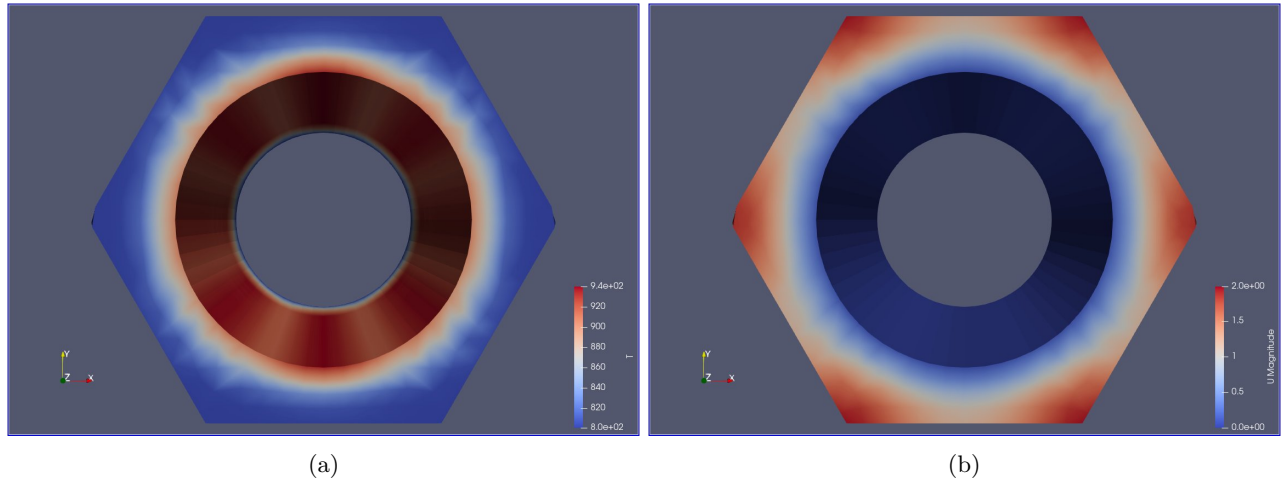


Figure 40: Coolant velocity (magnitude) and temperature profiles

### 8.2.3 Radially Averaged Fields

Though the 3D field profiles are visually appealing, they aren't very quantitatively insightful. To distill some of the field information, radial averages of each of the fields were computed for each  $z$  level, and plotted in Fig. 41. We see that the average  $z$ -velocity is nearly constant over the whole length of the pin-cell, and roughly equal to its inlet value. This is interesting, because we might expect the average velocity to increase due to the buoyant acceleration caused by the heating of the coolant, however it's possible this effect is negated by the viscous friction imposed by the no-slip boundary conditions. A more troubling result is the pressure profile shown in Fig. 41 (c), which shows that the inlet pressure must be nearly 50 MPa (while the outlet value was set to atmospheric pressure). The inlet pressure was set to be a calculated boundary condition, i.e. the pressure field on the boundary is calculated from the simulation to be consistent with each of the other fields and the conditions on the other boundaries. This extremely large inlet pressure could be the result of an incorrect case setup, or perhaps is truly indicative of the *large* pumping requirements to move the relatively dense coolant salt through the core. Finally, we can see that the radially averaged temperature increases

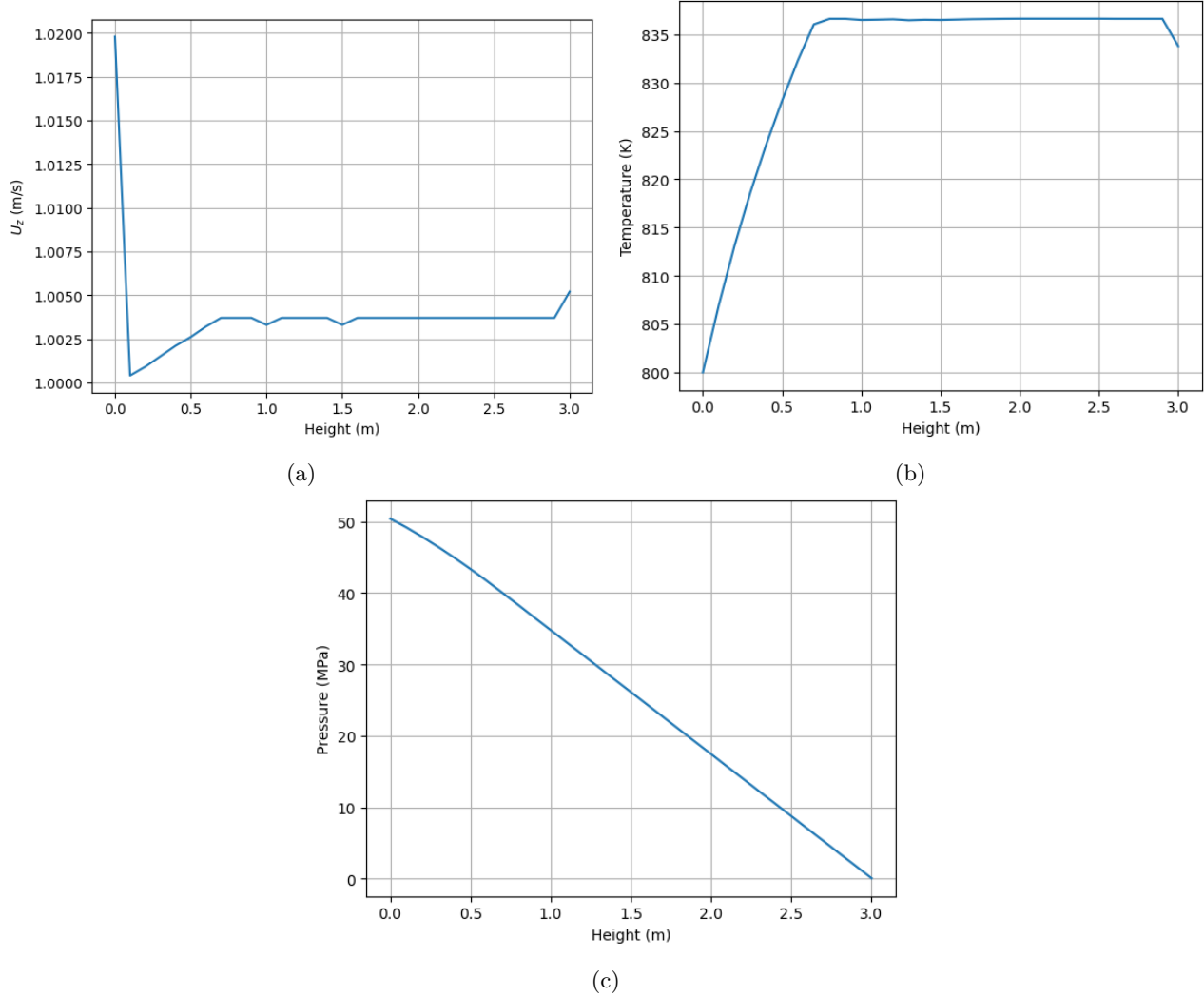


Figure 41: Radially averaged fields for the coolant calculation

#### 8.2.4 Clad Surface Averaged Fields

Finally, the fields were averaged along the perimeter of the inner (clad) surface for each  $z$  level in paraview to generate the results in Fig. 42. The same large inlet pressure is observed along the clad inner surface as well, and the pressure profile in general did not vary radially (and so it was not displayed in Fig. 40), so this result is to be expected. We see that the coolant  $z$  velocity tends to 1 m/s at the inlet (as required by the boundary condition) but the  $z$  velocity is *not* exactly zero on the clad inner surface as it should be for a no slip condition. This is in conflict with the velocity profile shown in Fig. 40 which seems to suggest that it *is* exactly zero, which might imply that this averaging/postprocessing in paraview was imperfect. We see that the maximum clad temperature is less than 930 K, which is sufficiently below the code for stainless steel 316H (as described in Section 5) and so verifies the thermal hydraulic feasibility of the design for the clad, and so it remains only to show that the fuel temperature is within a reasonable margin of its boiling point. These clad averaged fields were then used as boundary conditions for the fuel salt calculation in the next section. Note that this is an approximation - because the pin cell is non-circular, the temperature of the clad will be lower at positions near the vertices (where there is a greater amount of coolant separating adjacent rods on average), and this nonuniform temperature profile can be visually seen in Fig. 40 (a), but for the sake of input simplicity, the averaged values were used to impose a axisymmetric axial temperature

distribution for the fuel calculation.

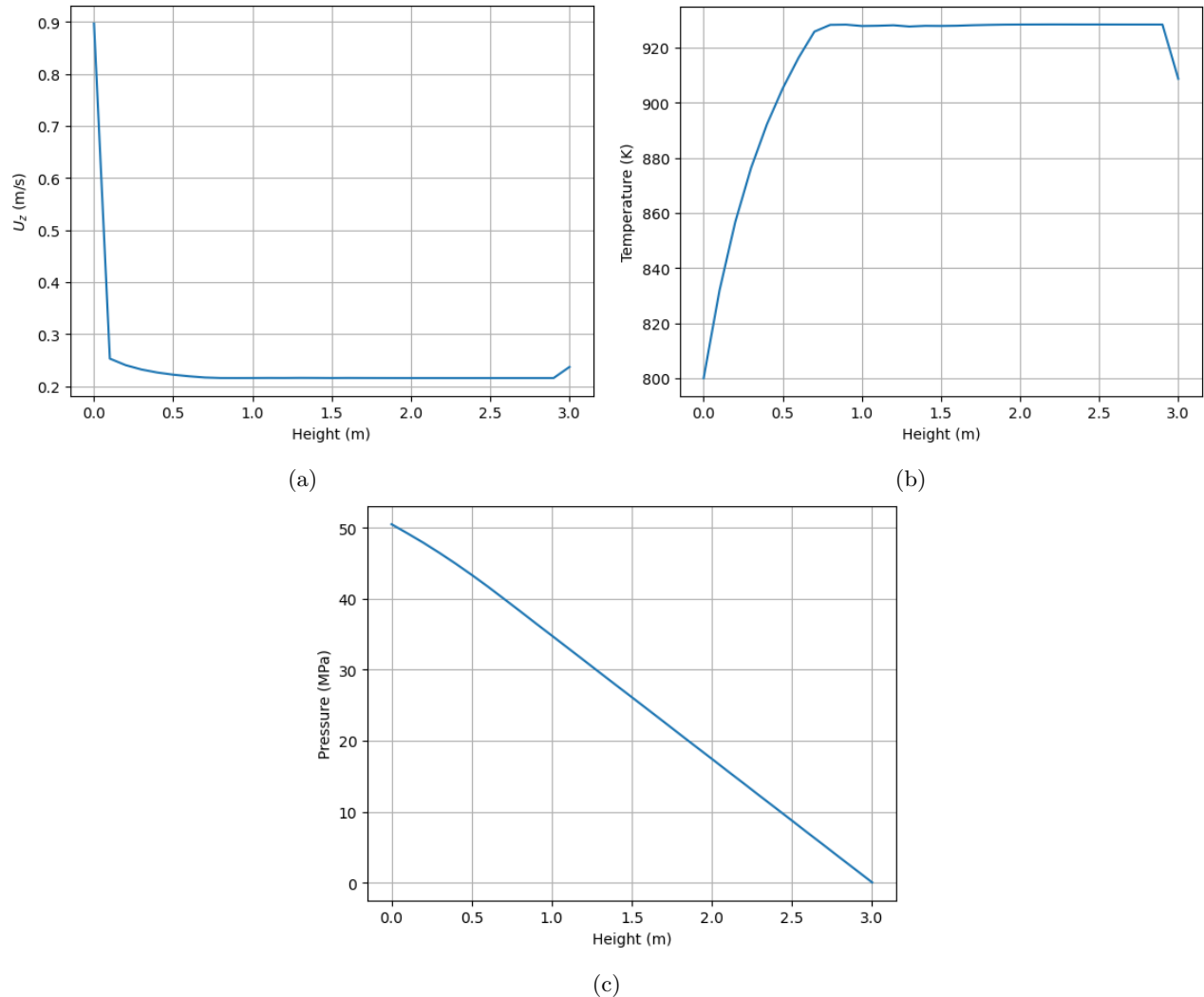


Figure 42: Clad surface averaged fields for the coolant calculation

### 8.3 The Fuel Calculation

To model the fuel salt which is generating heat uniformly at 100 kW/L, a source term must be added into the governing equations solved by OpenFOAM. Practically, this was done by adding a fission heat source to the finite volume options

```
fissionHeatSource
{
    // Type of source, using scalarSemiImplicitSource for energy equation
    type      scalarSemiImplicitSource;

    // Apply to entire domain
    selectionMode all;

    // Specify as absolute source (W/m^3)
    volumeMode specific;

    // Specify the field affected, here it's the enthalpy field
    injectionRateSuSp
    {
        h          (100000000 0); // 100,000,000 W/m^3 explicit, 0 implicit
    }
}
```

in addition, no slip boundary conditions were added to all boundaries because the fuel salt is practically constrained inside of the fuel tube (although there is venting of fission product gases into the coolant), and adiabatic thermal boundary conditions were also added to the top and bottom of the pincell. Finally, the polynomial coefficients representing the thermophysical properties given in Fig. 30 were used in the input.

#### 8.3.1 Approximating With a Shortened Pincell

The first thing to note is that the mesh shown in Fig. 39 (b) is much shorter than the 3 m rod length, and is in fact only 10 mm in length. Simulating the entire rod length was attempted but convergence issues prevented any meaningful results, which was interestingly *not* the case for the shortened model. Different mesh refinements and finite volume schemes were tried to improve the convergence of the full length simulation, but pinpointing issues in OpenFOAM can be very difficult in a large case such as this. It was assumed that a shortened pincell with the same axial temperature profile imposed on it (i.e. 800 K at the bottom and around 930 K near the top) would have nearly the same temperature profile. The only difference between the two cases is that, in the full length simulation, there is a larger space within the fuel tube for free convection flow patterns to develop, and since the upper and lower boundaries are further apart, less viscous friction, allowing for more heat transfer. So, the results given below are though to represent a conservative estimate.

#### 8.3.2 The Profiles

The temperature and velocity profiles along different slices are shown in Fig. 43 and show:

1. (although it's admittedly hard to see) the satisfaction of the imposed axial temperature profile on the boundary
2. The development of a free convection pattern in the fuel tube where the  $z$  velocity is negative on the clad surface where the fuel salt is cooled, increases its density, and sinks to the center where it is heated, its density decreases, and it is accelerated by buoyant forces and has a large *positive*  $z$  velocity.
3. The largest fuel salt temperature occurs at the top and center of the pincell, as expected
4. The no slip condition is satisfied on all surfaces

the above suggest, along with the reasonably low residuals, that the case was set up correctly, and the simulation is physically accurate.

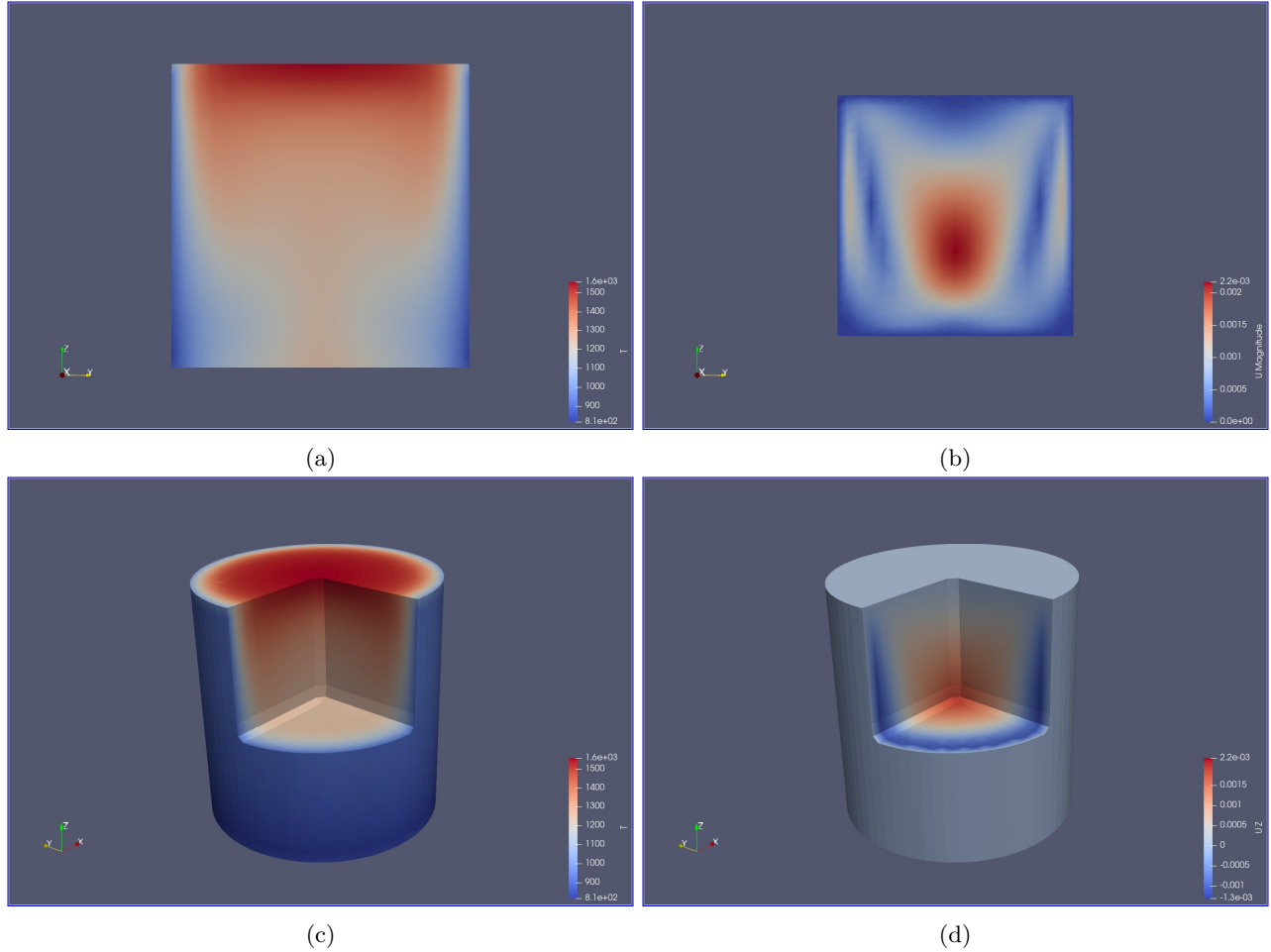


Figure 43: Fuel velocity (magnitude) and temperature profiles

### 8.3.3 Radially Averaged Fields

As for the coolant case, more quantitatively insightful information can be obtained by radially averaging the fields, as was done in Fig. 44. We see that the average  $z$  velocity is *negative* and very small in magnitude, as is roughly corroborated by Fig. 43 (b), however it is practically zero, as we might expect since the fuel salt is completely enclosed (if there were a nonzero net velocity there would not be conservation of mass). The average temperature is around 1000 K, which is *much* lower than the boiling point, as desired, but it still remains to show that the centerline temperature is below the boiling point. The pressure in the case is *negative*, which might be concerning initially, but OpenFOAM simulations only output *gauge pressure*, so these values are perfectly physical, and we see that they are on the order of Pa, and so essentially zero. Interestingly, each of these radial averages is nearly constant with height.

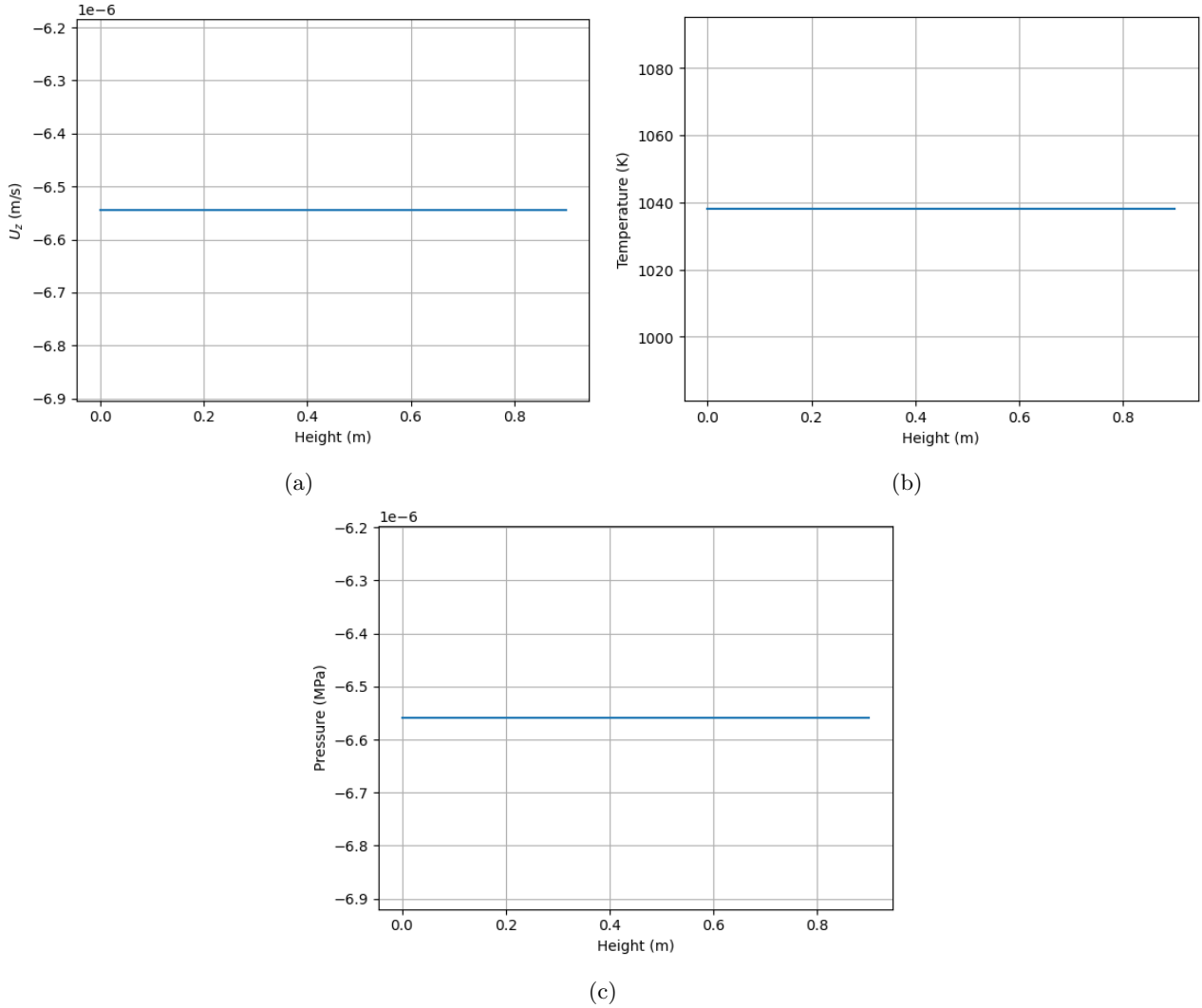


Figure 44: Radially averaged fields for the fuel calculation

### 8.3.4 Fields Along the Centerline

Finally, the fields along the centerline were extracted using paraview, and are shown in Fig. 45. These show the positive  $z$  velocity along the centerline (where temperatures are the highest radially) that drives the free convection flow pattern discussed previously. Most importantly, we see that the max centerline temperature (which indeed occurs at the top of the pin cell) is 1550 K, well within the 270 K margin of the boiling point, as recommended by Section 5.

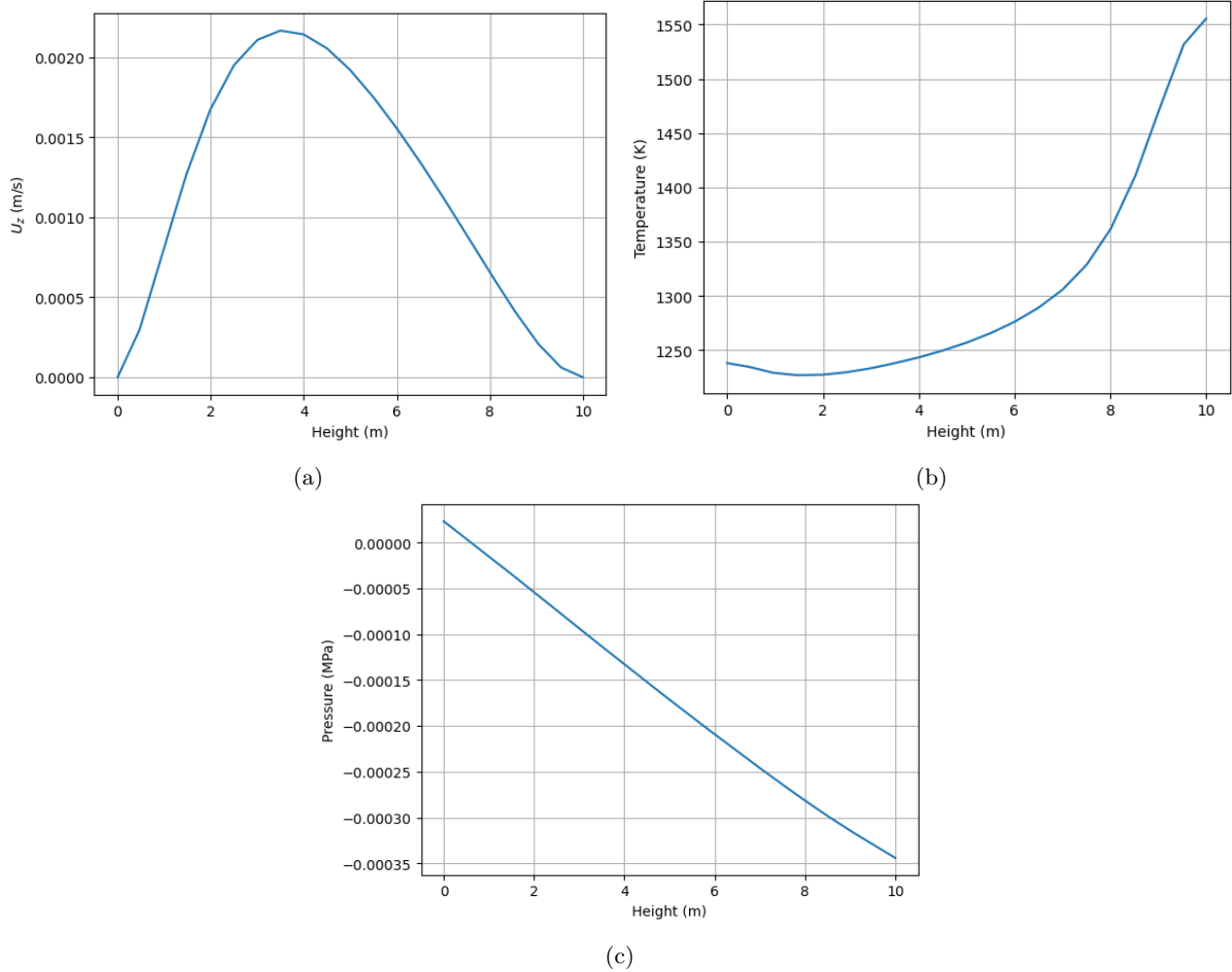


Figure 45: Fields along the fuel centerline

## 8.4 A Worst Case Analysis

The above results were for the average pincell, however, the power distribution in a practical core will not be flat, and in the worst case (in a completely fresh core) the power peaking can be quite high, causing some fuel tubes to generate much more heat. These pins are the most thermohydraulically constraining for a practical core, and to say that our design is thermohydraulically sound, the results above should really be extended to the hottest fuel tube. For a completely fresh core (homogeneous), we may use diffusion theory to approximate the power peaking. For a finite cylinder, the flux is given by

$$\phi(r, z) = AJ_0\left(\frac{2.405r}{R}\right) \cos\left(\frac{\pi z}{H}\right)$$

And the minimum to average flux ratio is

$$\frac{\phi_{max}}{\phi_{av}} \equiv \Omega = 3.64$$

so we can approximate that the central fuel element will produce 3.64 times the average pin power, or

$$P_{pin,max} = 3.64 \cdot q = 3.64 \cdot 22.6 \text{ kW} = 82.4 \text{ kW}$$

as opposed to 22.6 kW for the average fuel tube. Note that this is really only at the very center, not along the entire central axis, although it's a useful conservative assumption. Unfortunately, due to time constraints this case could not be analyzed, so it remains for future work.

## 8.5 The Need for Pumps

Though the results seem promising for proving the claim made by Scott in [1], a more thorough analysis of the pressure drops throughout the primary loop (including in the heat exchanger) would be needed to confidently make this claim, so for now, it will be assumed that conventional pumps will be used in the primary loop. As described by Scott, if natural convection could be relied on *solely*, then the development issues regarding the development of reliable pumps for molten salt reactors could be sidestepped entirely, which is an attractive benefit, but remains to be shown.

## 8.6 Decay Heat

The decay heat (immediately following shutdown) calculated in the Neutronic analysis:  $2.5 \text{ MW}_t$ , is a *very* small fraction of the total thermal power ( $426 \text{ Mw}_t$ ), and it is thought that natural convection in each of the primary and secondary loops, along with convective and radiative heat transfer from the vessel would be sufficient to *completely* remove the decay heat (this claim is also made by Scott in [1]), although the calculations required to justify this were both outside of the time and technical constraints of this project.

## 8.7 Efficiency

For a light water reactor with an outlet temperature of  $\approx 588 \text{ K}$ , and a cold reservoir temperature of around  $300.15 \text{ K}$ , a typical thermal efficiency is 33%. The Carnot efficiency for a system operating between those two temperatures is

$$\begin{aligned}\eta_1 &= 1 - \frac{300.15}{588} \\ &= 0.4898\end{aligned}$$

which implies that the ratio of the actual efficiency to the Carnot efficiency ( $\epsilon$ ) is

$$\begin{aligned}\epsilon &= \frac{0.33}{0.4898} \\ &= 0.67\end{aligned}$$

assuming this same value for our secondary loop, we can estimate an efficiency of

$$\begin{aligned}\eta &= 0.67 \left( 1 - \frac{300.15}{835} \right) \\ &= \boxed{0.43}\end{aligned}$$

which represents a 30% increase in efficiency due to purely to the higher temperatures allowed by a molten salt coolant.

## 8.8 Conclusion

Using modern CFD tools, the chosen power density, fuel tube radius, and lattice pitch were justified from a thermohydraulic standpoint (at least on average) that is they allow for clad temperatures below the code for stainless steel 316H, and fuel temperatures comfortably below the boiling point. These calculations represent the knowledge gap at the time of the Aircraft Reactor Experiment (ARE) and the conclusions we are able to draw with them now are a testament to the power of modern CFD tools and scientific computing as a whole.

## References

- [1] Thomas James Dolan. *Molten salt reactors and thorium energy*. Woodhead Publishing, 2017.
- [2] Hrvoje Jasak, Aleksandar Jemcov, Zeljko Tukovic, et al. Openfoam: A c++ library for complex physics simulations. In *International workshop on coupled methods in numerical dynamics*, volume 1000, pages 1–20, 2007.
- [3] Robert K Podgorney. Nuclear computational resource center-status and fy21 plans. Technical report, Idaho National Lab.(INL), Idaho Falls, ID (United States), 2020.

## 9 Safety

### 9.1 Event Trees

The safety assessment can be illustrated through the event tree analysis (ETA) which is a useful schematic for visualizing failures and their consequences in a nuclear accident scenario [2, 3]. The fundamental purpose of ETA is mitigation of the consequences, whereas other analysis may focus on prevention of the causes, such as Fault Tree Analysis [1]. The trees model the possibility of high-risk consequences of a system failure as well as reliability. They are headed by “Initiating Events” (IE) which are any potential occurrence that could disrupt plant operations. Examples of such initiating events could be a loss of coolant or loss of power. In the design phase, these events are also referred to as “Postulated Initiating Events” (PIEs) but in our analysis, we have elected to just call them Initiating events for simplicity. Typically, these events are quantified in terms of their frequency (specifically the probability or number of events per year). However, for our analysis, the tree will be qualitative since there is no yearly data recorded for our proposed design as it’s conceptual and estimating them is outside the scope of this project. Following the initiating event, each of the dividing branches represents the possible successive events which demonstrate the success or failure of the safety functions. The upward branches signify the successes whereas the downward branches signify the failures at each stage. In typical trees, the actions taken to mitigate the severity of the consequences as well as the effectiveness of these actions are also recorded. The branches expand until they reach the end state or “Result” of the reactor, which would show the several outcomes pertaining to the accident. The level of severity of the outcomes typically scales in impact from least to greatest going from the top of the display to the bottom.

In summary, the main purpose of the Event Tree analysis is to assist with reactor safety by:

1. Identifying and understanding the possible sequences of events that could lead to common and severe accidents
2. Assessing the probability of each sequence of events occurring
3. Evaluating the potential consequences of each event
4. Identifying vulnerabilities and weaknesses within the safety systems
5. Facilitating the safety measures and emergency response plans

### 9.2 Accidents

There are three main sub-categorizations for internally provoked accidents pertaining basic Design Basis Accidents (DBAs) to molten salt reactors and they are:

1. Power Excursion accident
2. Flow Decrease accident
3. Fuel Salt leak accident

### 9.2.1 Power Excursion Accident

This accident is also known as a Reactivity Initiated Accident (RIA) and it primarily occurs due to control rod withdrawal or ejection provoked by operator oversight error or equipment failure. If the neutron-absorbing control rod is removed, then the system's moderation decreases, triggering the response. The negative reactivity coefficient within the fuel should be sufficient to mitigate and terminate the power excursion, even in the event of a SCRAM failure.

### 9.2.2 Flow Decrease Accident

This accident pertains to the event in which the pumps fail, and the heat removal function is diminished. In this case, there would be an increase in the fuel salt temperature and the quantity of the delayed neutrons in the core. This would eventually cause the core to overheat and the cladding and structural materials to fail. However, this accident should be tremendously mitigated by the SCRAM function and the negative reactivity coefficient. There would still be an amount of decay heat to remove by passive cooling functions.

### 9.2.3 Fuel Salt Leak Accident

These accidents are caused by compromises in the integrity of the vessel, pipes, or heat exchangers which can allow leakages of the fuel salt. They can be caused by corrosion, manufacturing faults, high temperatures, or natural disaster. The primary safety system to control and mitigate the effects of a leak is shutting down the core as soon as feasible. However, these fuel salt leaks should be benign because the fuel salt would mix with the coolant and be effectively diluted, and the two substances are chemically compatible [5, 4].

## 9.3 Severe Accidents

A severe accident is one that challenges the safety functions to a much higher degree than expected. These accidents pertain to the series of events that can result in significant core damage or release of radioactive material to the surrounding environment. In the following section, event trees have been constructed for a selection of severe accidents to illuminate the response that could mitigate the negative consequences. Specifically, these show the action plan as well as consequences corresponding to potential scenarios for a criticality event, source term accident, decay heat accident, and a Loss of Coolant (LOCA) event. The LOCA event has been included because it is the accident scenario of most concern in our design. This would be a positive reactivity insertion, which would cause the reactor to go supercritical without sufficient coolant. This would ultimately result in melting conditions.

### 9.3.1 Criticality Event

These events occur from excess reactivity due to changes in the temperature, geometry, and/or composition of the system while operating. Particularly, a control rod ejection accident occurs when a control rod is withdrawn during operation, leading to a RIA, the effects of which are shown in Fig. 46.

## Criticality Event

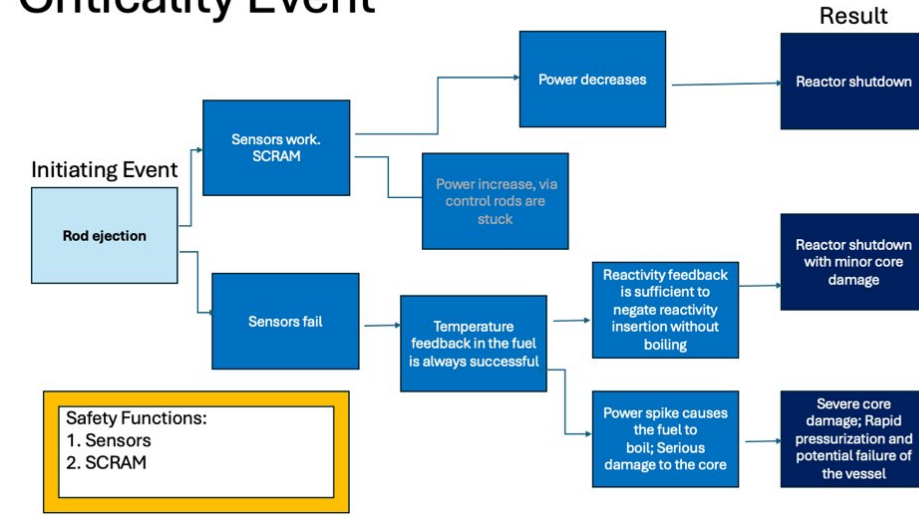


Figure 46: Event tree for a criticality/reactivity insertion accident

### 9.3.2 Source Term Accident

The source term is the measure of the radiation from the fuel which needs to be contained from reaching any of the sensitive locations. Source term-related accidents can include heat removal failure or changes to the system structure's integrity. The mechanisms used to reduce the source term and ultimately alleviate the severity of these accidents can be reducing dispersion driving force, eliminating major stored energy sources, and reducing the long half-life isotopes. An even tree showing the progression of a source term accident is shown in Fig. 47

## Source Term

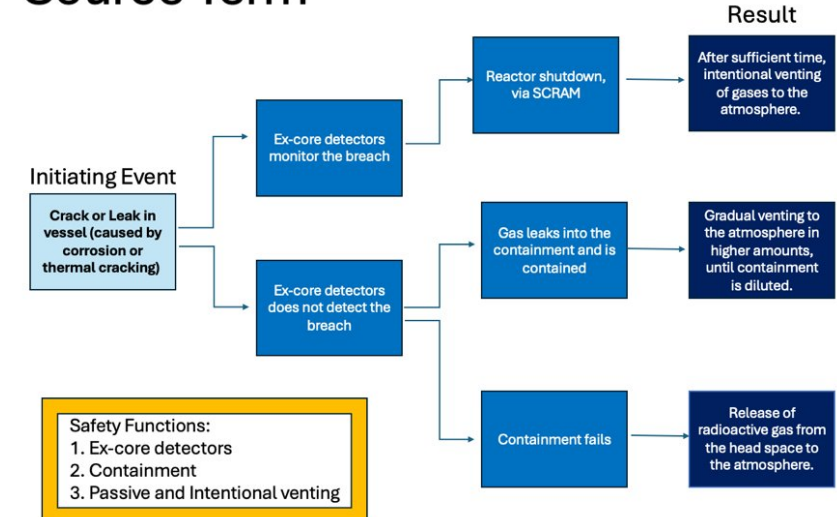


Figure 47: Event tree for a source term accident

Note: We hope that in the worst-case scenario that the source term would still be relatively small because the primary gases in the headspace are Xenon and Krypton

### 9.3.3 Decay Heat Accident

Decay heat accidents can result from inability to remove heat from the fuel after the nuclear chain reactions have been stopped via the reactor being shut down. When this happens, if cooling is not reintroduced, temperatures rise until structural materials fail, releasing fission products and radiation (as is depicted in Fig. 48). In our design, most of the gaseous fission products are radioactive isotopes of Xenon and Krypton inside the fuel head. A related accident, for which large temperature excess also leads core damage is a loss of coolant accident, for which an event tree is shown in Fig. 49.

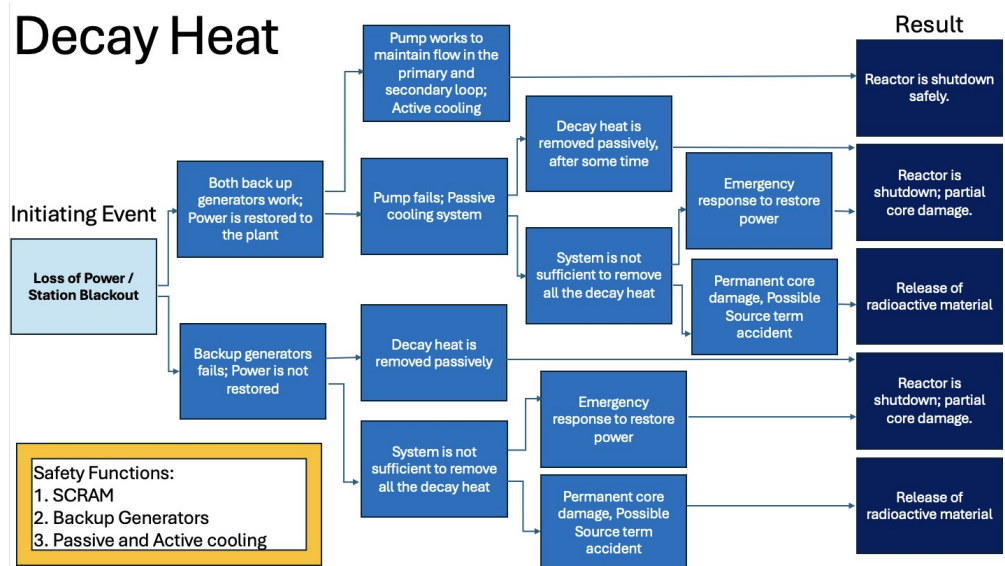


Figure 48: Event tree for a decay heat accident

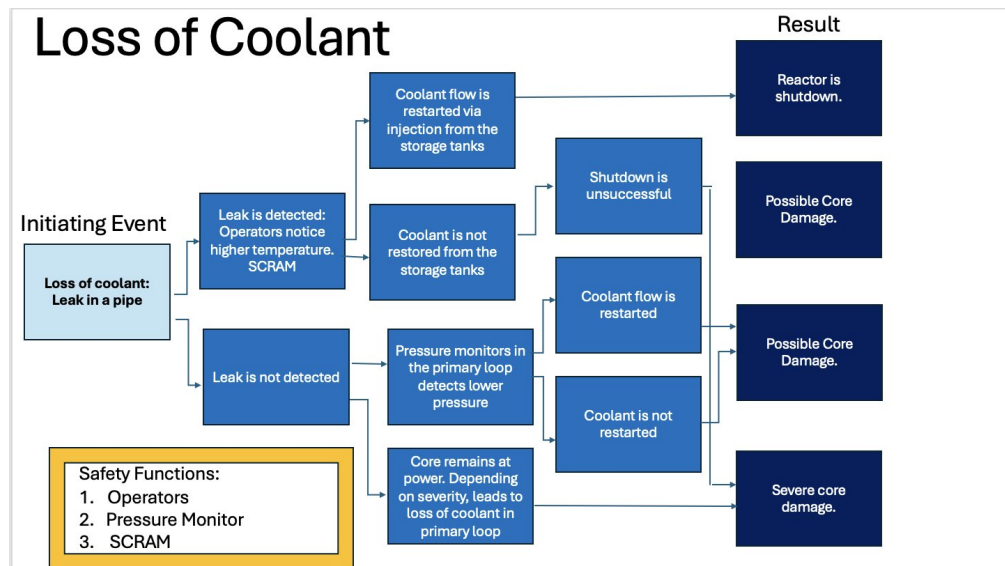


Figure 49: Event tree for a loss of coolant accident

## 9.4 Safety Functions

Our primary safety function and response in the event of a crisis is the alarm system and immediate implementation of the control rods via the SCRAM function (historically known as Security Control Rod Axel Man). Due to the nature of the electromagnetic mechanism in which the rods are suspended and physical properties of the earth, gravity, once SCRAM is initiated, the rods must be released. Aside from this, other safety functions which may be subject to fault include operator oversight, system monitors, detectors, physical structure, passive and active cooling systems, and the backup generators. In our design there is redundancy in these functions, like in the AP 1000, to decrease the detriment in the event of failure. For example, there would be multiple backup generators, detectors, monitors, and operators to maintain the systems. Passive cooling of the system would be implemented through the natural circulation of air over the reactor vessel and in the primary and secondary loop. Other important safety functions are the fans and cladding of the fuel rods. The purpose of the fans would be in an event where active cooling of the temperature is needed in supplement to the inherent passive cooling system. The cladding provides additional moderation which keeps the fission productions from escaping into the environment. To combat a LOCA event, it is our plan to have supplemental coolant tanks appropriately heated in storage to diminish the time spent to recover the coolant in the core.

### 9.4.1 A Note on Freeze Plugs

Due to the infeasibility, our design does not include freeze plugs which are a nominal shutdown feature for typical molten salt reactors. Their absence is abated because our design implements more control rods than in other standard molten salt reactors. Furthermore, our design is more resemblant to a light water reactor, which control rods are sufficient for licensing purposes from the NRC.

## References

- [1] Iman Q Al Saffar and Akram W Ezzat. Probabilistic risk assessment of typical process plant using event tree and fault tree analysis. *J Mech Eng Res Develop*, 43:465–477, 2020.
- [2] Felix Ameyaw, Rex Abrefah, S. Yamoah, and Sylvester Birikorang. Analysis and estimation of core damage frequency of flow blockage and loss of coolant accident: A case study of a 10 mw water-water research reactor-psa level 1. *Science and Technology of Nuclear Installations*, 2021:1–17, 06 2021.
- [3] Matteo D’Onorio, Tommaso Glingler, Fabio Giannetti, and Gianfranco Caruso. Dynamic event tree analysis as a tool for risk assessment in nuclear fusion plants using raven and melcor. *IEEE Transactions on Plasma Science*, 50(11):4514–4520, 2022.
- [4] Badawy M. Elsheikh. Safety assessment of molten salt reactors in comparison with light water reactors. *Journal of Radiation Research and Applied Sciences*, 6(2):63–70, 2013.
- [5] Ritsuo Yoshioka and Motoyasu Kinoshita. *Liquid fuel, thermal neutron spectrum reactors*, pages 281–373. 12 2017.

## 10 Regulations

The relevant regulations for radioactive gases and radioactivity in the coolant in the United States are primarily governed by the Nuclear Regulatory Commission (NRC) and the Environmental Protection Agency (EPA) with the goal of ensuring that any potential releases do not impose detrimental risk to public health and the sanctity of the environment. For management of radioactivity in the coolant, the regulations are set by the NRC with the same overarching goal of fostering the safe operations of facilities and the protection of public health and the environment.

For our design the regulations more crucial to pay attention to are those concerning:

1. Venting of Radioactive gases
2. Radioactivity in the coolant

## 10.1 Venting of Radioactive Gases

Pertaining to the venting of radioactive gases, pertinent standards come from the Code of Federal Regulations (CFR) in PART 190.10— Standards for normal operations. These standards are firstly that “the annual dose equivalent does not exceed 25 millirems to the whole body, 75 millirems to the thyroid, and 25 millirems to any other organ of any member of the public...” and secondly that “the total quantity of radioactive materials entering the general environment . . . contains less than 50,000 curies of krypton-85, 5 millicuries of iodine-129, and 0.5 millicuries combined of plutonium-239 and other alpha-emitting transuranic radionuclides with half-lives greater than one year.” [1].

Other standards that must be adhered to are from the 40 CFR 61.92 which is: “Emissions of radionuclides to the ambient air from Department of Energy facilities shall not exceed those amounts that would cause any member of the public to receive in any year an effective dose equivalent of 10 mrem/yr.” [3].

## 10.2 Radioactivity in the Coolant

Likewise, for the radioactivity in the coolant, the NRC specifies within the 10 CFR 50.36a that the release of radioactive materials, including the coolant, or radiation pertaining to it should be as low as reasonably achievable in compliance with the provisions in 10 CFR Part 20.1301, which refers to the dose limits for individual members of the public as a basis for the standard [7, 2].

## 10.3 Dosimetry

In general, the regulations regarding occupational dose limits are from the NRC or the EPA as displayed here in this chart and found in the 10 CFR (code of federal regulations) [8, 5, 6]

Occupational Dose			
	NRE 10 CFR 10	EPA 52 FR 2822	OSH 29 CFR 1910.1096
Whole Body	5000	5000	5000
Lens of Eye	1500	15000	5000
Skin, Hands, Feet	50000	50000	N/A

Non-Occupational Dose			
General Public	100 mrem in 1 year	N/A	N/A
Non-Occupational Dose (Uncontrolled Areas)			
General Public	2 mrem in 1 hour	N/A	N/A

Table 18: Regulations for occupational and non-occupational dose

## 10.4 Other Basic Characteristics for MSR Safety pertaining to Our Design

Other basic safety characteristics are as described below [4]:

1. The primary and secondary systems have pressures lower than 5 bars, therefore there is no danger of accidents due to high pressure which could cause system destruction or salt leakage.
2. The fuel and coolant salts are chemically inert, so therefore they would not ignite if exposed to the air.
3. The boiling point of the fuel salt is about 1670K or much more, so long that it is much higher than the operation temperature 973 K. Therefore, the pressure of primary system cannot increase causing system destruction or damage.
4. The fuel rods on their own are subcritical, only when exposed to a full core geometry will the neutron economy be such that its critical.

5. Molten salt reactors have a large negative temperature coefficient of the fuel salt which is much larger than the temperature coefficient of the coolant, which is slightly positive.
6. The delayed-neutron fraction in  $^{233}\text{U}$  fission is smaller than that in  $^{235}\text{U}$ , and half of the delayed neutrons is generated outside the core. However, it is within the controllable range and due to the longer neutron life, and large negative prompt temperature coefficient of fuel salt.
7. The excess reactivity and required control rod reactivity are sufficiently small, and the reactivity shift by control rods is small.
8. Gaseous fission products such as Kr, Xe and T are continuously removed from the fuel salt, so that the buildup is minimized.

## References

- [1] Federal Register :: Request Access — ecfr.gov. <https://www.ecfr.gov/current/title-40/chapter-I/subchapter-F/part-190>. [Accessed 20-04-2024].
- [2] US Nuclear Regulatory Commission et al. Subpart d—radiation dose limits for individual members of the public. *nrc.gov*, 1991.
- [3] National Research Council et al. Environmental protection agency guidances and regulations for naturally occurring radionuclides. *Evaluation of Guidelines for Exposures to Technologically Enhanced Naturally Occurring Radioactive Materials*, 1999.
- [4] Badawy M. Elsheikh. Safety assessment of molten salt reactors in comparison with light water reactors. *Journal of Radiation Research and Applied Sciences*, 6(2):63–70, 2013.
- [5] Robert Esworthy and David M Bearden. Environmental protection agency (epa): Fy2016 appropriations. Library of Congress, Congressional Research Service, 2015.
- [6] Robert K Lewis. Radon in the workplace: The occupational safety and health administration (osha) ionizing radiation standard. *Health Physics*, 111(4):374–380, 2016.
- [7] Supplemental Proposed Rule. Nuclear regulatory commission 10 cfr parts 2, 50, 51 and 52.
- [8] Terry T Yoshizumi, Sudhir K Suneja, and James S Teal. An overview of the changing us nrc regulations—10 cfr part 20. *Journal of Nuclear Medicine Technology*, 18(2):102–106, 1990.

## 11 Economics

Assessing the relative costs of a power generating plant is a very complex task that is largely dependent on location and resources. In comparison to other generation plants, LWR's are expensive to build, but are relatively cheap to operate making them competitive as a source of electricity generation.[2]. While there has been thorough economic analysis on LWR's, there are no MSR's in commercial operation currently or under construction; thus, there is little historical data about the economics or financing of MSR projects to establish a bottom-up approach. [5]. However, the MOSS reactor contains very similar design traits to the GE-Hitachi-Toshiba ABWR and there are economic cost analyses for the ISMR-600 and ORNL MSR designs to approximate the levelized cost of electricity for the MOSS reactor.

The economics of nuclear power involve numerous considerations and are typically broken down into four groups to establish the total life cycle cost: capital cost, fuel cost, operational and maintenance costs, and decommissioning cost. Each of these four groups will be evaluated in the following sections.

## 11.1 Capital Cost

Capital cost can be defined many different ways depending on how an individual wants to categorize the analysis. One popular approach is to define the overnight capital cost as “the base construction cost plus applicable owner’s cost, contingency, and first core costs” [3]. In this case, the interest during construction is not included. Contrarily, our approach defines the total capital cost (investment cost) as the sum of the total overnight capital cost and interest during construction [7]. Thus, the overnight capital cost includes only direct costs excluding owner’s cost, contingency cost, and constructive services. Using the cost estimated guidelines developed by MIT, we have approximated our direct costs in agreement to the ORNL 1000 MWe MSR design. While the MOSS reactor operates at a much lower power, equipment costs should be similar with the exception of the chemical processing plant which is not included in the MOSS design. Various categories of fixed capital costs estimated by MIT are shown below.

Direct Costs	\$/kWe
Structures and Improvements	659
Reactor Plant Equipment	870
Turbine Plant Equipment	440
Electrical Plant Equipment	266
Misc. Plant Equipment	159
Main Cond Heat Rejection System	61
Total	2455

Table 19: MIT Capital Cost Estimation [7]

The overnight capital cost as well as other characteristics can be compared to the GE-Hitachi-Tochiba ABWR as seen below in table 20. The capacity factor and thermal efficiency for the MOSS reactor was approximated to be 90% and 38%. This is a rather conservative estimate based on a 92% capacity factor and 0.4% thermal efficiency estimated in the SSR-W by MOLTEX [4]. Most importantly, there is a much larger overnight capital cost in comparison to the GE ABWR which is due to the significantly lower operating power.

Name	Operating Life (years)	Capacity Factor	Electrical Power MWe	Thermal Efficiency	Overnight Capital Cost (\$/kWe)
MOSS	50	.90	161.88	.38	2455
ABWR	40	0.87	1356	.33	1300

Table 20: Characteristics of Reactor Design [6]

After finding the overnight capital cost, the discount rate and length of construction must be considered to evaluate the total investment cost. For simplification, the MOSS reactor’s construction schedule was modeled after the GE-Hitachia-Tochiba ABWR considering the similarities of reactor size. In addition, the turbine, electrical, and reactor plant equipment are largely constant. The construction schedule can be seen below in table 21.

Type of Plant	Construction Years	Annual Capital Flow %
ABWR	4	5.4, 20.5, 59.62, 14.6

Table 21: Construction Schedule [6]

Assuming a discount rate of 8%, the investment cost can be calculating by considering the present value factor and capital recuperation factor as shown below:

$$CI = CU \frac{1}{GNA} \frac{frc(i, n)}{(i + 1)} fvp(i, W)$$

Where:

CU: Direct investment cost in dollars

GNA: Average total generation in MWh

*frc*: Capital recuperation factor

*fvp*: Present value factor

The capital recuperation factor is dependent on the discount rate ( $i$ ), and the economic life of the plant ( $n$ ) as shown below:

$$frc = \frac{i(i+1)^n}{(i+1)^n - 1}$$

The present value factor is a function of the construction schedule ( $W_k$ ), discount rate ( $i$ ), and construction period in years ( $N$ ) provided in the following equation:

$$fvp = \sum_{k=1}^N W_k (i+1)^{N-(k-1)}$$

The total investment cost is tabulated below. As you, can see the MOSS reactor is near the double the capital cost in comparison to the GE ABWR which is largely due to a lower operating power. However, 27.93 \$/MWh is significantly lower than the 60.25\$/MWh overall capital cost of the 141 MWe ISMR-300 [5] which does rise some concern with the above calculations.

Reactor Type	Investment Cost (\$/MWh)
MOSS	27.93
ABWR	17.03

Table 22: Investment Cost Comparison

## 11.2 Fuel Cost

Due to time constraints, transportation costs of LWR spent fuel and fuel fabrication were not analyzed. However, we are assuming that obtaining the legacy fuel will be free and we will be charging for the entire cost of transportation and the cost of fuel salt conversion. Thus, fuel cost will be zero.

## 11.3 Operational and Maintenance Costs

Operation and maintenance costs include all the non-fuel costs including equipment repairs, plant staffing, and purchased services during operation. Moreover, operating costs can be split into fixed costs which are not dependent on electricity production i.e. plant staffing and variable costs which vary with the electrical output i.e .non fuel consumables where the fixed cost represents a much larger portion of O&M costs[5]. Considering there are no current MSR's in operation, O&M costs can be very difficult to obtain. However, MOLTEX commissioned a cost estimation from Atkins Ltd (nuclear engineering company), which gave an estimation of 12.81\$/MWh fixed operational cost and 2.13\$/MWh variable operational cost[4]. The problem with this estimation is that it assumes the same operational cost of a UK PWR which is a large overestimate considering the intrinsic safety mechanisms of a stable salt reactor. Thus, we decided that since the MOSS reactor core is roughly the same size and is non-pressurized like the GE-ABWR, their O&M costs would be a better approximation and is tabulated below:

Plant	O&M Costs (\$/Mwh)
MOSS	8.19

Table 23: Operation and Maintenance Cost [6]

## 11.4 Decommissioning Cost

Decommissioning cost includes all the costs from planning for decommissioning until the final remediation of the site. This includes the costs to perform the decontamination, decomposing the site, and waste storage [5]. As said previously, since there are no MSR's in operation, the decommissioning cost is very difficult to approximate. However, there have been estimates provided for a 1,000 MWe MSR which is reasonable to compare to our design. The decommissioning costs including waste disposal and decomposition are provided in the table below:

Component	Decommissioning Costs (\$/Mwh)
Waste Disposal	1.0
Decomposition	0.4

Table 24: Decommissioning Cost [5]

## 11.5 Profit Analysis

Once determining the levelized cost of electricity for each component: capital, operation & maintenance, fuel, and decommissioning cost, the total LCOE was calculated for the MOSS Reactor.

Components	LCOE (\$/Mwh)
Total Capital	27.92
Fuel	0
O&M	8.19
Decommissioning	1.4
Total	37.51

Table 25: Component-Wise LCOE for MOSS Reactor

Finally, to have an understanding of profitability, our total LCOE was compared to the average electricity rate in Georgia [1]. Much to our surprise, there were huge financial returns for the MOSS reactor which definitely exceeded our expectations. While all cost components were approximated using economic estimations from similar MSR designs and an operating BWR, the results are very promising. The total profit can be seen in the table below:

Total LCOE (c/kWh)	Revenue (c/kWh)	Profit (c/kWh)
3.7514	12.66	8.9086

Table 26: Profit from MOSS Reactor

## References

- [1] Electricity Rates (Updated April 2024) &x2014; Electric Choice — electricchoice.com. <https://www.electricchoice.com/electricity-prices-by-state/>. [Accessed 20-04-2024].
- [2] Nuclear Power Economics — Nuclear Energy Costs - World Nuclear Association — world-nuclear.org. <https://world-nuclear.org/information-library/economic-aspects/economics-of-nuclear-power.aspx>. [Accessed 19-04-2024].
- [3] G. EMWG. Cost estimating guidelines for generation iv nuclear energy systems, 2007.
- [4] T. W. <https://www.techniquewebdesign.co.uk>. Costs less - Moltex Energy — moltexenergy.com. <https://www.moltexenergy.com/costs-less/>. [Accessed 20-04-2024].

- [5] B. Mignacca and G. Locatelli. Economics and finance of molten salt reactors. *Progress in Nuclear Energy*, 129:103503, 2020. ISSN 0149-1970. doi: <https://doi.org/10.1016/j.pnucene.2020.103503>. URL <https://www.sciencedirect.com/science/article/pii/S0149197020302511>.
- [6] J. C. Palacios, G. Alonso, R. Ramirez, A. Gomez, J. Ortiz, and L. C. Longoria. Levelized costs for nuclear, gas and coal for electricity, under the mexican scenario. Technical report, Instituto Nacional de Investigaciones Nucleares (MX), 2004.
- [7] D. Petti, P. J. Buongiorno, M. Corradini, and J. Parsons. The future of nuclear energy in a carbon-constrained world. *Massachusetts Institute of Technology Energy Initiative (MITEI)*, 272, 2018.

## 12 Summary of Findings and Conclusions

To conclude this research, the authors thank you for reading this far. We will now review the main findings regarding the goals and feasibility of the MoSS Reactor. Firstly, it is important to comment on the impressive feat of finding a design space in which this reactor can theoretically operate. This is an extremely novel reactor concept with much of the previous research hidden behind patents, and reverse engineering a system that can handle the high temperatures while maintaining a self-sustaining nuclear reaction is a feat on its own. Moreover, the design has shown minimal reactivity loss despite relatively high specific heat, meaning that the design can reach high burnup and avoid frequent expensive refueling outages. The design space has been shown to exist, and whether or not this design is the most optimal, the achievement now rests on future engineers and scientists to perfect the system.

One of the major goals of the reactor was to utilize spent legacy nuclear fuel in an ingenious and positive way. The radiotoxicity of one gram of transuranics entered into the core is reduced by 82% after a six-year burn and by 89% after 300 years post irradiation. This means that the waste is less harmful to humans and other life after being utilized for further power generation. What happens to nuclear waste is a critical question that governments and companies have long debated. So, it is a massive boon to give industry the option to reduce this major criticism of nuclear power. Further analysis could even be considered into reusing the discharged molten salt fuel by reinvesting more fissile plutonium into it and extracting the fission products. This possibility could even further reduce the future radiotoxicity of the remaining actinides.

## 13 Compilation of all References

### References

- [1] Properties: Stainless Steel - Grade 316 (UNS S31600) — azom.com. <https://www.azom.com/properties.aspx?ArticleID=863>. [Accessed 28-02-2024].
- [2] Federal Register :: Request Access — ecfr.gov. <https://www.ecfr.gov/current/title-40/chapter-I/subchapter-F/part-190>. [Accessed 20-04-2024].
- [3] Electricity Rates (Updated April 2024) &x2014; Electric Choice — electricchoice.com. <https://www.electricchoice.com/electricity-prices-by-state/>. [Accessed 20-04-2024].
- [4] URL <https://www.terrapower.com/benefits-molten-chloride-fast-reactor-technology/>.
- [5] nrc.gov. <https://www.nrc.gov/docs/ML0814/ML081400680.pdf>. [Accessed 17-04-2024].
- [6] Description &xAB; MSTDB — mstdb.ornl.gov. <https://mstdb.ornl.gov/description-tc/>. [Accessed 19-04-2024].
- [7] The Andasol Solar Power Station Project — power-technology.com. <https://www.power-technology.com/projects/andasolsolarpower/?cf-view>. [Accessed 19-04-2024].

- [8] Home - SAMOFAR — samofar.eu. <http://samofar.eu/>. [Accessed 19-04-2024].
- [9] Nuclear Power Economics — Nuclear Energy Costs - World Nuclear Association — world-nuclear.org. <https://world-nuclear.org/information-library/economic-aspects/economics-of-nuclear-power.aspx>. [Accessed 19-04-2024].
- [10] C. Agca and J. W. McMurray. Empirical estimation of densities in nacl-kcl-ucl3 and nacl-kcl-ycl3 molten salts using redlich-kister expansion. *Chemical Engineering Science*, 247:117086, 2022. ISSN 0009-2509. doi: <https://doi.org/10.1016/j.ces.2021.117086>. URL <https://www.sciencedirect.com/science/article/pii/S0009250921006515>.
- [11] C. Agca and J. W. McMurray. Empirical estimation of densities in nacl-kcl-ucl3 and nacl-kcl-ycl3 molten salts using redlich-kister expansion. *Chemical Engineering Science*, 247:117086, 2022.
- [12] I. Q. Al Saffar and A. W. Ezzat. Probabilistic risk assessment of typical process plant using event tree and fault tree analysis. *J Mech Eng Res Develop*, 43:465–477, 2020.
- [13] F. Ameyaw, R. Abrefah, S. Yamoah, and S. Birikorang. Analysis and estimation of core damage frequency of flow blockage and loss of coolant accident: A case study of a 10 mw water-water research reactor-psa level 1. *Science and Technology of Nuclear Installations*, 2021:1–17, 06 2021. doi: 10.1155/2021/9423176.
- [14] S. Arrhenius. Über die innere reibung verdünnter wässriger lösungen. *Zeitschrift für Physikalische Chemie*, 1 (1):285–298, 1887.
- [15] C. W. Bale, P. Chartrand, S. Degterov, G. Eriksson, K. Hack, R. B. Mahfoud, J. Melançon, A. Pelton, and S. Petersen. Factsage thermochemical software and databases. *Calphad*, 26(2):189–228, 2002.
- [16] M. Basol, J. F. Kielb, J. F. MuHooly, and K. Smit. Updating of asme nuclear code case n-201 to accommodate the needs of metallic core support structures for high temperature gas cooled reactors currently in development. Technical report, ASME Standards Technology, LLC, 2007.
- [17] A. D. Becke. Density-functional thermochemistry. i. the effect of the exchange-only gradient correction. *The Journal of chemical physics*, 96(3):2155–2160, 1992.
- [18] M. Beilmann, O. Benes, E. Capelli, V. Reuscher, R. Konings, and T. Fanganel. Excess heat capacity in liquid binary alkali-fluoride mixtures. *Inorganic Chemistry*, 52(5):2404–2411, 2013.
- [19] T. L. Bergman. *Fundamentals of heat and mass transfer*. John Wiley & Sons, 2011.
- [20] T. M. Besmann and J. Schorne-Pinto. Developing practical models of complex salts for molten salt reactors. *Thermo*, 1(2):168–178, 2021.
- [21] T. M. Besmann and J. Schorne-Pinto. Developing practical models of complex salts for molten salt reactors. *Thermo*, 1(2):168–178, 2021. ISSN 2673-7264. doi: 10.3390/thermo1020012. URL <https://www.mdpi.com/2673-7264/1/2/12>.
- [22] T. M. Besmann, J. Schorne-Pinto, M. Aziziha, A. M. Mofrad, R. E. Booth, J. A. Yingling, J. Paz Soldan Palma, C. M. Dixon, J. A. Wilson, and D. Hartanto. Applications of thermochemical modeling in molten salt reactors. *Materials*, 17(2), 2024. ISSN 1996-1944. doi: 10.3390/ma17020495. URL <https://www.mdpi.com/1996-1944/17/2/495>.
- [23] K. Bhandari, V. Grover, A. Roy, M. Sahu, R. Shukla, and J. Banerjee. Nd<sub>3+</sub>-yAl<sub>5</sub>O<sub>12</sub> system: Iso-valent substitution driven structural phase evolution and thermo-physical behavior. *Journal of Molecular Structure*, 1264:133206, 2022. ISSN 0022-2860. doi: <https://doi.org/10.1016/j.molstruc.2022.133206>. URL <https://www.sciencedirect.com/science/article/pii/S0022286022008638>.
- [24] C. V. Bhave, G. Zheng, K. Sridharan, D. Schwen, and M. R. Tonks. An electrochemical mesoscale tool for modeling the corrosion of structural alloys by molten salt. *Journal of Nuclear Materials*, 574:154147, 2023.

- [25] A. Birri, R. Gallagher, C. Agca, J. McMurray, and N. Dianne Bull Ezell. Application of the redlich-kister expansion for estimating the density of molten fluoride psuedo-ternary salt systems of nuclear industry interest. *Chemical Engineering Science*, 260:117954, 2022. ISSN 0009-2509. doi: <https://doi.org/10.1016/j.ces.2022.117954>. URL <https://www.sciencedirect.com/science/article/pii/S0009250922005383>.
- [26] A. Birri, R. Gallagher, C. Agca, J. McMurray, and N. D. B. Ezell. Application of the redlich-kister expansion for estimating the density of molten fluoride psuedo-ternary salt systems of nuclear industry interest. *Chemical Engineering Science*, 260:117954, 2022.
- [27] M. Bushnaga, T. Oha, and Y. Kima. A neutronic study on safety characteristics of fast spectrum stable salt reactor (ssr). 2021.
- [28] W.-J. Cheng, R. S. Sellers, M. H. Anderson, K. Sridharan, C.-J. Wang, and T. R. Allen. Zirconium effect on the corrosion behavior of 316l stainless steel alloy and hastelloy-n superalloy in molten fluoride salt. *Nuclear technology*, 183(2):248–259, 2013.
- [29] U. N. R. Commission et al. Subpart d—radiation dose limits for individual members of the public. *nrc.gov*, 1991.
- [30] N. R. Council et al. Environmental protection agency guidances and regulations for naturally occurring radionuclides. *Evaluation of Guidelines for Exposures to Technologically Enhanced Naturally Occurring Radioactive Materials*, 1999.
- [31] T. J. Dolan. *Molten salt reactors and thorium energy*. Woodhead Publishing, 2017.
- [32] J. Duderstadt and L. Hamilton. *Nuclear Reactor Analysis*. Wiley, 1976. ISBN 9788126541218. URL <https://books.google.com/books?id=xWvsswEACAAJ>.
- [33] G. Dul'Nev and Y. P. Zarichnyak. Thermal conductivity of liquid mixtures. *Journal of engineering physics*, 11(6):400–402, 1966.
- [34] M. D'Onorio, T. Glingler, F. Giannetti, and G. Caruso. Dynamic event tree analysis as a tool for risk assessment in nuclear fusion plants using raven and melcor. *IEEE Transactions on Plasma Science*, 50(11):4514–4520, 2022. doi: 10.1109/TPS.2022.3165170.
- [35] B. M. Elsheikh. Safety assessment of molten salt reactors in comparison with light water reactors. *Journal of Radiation Research and Applied Sciences*, 6(2):63–70, 2013. ISSN 1687-8507. doi: <https://doi.org/10.1016/j.jrras.2013.10.008>. URL <https://www.sciencedirect.com/science/article/pii/S1687850713000101>.
- [36] G. EMWG. Cost estimating guidelines for generation iv nuclear energy systems, 2007.
- [37] R. Esworthy and D. M. Bearden. Environmental protection agency (epa): Fy2016 appropriations. Library of Congress, Congressional Research Service, 2015.
- [38] B. Faure and T. Kooyman. A comparison of actinide halides for use in molten salt reactor fuels. *Progress in Nuclear Energy*, 144:104082, 2022.
- [39] C. W. Forsberg. Reactors with molten salts: options and missions. *Frederick Joliot & Otto Hahn Summer School on Nuclear Reactors, Physics and Fuels Systems, Cadarache, France*, 2004.
- [40] I. C. Gauld, G. Radulescu, G. Ilas, B. D. Murphy, M. L. Williams, and D. Wiarda. Isotopic depletion and decay methods and analysis capabilities in scale. *Nuclear Technology*, 174(2):169–195, 2011. doi: 10.13182/NT11-3. URL <https://doi.org/10.13182/NT11-3>.
- [41] A. E. Gheribi, J. A. Torres, and P. Chartrand. Recommended values for the thermal conductivity of molten salts between the melting and boiling points. *Solar energy materials and solar cells*, 126:11–25, 2014.
- [42] A. M. Graham, Z. Taylor, B. S. Collins, R. K. Salko, and M. Poschmann. Multiphysics coupling methods for molten salt reactor modeling and simulation in vera. *Nuclear Science and Engineering*, 195(10):1065–1086, 2021.

- [43] W. Grimes. Molten-salt reactor chemistry. *Nuclear Applications and Technology*, 8(2):137–155, 1970.
- [44] S. Guo, J. Zhang, W. Wu, and W. Zhou. Corrosion in the molten fluoride and chloride salts and materials development for nuclear applications. *Progress in Materials Science*, 97:448–487, 2018.
- [45] K. Hanson, K. M. Sankar, P. F. Weck, J. K. Startt, R. Dingreville, C. S. Deo, J. D. Sugar, and P. M. Singh. Effect of excess mg to control corrosion in molten mgcl<sub>2</sub> and kcl eutectic salt mixture. *Corrosion Science*, 194: 109914, 2022.
- [46] P. N. Haubenreich and J. Engel. Experience with the molten-salt reactor experiment. *Nuclear Applications and technology*, 8(2):118–136, 1970.
- [47] S. Henderson, C. Agca, J. W. McMurray, and R. A. Lefebvre. Saline: An api for thermophysical properties. Technical report, Oak Ridge National Lab.(ORNL), Oak Ridge, TN (United States), 2021.
- [48] B. A. Hombourger. Conceptual design of a sustainable waste burning molten salt reactor. Technical report, EPFL, 2018.
- [49] T. W. <https://www.techniquewebdesign.co.uk>. Costs less - Moltex Energy — moltexenergy.com. <https://www.moltexenergy.com/costs-less/>. [Accessed 20-04-2024].
- [50] D. T. Ingersoll and M. D. Carelli. *Handbook of small modular nuclear reactors*. Woodhead Publishing, 2020.
- [51] W. Jahnens-Decent and M. Ketteler. Magnesium basics. *Clinical kidney journal*, 5(Suppl\_1):i3–i14, 2012.
- [52] I. A. Kartsonakis, S. G. Stanciu, A. A. Matei, R. Hristu, A. Karantonis, and C. A. Charitidis. A comparative study of corrosion inhibitors on hot-dip galvanized steel. *Corrosion Science*, 112:289–307, 2016.
- [53] Y. Katoh and L. L. Snead. Silicon carbide and its composites for nuclear applications—historical overview. *Journal of Nuclear Materials*, 526:151849, 2019.
- [54] J. F. Kincaid and H. Eyring. Free volumes and free angle ratios of molecules in liquids. *The Journal of Chemical Physics*, 6(10):620–629, 1938.
- [55] K. Kinoshita, T. Inoue, S. P. Fusselman, D. L. Grimmett, J. J. Roy, R. L. Gay, C. L. Krueger, C. R. Nabelek, and T. S. Storwick. Separation of uranium and transuranic elements from rare earth elements by means of multistage extraction in licl-kcl/bi system. *Journal of Nuclear Science and Technology*, 36(2):189–197, 1999. doi: 10.1080/18811248.1999.9726197. URL <https://doi.org/10.1080/18811248.1999.9726197>.
- [56] J. Koger. Evaluation of hastelloy n alloys after nine years exposure to both a molten fluoride salt and air at temperatures from 700 to 560 0 c. Technical report, Oak Ridge National Lab., 1972.
- [57] R. Konings and R. E. Stoller. *Comprehensive nuclear materials*. Elsevier, 2020.
- [58] A. Krätschmer, I. O. Wallinder, and C. Leygraf. The evolution of outdoor copper patina. *Corrosion Science*, 44(3):425–450, 2002.
- [59] O. R. N. Laboratory. *The Radioactivity Concentration Guidelines*. Environmental Protection Agency, 1984. URL [https://www.epa.gov/sites/default/files/2015-06/documents/fgr\\_10.pdf](https://www.epa.gov/sites/default/files/2015-06/documents/fgr_10.pdf).
- [60] F. Lantelme and H. Groult. *Molten salts chemistry: from lab to applications*. Newnes, 2013.
- [61] N. Larrosa, R. Akid, and R. Ainsworth. Corrosion-fatigue: a review of damage tolerance models. *International Materials Reviews*, 63(5):283–308, 2018.
- [62] E. Lee, T. Oh, and Y. Kim. Burnable absorber design study for fast-spectrum molten salt reactors. 2022. URL [https://www.kns.org/files/pre\\_paper/48/22A-209-%EC%9D%B4%EC%9D%80%ED%98%81.pdf](https://www.kns.org/files/pre_paper/48/22A-209-%EC%9D%B4%EC%9D%80%ED%98%81.pdf).
- [63] R. K. Lewis. Radon in the workplace: The occupational safety and health administration (osha) ionizing radiation standard. *Health Physics*, 111(4):374–380, 2016.

- [64] S. Li, T. Ma, H. Shen, M. Yu, and Z. Lei. Analysis and optimization of the opening dynamic characteristics of molten salt check valves for concentrating solar power. *Applied Sciences*, 13(5), 2023. ISSN 2076-3417. doi: 10.3390/app13053146. URL <https://www.mdpi.com/2076-3417/13/5/3146>.
- [65] C. Linder. Investigation of new materials and methods to reduce corrosion of stainless steel in contact with molten chloride salts., 2017.
- [66] K. Lovegrove and W. Stein. Concentrating solar power technology: principles, developments and applications. 2012.
- [67] B. Mazen. (a) neutronic study on safety characteristics of fast spectrum stable salt reactor. 2021.
- [68] P. J. Maziasz and J. T. Busby. Properties of austenitic steels for nuclear reactor applications. 2020.
- [69] F. Michel-Sendis, I. Gauld, J. Martinez, C. Alejano, M. Bossant, D. Boulanger, O. Cabellos, V. Chrapciak, J. Conde, I. Fast, M. Gren, K. Govers, M. Gysemans, V. Hannstein, F. Havluj, M. Hennebach, G. Hordosy, G. Ilas, R. Kilger, R. Mills, D. Mountford, P. Ortego, G. Radulescu, M. Rahimi, A. Ranta-Aho, K. Rantamäki, B. Ruprecht, N. Soppera, M. Stuke, K. Suyama, S. Tittelbach, C. Tore, S. V. Winckel, A. Vasiliev, T. Watanabe, T. Yamamoto, and T. Yamamoto. Sfcompo-2.0: An oecd nea database of spent nuclear fuel isotopic assays, reactor design specifications, and operating data. *Annals of Nuclear Energy*, 110:779–788, 2017. ISSN 0306-4549. doi: <https://doi.org/10.1016/j.anucene.2017.07.022>. URL <https://www.sciencedirect.com/science/article/pii/S0306454917302104>.
- [70] B. Mignacca and G. Locatelli. Economics and finance of molten salt reactors. *Progress in Nuclear Energy*, 129:103503, 2020. ISSN 0149-1970. doi: <https://doi.org/10.1016/j.pnucene.2020.103503>. URL <https://www.sciencedirect.com/science/article/pii/S0149197020302511>.
- [71] M. Mikami, O. Odawara, and K. Kawamura. Sound velocity in heat transfer salt (mixture of molten sodium nitrate-potassium nitrate-sodium nitrite, 7/44/49 mol%) studied by an ultrasonic pulse-echo method. *Journal of Chemical and Engineering Data*, 26(4):411–413, 1981.
- [72] T. Oh, E. Lee, Y. Son, and Y. Kim. Preliminary analysis of burnable absorber concepts for seaborg compact molten salt reactor. 2022. URL [https://www.kns.org/files/pre\\_paper/48/22A-410-%EC%98%A4%ED%83%9C%EC%84%9D.pdf](https://www.kns.org/files/pre_paper/48/22A-410-%EC%98%A4%ED%83%9C%EC%84%9D.pdf).
- [73] R. Otis and Z.-K. Liu. pycalphad: Calphad-based computational thermodynamics in python. *Journal of Open Research Software*, 5(1), 2017.
- [74] J. C. Palacios, G. Alonso, R. Ramirez, A. Gomez, J. Ortiz, and L. C. Longoria. Levelized costs for nuclear, gas and coal for electricity, under the mexican scenario. Technical report, Instituto Nacional de Investigaciones Nucleares (MX), 2004.
- [75] B. Parikshit, M. Poschmann, M. Piro, C. Bhave, M. Tonks, and D. Schwen. Yellowjacket gibbs energy minimiser: computing thermochemical equilibrium for multiphysics simulations of molten salt reactors.
- [76] D. Petti, P. J. Buongiorno, M. Corradini, and J. Parsons. The future of nuclear energy in a carbon-constrained world. *Massachusetts Institute of Technology Energy Initiative (MITEI)*, 272, 2018.
- [77] M. Piro, S. Simunovic, and T. M. Besmann. Thermochemica user manual v1. 0. *Oak Ridge National Laboratory, Oak Ridge*2012, 2012.
- [78] M. Piro, S. Simunovic, T. M. Besmann, B. Lewis, and W. Thompson. The thermochemistry library thermochemica. *Computational Materials Science*, 67:266–272, 2013.
- [79] M. H. Piro. Computational thermochemistry of nuclear fuel. In *Advances in Nuclear Fuel Chemistry*, pages 159–182. Elsevier, 2020.
- [80] R. Powell, W. Roseveare, and H. Eyring. Diffusion, thermal conductivity, and viscous flow of liquids. *Industrial & Engineering Chemistry*, 33(4):430–435, 1941.

- [81] M. Rosenthal, P. Kasten, and R. Briggs. Molten-salt reactors—history, status, and potential. *Nuclear Applications and Technology*, 8(2):107–117, 1970.
- [82] P. R. Rubiolo, M. T. Retamales, V. Ghetta, and J. Giraud. High temperature thermal hydraulics modeling of a molten salt: application to a molten salt fast reactor (msfr). *ESAIM: Proceedings and Surveys*, 58:98–117, 2017.
- [83] S. P. Rule. Nuclear regulatory commission 10 cfr parts 2, 50, 51 and 52.
- [84] M. H. S. S. Banoori and F. Reitsma. Advances in small modular reactor technology developments, 2016.
- [85] B. Sundman, B. Jansson, and J.-O. Andersson. The thermo-calc databank system. *Calphad*, 9(2):153–190, 1985.
- [86] N. Termini, A. Birri, S. Henderson, and N. D. B. Ezell. An overview of the molten salt thermal properties database—thermophysical, version 2.1.1 (mstdb-tp v.2.1.1). 7 2023. doi: 10.2172/1988348. URL <https://www.osti.gov/biblio/1988348>.
- [87] O. Y. Tkacheva, A. V. Rudenko, and A. A. Kataev. Viscosity of fluoride melts promising for molten salt nuclear reactors. *Electrochemical Materials and Technologies*. 2023. Vol. 2. № 4, 2(4), 2023.
- [88] C. Wang, P. Zhang, Q. Meng, Z. Xue, X. Zhou, H. Ju, L. Mao, F. Shao, Y. Jing, Y. Jia, and J. Sun. Electromigration separation of lithium isotopes: The effect of electrolytes. *Journal of Environmental Chemical Engineering*, 11(3):109933, 2023. ISSN 2213-3437. doi: <https://doi.org/10.1016/j.jece.2023.109933>. URL <https://www.sciencedirect.com/science/article/pii/S2213343723006723>.
- [89] Wikipedia contributors. Enthalpy of mixing — Wikipedia, the free encyclopedia, 2023. URL [https://en.wikipedia.org/w/index.php?title=Enthalpy\\_of\\_mixing&oldid=1160533318](https://en.wikipedia.org/w/index.php?title=Enthalpy_of_mixing&oldid=1160533318). [Online; accessed 7-February-2024].
- [90] Wikipedia contributors. Ideal solution — Wikipedia, the free encyclopedia, 2024. URL [https://en.wikipedia.org/w/index.php?title=Ideal\\_solution&oldid=1197329062](https://en.wikipedia.org/w/index.php?title=Ideal_solution&oldid=1197329062). [Online; accessed 7-February-2024].
- [91] D. Williams, L. Toth, and L. UT-Battelle. Chemical considerations for the selection of the coolant for the advanced high-temperature reactor. *ORNL/GEN4/LTR-05-011, Oak Ridge National Laboratory, Oak Ridge, TN*, 2005.
- [92] X. Xu, X. Wang, P. Li, Y. Li, Q. Hao, B. Xiao, H. Elsentriecy, and D. Gervasio. Experimental test of properties of kcl–mgcl<sub>2</sub> eutectic molten salt for heat transfer and thermal storage fluid in concentrated solar power systems. *Journal of Solar Energy Engineering*, 140(5):051011, 2018.
- [93] R. Yoshioka and M. Kinoshita. *Liquid fuel, thermal neutron spectrum reactors*, pages 281–373. 12 2017. ISBN 9780081011263. doi: 10.1016/B978-0-08-101126-3.00011-7.
- [94] T. T. Yoshizumi, S. K. Suneja, and J. S. Teal. An overview of the changing us nrc regulations—10 cfr part 20. *Journal of Nuclear Medicine Technology*, 18(2):102–106, 1990.
- [95] J. Zhang and N. Li. Review of the studies on fundamental issues in lbe corrosion. *Journal of nuclear materials*, 373(1-3):351–377, 2008.
- [96] J. Zhou, J. Chen, J. Wu, S. Xia, and C. Zou. Influence of <sup>7</sup>Li enrichment on Th-U fuel breeding performance for molten salt reactors under different neutron spectra. *Progress in Nuclear Energy*, 120:103213, 2020. ISSN 0149-1970. doi: <https://doi.org/10.1016/j.pnucene.2019.103213>. URL <https://www.sciencedirect.com/science/article/pii/S014919701930321X>.
- [97] W. Zhou and J. Zhang. Thermodynamic evaluation of LiCl-KCl-PuCl<sub>3</sub> system. *Journal of Alloys and Compounds*, 695:2306–2313, 2017.

## A Appendix

### A.1 Figures

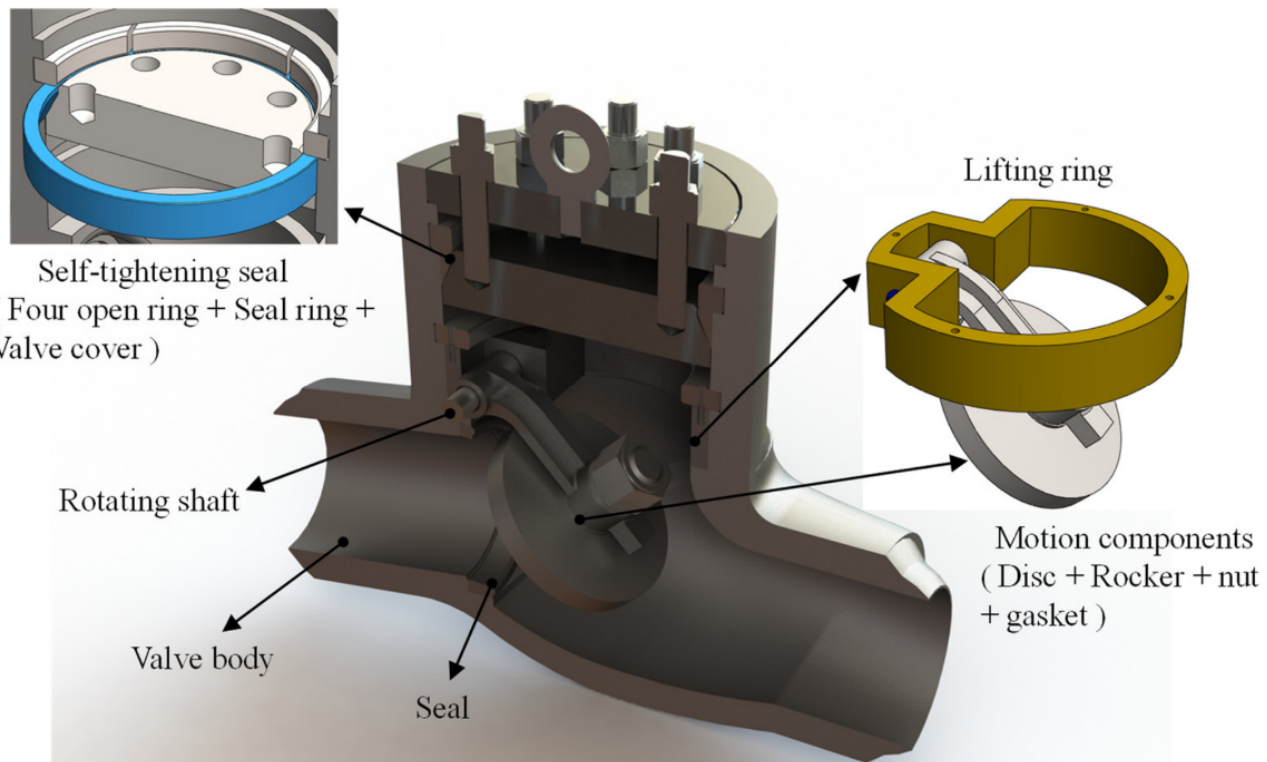


Figure 50: A reference diagram of a molten salt swing valve used in transporting molten salt in a solar plant taken from [64]

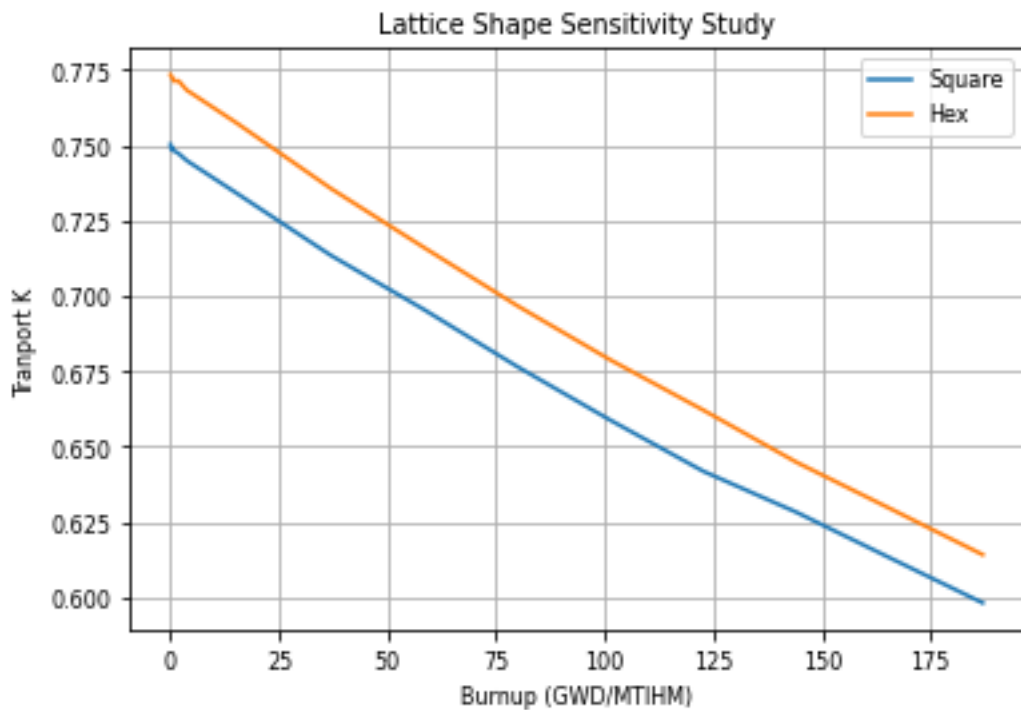


Figure 51: Lattice shape sensitivity study in pincell depletion

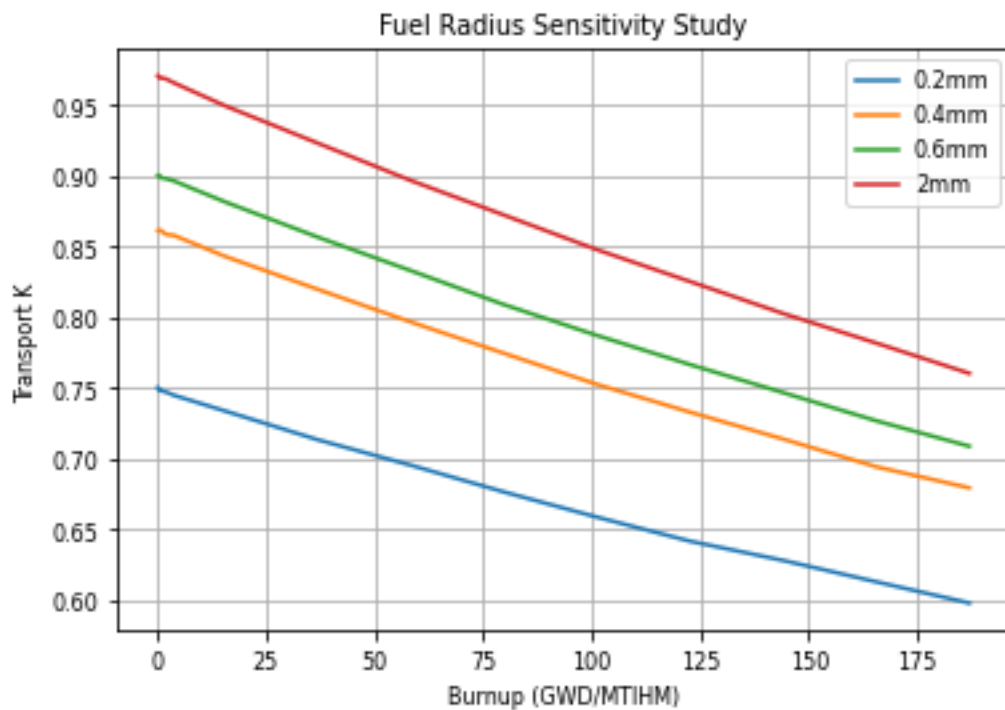


Figure 52: Fuel radius sensitivity study in pincell depletion

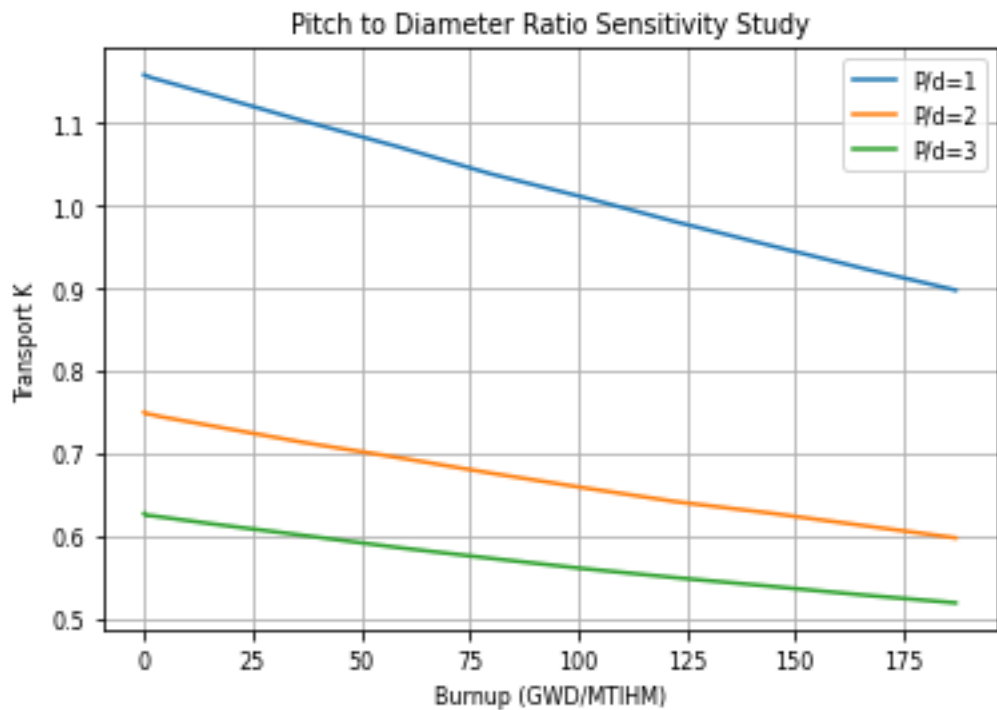


Figure 53: P/D ratio sensitivity study in pin cell depletion

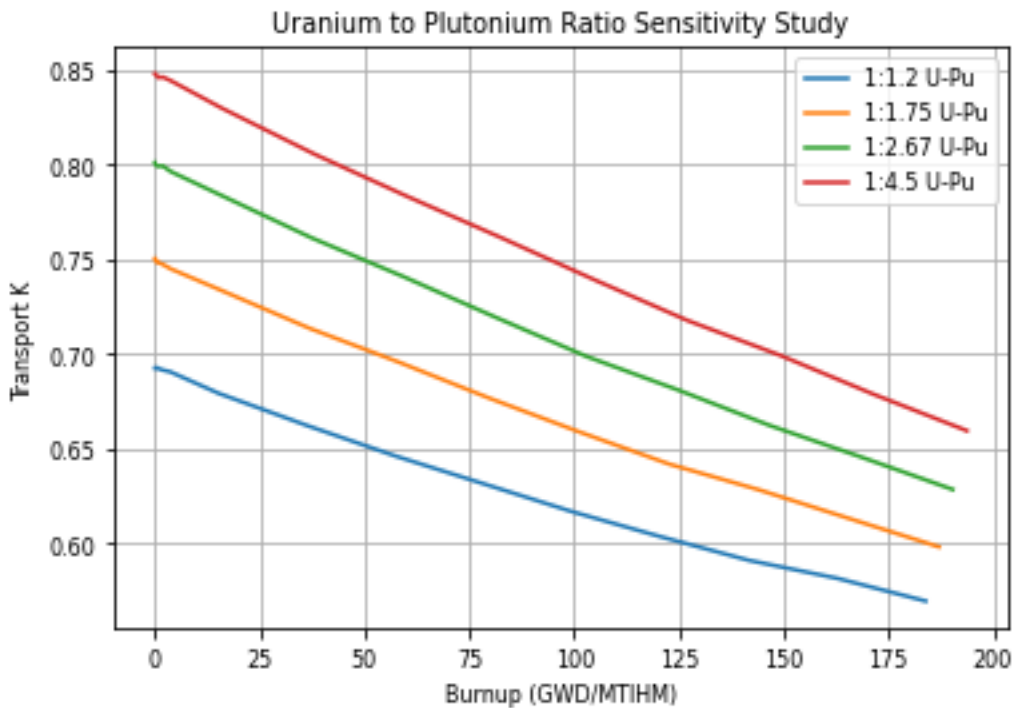


Figure 54: Uranium-Plutonium ratio sensitivity study in pin cell depletion

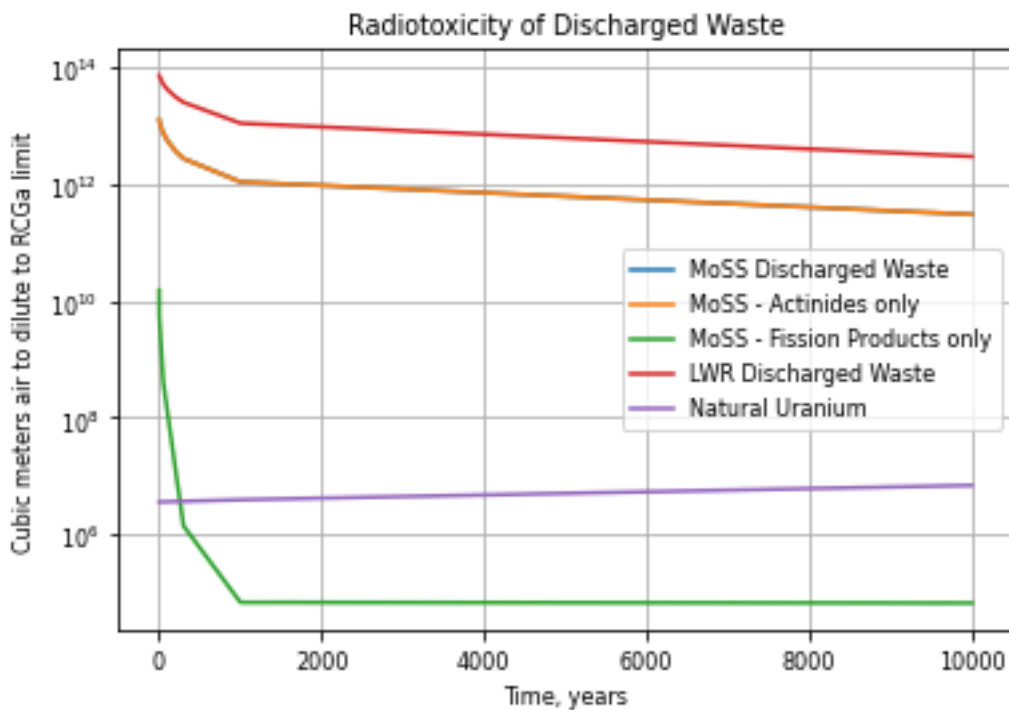


Figure 55: Radiotoxicity of 1 gram of discharged MoSS waste compared against its constituent groups, against discharged LWR waste, and against natural uranium

## A.2 Tables

Zone 1 ZAIDs	wt%	Zone 2 ZAIDs	wt%	Zone 3 ZAIDs	wt%
17035	25.2217	17035	25.4327175	17035	25.576896
17037	8.0699	17037	8.1439394	17037	8.195825
19039	7.3285	19039	7.3833333	19039	7.4204771
19040	0.5289	19040	0.535	19040	0.5394301
19041	0.00094	19041	0.0019682	19041	0.0026458
92235	0.021	92235	0.0185303	92235	0.017611
92238	10.6176	92238	10.3454545	92238	10.193837
94238	1.1701	94239	18.3484848	94239	16.6666667
94239	21.5553	94240	11.3045455	94240	11.5142478
94240	10.9032	94241	2.4151515	94241	2.1653413
94241	2.7704	94242	3.5257576	94242	3.5437376
94242	3.5091	93237	2.6984848	93237	2.4237906
93237	3.2033	95241	3.3727273	95241	3.1974818
95241	3.8013	95242	0.0798448	95242	0.0004283
95243	1.0338	96244	0.3822727	96244	0.436216
96244	0.2651	94238	1.7333333	94238	2.1653413
		95243	1.0163636	95243	1.0051359
		96242	0.1324545	54134	0.2622598
		54134	0.1684848	55135	0.2549702
		55135	0.1648485	54136	0.2463552
		54136	0.1580303	55133	0.2246521
		55137	0.1455455	55137	0.2203446
		55133	0.1463788	56138	0.2220013
		56138	0.142303	57139	0.2069251
		57139	0.1327424	58140	0.1916832
		58140	0.1227576	58142	0.1799205
		58142	0.1153333	54132	0.1794235
		54132	0.1145455	59141	0.1736249
		42100	0.1088333	44102	0.1734592
		44102	0.1093182	42100	0.1691518
		44104	0.1078485	44104	0.1671637
		59141	0.1120152	45103	0.1605699
		44101	0.0996667	60143	0.1554009
		43099	0.0985152	44101	0.1520709
		60143	0.100697	43099	0.1507621
		45103	0.1046818	96242	0.087939
		46105	0.094	46105	0.1433068
		42098	0.0924091	42098	0.1449636
		42097	0.0833636	42097	0.1286614
		54131	0.0778939	54131	0.1202783
		40096	0.0765606	40096	0.1192512
		60145	0.072197	60145	0.1108184
		40094	0.0645606	40094	0.1009609
		60146	0.0632879	60146	0.1003976
		46107	0.0615303	46107	0.0931909
		40093	0.0560606	40093	0.0870278
		58144	0.0425909	52130	0.0753645
		44106	0.0442424	44106	0.0360338
		52130	0.0483939	58144	0.0310139
				60144	0.0649437

Table 27: ZAID values and their corresponding weight percentages for each fuel region at the beginning of cycle.